

---

# Ocean Heat Fluxes Affecting Sea-Ice in the Community Climate System

## Model Version 3

---

Louis Renaud-Desjardins

Atmospheric and Ocean Sciences

McGill University, Montréal, Québec

DATE???

A thesis submitted to McGill University in partial fulfillment of the  
requirements of the degree of Doctor of Philosophy.

©Louis Renaud-Desjardins 2018

# Abstract

This thesis furthers the understanding thermal interactions between the ocean and the sea ice using the CCSM3. It focuses on the six simulations under the SRES A1B. [Holland et al. \(2006a\)](#) argued that the rapid losses of September sea ice extent recorded in each of these simulations were preceded by pulses of warm water toward the Arctic Ocean one to two years beforehand. The presented analysis includes all the physical processes affecting sea ice in connection with the years of rapid September sea ice extent loss. Every melt processes increases until the years of rapid sea ice extent loss whereas the sea ice formation processes stagnate and the sea ice transport through the gates of the Arctic Ocean decreases. Therefore, the rapid loss of September sea ice extent is caused by increased melt. The basal melt is the process which increased the most. Averaged over the six simulations, the sea ice receives  $20\text{ W/m}^2$  in 1900 up to  $120\text{ W/m}^2$  from the ocean. Significantly more than the  $2\text{ W/m}^2$  predicted by [Maykut and Untersteiner \(1971\)](#). This important increase in heat transfer is caused by an exponential increase in sea surface temperature all over the Arctic Ocean. The heat sources causing the exponential increase in sea surface temperature for the top layer of the CCSM can be uncovered through a temperature-heat ocean budget. The temperature-heat ocean budget proved impossible to close satisfactorily even if using the extended output of the fourth version of the CCSM. The error over the grid columns exceeds  $\pm 50\text{ W/m}^2$ . Nevertheless, the study of the heat transport through the gateways of the Arctic Ocean can provide insight on the warming of the Arctic Ocean and of its impact on sea ice melt. The heat transport through the gateways of the Arctic Ocean is studied for both the CCSM versions 3 and 4 by adding the results from five simulations under the RCP 6.0 scenario. Both models forecast very different Arctic conditions. The CCSM3 heat transport is dominated by the heat fluxes through the Barents Sea Opening. The total heat transfer to the Arctic Ocean is positive, warming it, from  $35\text{ W/m}^2$  in 1900 up to  $130\text{ W/m}^2$  in 2100. The CCSM4 heat transport has similar contributions from the different gateways to the Arctic Ocean. The total heat transfer simulated by the CCSM4 starts from  $19\text{ W/m}^2$  in 1900 up to  $60\text{ W/m}^2$  in 2100. The CCSM3 oceanic heat transfer is more than twice as important than the one simulated by the CCSM4.

## Résumé

Cette thèse explore les interactions thermodynamiques entre l'océan Arctique et sa glace de mer. Pour ce faire, les résultats des six simulations du CCSM3 soumises au futur scénario SRES A1B sont étudiés. [Holland et al. \(2006a\)](#) ont constaté que les pertes abruptes de superficie de glace en septembre observées ces simulations sont précédées par des maximums de transport de chaleur océanique une ou deux années au paravant. L'analyse présentée ici pousse plus loin en considérant tous les mécanismes physiques influençant la glace de mer en connexion avec les années de perte abrupte de glace. La fonte de glace s'accentue jusqu'aux pertes abruptes de glace tandis que la création de glace stagne et que l'expulsion de glace diminue. La fonte de glace est donc responsable des pertes abruptes de superficie de glace. La fonte à la base de la glace est le procédé de fonte le plus important et est celui qui augmente le plus. En moyenne, l'océan transfert à la glace  $20\text{ W/m}^2$  en 1900 et  $120\text{ W/m}^2$  en 2100. Ces flux de chaleur sont considérablement plus élevés que celui prédit par [Maykut and Untersteiner \(1971\)](#) de  $2\text{ W/m}^2$ . Cette hausse de transfert thermique est générée par la hausse exponentielle de la température de surface de l'océan Arctique. Les sources de chaleur qui influencent la température de surface de l'océan Arctique peuvent être étudiées en complétant le bilan énergétique océanique. Ce bilan ne peut pas être complété sans une erreur substantielle de  $50\text{ W/m}^2$  même en utilisant des variables manquantes grâce aux résultats du CCSM4. Néanmoins, l'étude des flux de chaleur à travers les divers accès à l'océan Arctique est possible et permet d'identifier l'impact de ces flux de chaleurs sur l'océan Arctique et sa glace de mer. Cinq simulations du CCSM4 sous le scénario RCP 6.0 sont ajoutées aux six simulations précédemment nommées. Pour le CCSM3, le flux de chaleur total à l'océan Arctique est dominé par le flux passant par l'ouverture de la mer de Barents. Le flux de chaleur total augmente la température océanique de l'Arctique à force de  $35\text{ W/m}^2$  en 1900 et  $130\text{ W/m}^2$  en 2100. Pour le CCSM4, les flux de chaleur passant par toutes les voies d'accès sont importants. Le flux de chaleur total du CCSM4 réchauffe l'océan Arctique à force de  $19\text{ W/m}^2$  en 1900 et  $60\text{ W/m}^2$  en 2100. Le CCSM3 prévoit un réchauffement océanique, causé par les flux advectifs de chaleur, deux fois plus fort que celui du CCSM4.

## **Contribution of Authors**

Data analysis and presentation of results are Louis' own work. Bruno Tremblay provided guidance throughout the process.

# Statement of Originality

The following elements of the thesis show original scholarship and represent distinct contributions to knowledge:

- [Holland et al. \(2006a\)](#) observed rapid loss of September sea ice extent in all of the CCSM3 SRES A1B simulations. They notice that the ocean heat transport to the Arctic precedes the mean Arctic sea ice thickness by two years. The work presented in chapter 3, investigates the role of all the sources of melt, growth and transport for the CCSM3 simulations under the SRES A1B. The ocean heat transport considered in [Holland et al. \(2006a\)](#) includes all heat transport at 55° North. The region north of the 55<sup>th</sup> parallel encloses more than just the Arctic. This thesis works with an original region enclosing the Arctic Ocean tightly in the hope of a better correlation between the heat transport and the sea ice. [Holland et al. \(2010\)](#) analyzed the total melt, total growth and total transport of several GCMs and reanalysis including the CCSM3. This thesis investigates further by distinguishing (1) the total melt from its locations (bottom, top and lateral), (2) the sea ice creation from its two processes (basal and frazil), (3) the sea ice transport through the gates of the Arctic Ocean (the Fram Strait, the Barents Sea Opening, the CAA and the Bering Strait). In addition, inspired by the work of [Winton \(2011\)](#) which observed linear trends between the Arctic sea ice extent and the global temperature in the GFDL simulations, a decreasing exponential relationship between the sea ice volume and the extra forcing from the SRES A1B scenario is presented.
- Chapter 4 started off as a study of vertical heat fluxes of the CCSM3 simulations. Since the vertical diffusion is not part of the standard output, Professor Bruno Tremblay hired an NCAR employee, Laura Landrum with the help of Marika Holland, to provide a code calculating vertical heat diffusion as a residual of the temperature-heat equation. The code was finished when I started my PhD. As a test of the code, I used all the heat components included in their code and tried to reconstruct the temperature-heat equation. This work proved to be incredibly more complicated than I anticipated.

Chapter 4 and the appendices of this thesis are the results of this work. While the reconstruction of the temperature/heat equation is not original in itself - it is already known that the CCSM solves it -, it is a formidable tool to possess. No indications on how it should be done are published. Many scholars I met would have greatly appreciated the presence of such a tool for their own research.

- Despite the inconclusive results of chapter 4, I pushed forward and analyzed the heat transport through the gateways of the Arctic Ocean of the CCSM versions 3 and 4. Heat transports are mainly recorded over the Fram Strait and the Bering Strait ([Beszczynska-Moller et al., 2011](#)) because their locations are well accepted. The two other gateways are the Canadian Arctic Archipelago and the Barents Sea Opening. The water flowing through the many openings of the Canadian Arctic Archipelago is arduous to document. The Barents Sea Opening is not clearly defined. It spans from the east side of Svalbard unto Europe. It can end anywhere from the northern part of Norway to the eastern part of Novaya Zemlya Island. Considerable amount of sea ice exits the Arctic through the Fram Strait ([Smedsrud et al., 2017](#)) making it an excellent location to study. The Bering Strait is shallow and narrow. [Woodgate et al. \(2010\)](#) showed that the heat transport through the Bering Strait has an important impact on the sea ice thickness and cover in the proximity of the strait. Even though the heat transports have a notable impact on the Arctic sea ice, it is not thoroughly studied utilizing GCMs results. The freshwater transports are studied more extensively ([Wijffels, 2001](#)), from observations data([Serreze et al., 2006](#)) and from GCMs results ([Lehner et al., 2012](#)), since they have a considerable effect on the global thermohaline circulation. Chapter 5 tackles the neglect of the model community toward the heat transport through the gateways of the Arctic Ocean. The results from the CCSM3 and the CCSM4 hold significant discrepancies.

# Contents

<b>Abstract</b>	i
<b>Résumé</b>	ii
<b>Contribution of Authors</b>	iii
<b>Statement of Originality</b>	iv
<b>List of Figures</b>	ix
<b>List of Tables</b>	xv
<b>1 Introduction</b>	1
<b>2 The Arctic</b>	3
2.1 Arctic Ocean . . . . .	3
2.2 Sea ice . . . . .	7
2.2.1 Sea ice extent . . . . .	9
2.2.2 Sea ice thickness . . . . .	10
2.3 Feedback . . . . .	12
2.4 Community Climate System Model . . . . .	14
2.4.1 CCSM ocean component - POP model . . . . .	15
2.4.2 CCSM sea ice component - CICE model and CSIM . . . . .	20
2.4.3 Future projections . . . . .	25
2.5 Conclusion . . . . .	25
<b>3 Physical processes affecting sea ice in the Community Climate System Model (CCSM) version 3</b>	28
3.1 Rapid declines . . . . .	29
3.2 Ocean to sea ice thermodynamic interactions . . . . .	30
3.3 Sea ice volume . . . . .	33
3.4 Dynamic vs thermodynamic processes . . . . .	39

3.5	Transport out of the Arctic Ocean . . . . .	41
3.6	Thermodynamic . . . . .	43
3.6.1	Surface melt . . . . .	44
3.6.2	Basal melt and growth . . . . .	48
3.6.3	Lateral melt . . . . .	51
3.6.4	Frazil . . . . .	52
3.7	Discussion . . . . .	53
<b>4</b>	<b>Energy budget of the ocean component of the CCSM</b>	<b>56</b>
4.1	Energy equation . . . . .	56
4.2	Energy budget for the CCSM3 . . . . .	59
4.3	CCSM4 . . . . .	65
4.4	CCSM coded temperature equation . . . . .	68
4.5	Conclusion . . . . .	70
<b>5</b>	<b>Ocean advective heat fluxes through the gateways of the Arctic Ocean simulated by the CCSM version 3 and 4</b>	<b>72</b>
5.1	Introduction . . . . .	72
5.2	Fram Strait . . . . .	75
5.3	Barents Sea Opening . . . . .	80
5.4	Canadian Arctic Archipelago . . . . .	83
5.5	Bering Strait . . . . .	86
5.6	Discussion . . . . .	88
<b>6</b>	<b>Conclusion</b>	<b>92</b>
<b>Appendix A</b>	<b>CCSM4 code verification</b>	<b>95</b>
A.1	Temperature equation . . . . .	95
A.2	Horizontal diffusion . . . . .	95
A.3	Advection . . . . .	98
A.3.1	Vertical diffusion . . . . .	101

A.4	Reset temperature . . . . .	103
A.5	KPP . . . . .	104
A.6	Absorbed short wave . . . . .	105
A.7	Conclusion . . . . .	105
	<b>Table of Abbreviations</b>	<b>106</b>
	<b>References</b>	<b>107</b>

# List of Figures

2.1	The two definitions of the Arctic domain: 1) by the polar circle in dashed blues, and 2) by the $10^{\circ}\text{C}$ July average isotherm. This map was contributed by the United States Central Intelligence Agency, published in 2002. The map can be retrieve at the Library of Congress Geography and Map Division, Washington, D.C. or at the web site <a href="https://www.loc.gov/resource/g3270.ct001717/">https://www.loc.gov/resource/g3270.ct001717/</a> . . . . .	4
2.2	International Bathymetric Chart of the Arctic Ocean annotated with the names of basins, ridges and shelves (Jakobsson et al., 2012). . . . .	5
2.3	Circulation map of the Arctic Ocean. Red arrows show warm currents and blue arrows cold currents. The green region is for the Sub-Arctic, the purple region is for the Low Arctic and the blue region is for the high arctic (AMAP, 2013). . . . .	6
2.4	Schematic representation of the temperature and salinity structure in the upper Arctic Ocean and its maintenance. Taken from Aagaard et al. (1981). . . .	7
2.5	Sea ice extent in blue and sea ice area in red. Both curves are bound by their maximum or March area and minimum or September area. The four black dots display the four sea ice extent minima, 2002, 2005, 2007 and 2012. Data provided by the NSIDC Fetterer et al. (2017). . . . .	10
2.6	Arctic death spiral showing the evolution for each monthly sea ice volume between 1979 and 2017. . . . .	12
2.7	CCSM grid with the North Pole displaced over Greenland. . . . .	18
2.8	Left) Horizontal discretization of the grid showing the locations of tracers, velocities and lengths. Center) Vertical locations of tracers and velocities. Right) Vertical discretization. Taken from Smith et al. (2010). . . . .	19
2.9	Radiative forcing evolution of the different scenarios of the IPCC-AR4 (A1B, A2, B1) and IPCC-AR5 (RCPs). . . . .	26

3.1	Arctic Ocean domain including the four main gates considered in this study: Fram Strait, Barents Sea Opening (BSO), Bering Strait and Canadian Arctic Archipelago (CAA). For simplicity, All gates are defined along lines of constant latitude or longitude index in the rotated grid. . . . .	30
3.2	Yearly maximum and minimum Arctic sea ice volume. The vertical lines represents the years of rapid September sea ice decline. . . . .	35
3.3	Left) Minimum sea ice volume as a function of A1B SRES forcing. Right) Semilog plot of sea ice volume in function of A1B SRES extra forcing. The linear trend of the right plot proves that the sea ice volume decreases exponentially in function of the A1B scenario forcing. Each colour represents a different simulation. . . . .	36
3.4	Dotted-blue) September one-metre sea ice thickness contour five years before the first rapid loss event. Solid-blue) September one-metre sea ice thickness contour five years after the last rapid loss event. Dotted-red) September sea ice extent (15% sea ice concentration contour) five years before the first rapid loss event. Solid-red) September sea ice extent (15% sea ice concentration contour) five years after the last rapid loss event. . . . .	37
3.5	March 2099 sea ice concentration. . . . .	38
3.6	Yearly-mean thermodynamic changes (red), dynamic changes (blue) and tendency (black) of SIA. Vertical black lines represent the year of rapid September sea ice decline. These quantities are obtained from averaging over the Arctic domain presented in figure 3.1. . . . .	40
3.7	Yearly-mean thermodynamic changes (red), dynamic changes (blue) and total (black) of SIV. These quantities are obtained from averaging over the Arctic domain presented in figure 3.1. Vertical black lines represent the years of rapid September sea ice decline. . . . .	41
3.8	Sea ice transport out of the Arctic Ocean (blue), changes in sea ice volume caused by dynamic processes (green) and the difference between the two (red). The data represents yearly averages. . . . .	42

3.9	Yearly-mean Fram (blue), Barents (red), CAA (yellow) and Bering (purple) ice transport out of the Arctic Ocean. . . . .	43
3.10	Yearly-mean basal (blue), lateral (green) and surface (red) melt integrated over the Arctic Ocean. Vertical black lines represent the years of rapid September sea ice extent decline. . . . .	44
3.11	Yearly-mean sea ice surface fluxes averaged over the Arctic Ocean: red) down-welling long wave, blue) emitted longwave, yellow) shortwave radiation reaching sea ice, purple) latent, green) sensible. Vertical lines depict the years of rapid September sea ice extent decline. . . . .	46
3.12	Yearly-mean frazil ice formation (blue) and basal ice growth (green) integrated over the Arctic Ocean. Vertical black lines represent the years of rapid September sea ice extent decline. . . . .	49
3.13	Yearly-mean turbulent heat flux between the sea ice and ocean averaged over the Arctic Ocean. A negative value represents a loss of heat from the ocean to the sea ice. Vertical black lines represent the years of rapid September sea ice extent decline. . . . .	51
3.14	Yearly-mean sea surface temperature averaged over the Arctic Ocean in $^{\circ}\text{C}$ . Vertical black lines represent the years of rapid September sea ice extent decline. . . . .	52
4.1	Top) Global forcings for the year 1950. Bottom) Temperature temporal derivative for the year 1950 from three schemes (solid) and their associated budget error (dashed): Euler (blue), backward Euler (green) and Leap-Frog (red). . . . .	61
4.2	Top) Arctic forcings for the year 1950. Bottom) Temperature temporal derivative for the year 1950 from three schemes and its associated budget error (dashed): Euler (blue), backward Euler (green) and Leap-Frog (red). . . . .	63
4.3	Column budget error using the leapfrog scheme for the temporal derivative for every month of year 1950. . . . .	64

4.4	Top) Yearly global internal energy budget of the CCSM4. Bottom) Yearly Arctic Ocean internal energy budget of the CCSM4. Following the legend, dT stands for the yearly internal energy variation, adv for advection, diff for diffusion, surf for surface, q for frazil ice formation and budget represented the internal energy variation minus the fluxes. . . . .	66
4.5	Error of the vertically integrated internal energy budget in $W/m^2$ for the years 1951 to 1958 and in the bottom right corner, the average error over 1950-59. . .	67
5.1	Bathymetry of the Fram Strait for the CCSM version 3 in blue and version 4 in red. The Yerkman Plateau is located on the left side (west) of the Fram Strait. Completely on the left (west) is Greenland and on the right (east) side is Svalbard. . . . .	75
5.2	Fram Strait energy transport, volume transport and temperature for the CCSM3 in blue and the CCSM4 in red. The volume transport and temperature are divided as: averaged over the full gateway (second row), averaged over the inflow (third row), averaged over the inflow (fourth row). . . . .	76
5.3	Fram Strait spatial variations in heat flux, velocity and temperature. The left column is dedicated to the CCSM3 and the right column is dedicated to the CCSM4. The variations are calculated from the difference between the 2050-2099 average and the 1900-1950 average. The depth axis is in metres and the x-axis is in kilometres. . . . .	78
5.4	Example of a two cell Arakawa B-grid bordered by land. The orientation of the grid is on the x-y plane. The ocean temperature of the second and third cells is defined while the temperature of the first and fourth cells is undefined since they are land cell. Only the second cell has a defined velocity. The first and third cell velocity ends on land and is defined as zero. The velocity of the fourth cell is undefined since there is no water bordering it. . . . .	79
5.5	Bathymetry of the Barents Sea Opening for the CCSM version 3 in blue and version 4 in red. The location of Novaya Zemlya island is showed. On the left side (west) is Svalbard. On the right side (east) is Russia. . . . .	80

5.6	Barents Sea Opening energy transport, volume transport and temperature for the CCSM3 in blue and the CCSM4 in red. The volume transport and temperature are divided as: averaged over the full gateway (second row), averaged over the inflow (third row), averaged over the inflow (fourth row). . . . .	81
5.7	Barents Sea Opening spatial variations in heat flux, velocity and temperature. The left column is dedicated to the CCSM3 and the right column is dedicated to the CCSM4. The variations are calculated from the difference between the 2050-2099 average and the 1900-1950 average. The depth axis is in metres and the x-axis is in kilometres. Note that the colour axis changed from figure 5.3 . .	82
5.8	Bathymetry of the Canadian Arctic Archipelago along the cross-section defined in figure 3.1. It is completely located inside Canadian territory. . . . .	84
5.9	Canadian Arctic Archipelago energy transport, volume transport and temperature for the CCSM3 in blue and the CCSM4 in red. The volume transport and temperature are divided as: averaged over the full gateway (second row), averaged over the inflow (third row), averaged over the inflow (fourth row). . .	85
5.10	Bathymetry of the Bering Strait for the CCSM3 in blue and CCSM4 in red. On the right side (west) of the strait is Russia. On the left side (east) of the strait is Alaska, United States of America. . . . .	87
5.11	Bering Strait energy transport, volume transport and temperature. Blue) CCSM3. Red) CCSM4. . . . .	88
5.12	Heat transport through the gateways of the Arctic Ocean. Top) CCSM3. Bottom) CCSM4. . . . .	89
5.13	Volume transport through the gateways of the Arctic Ocean. Top) CCSM3. Bottom) CCSM4. . . . .	90
A.1	Difference between HDIFT and its reconstruction from HDIFE_TEMP and HDIFN_TEMP in $W/m^2$ . . . . .	98
A.2	Difference between ADVT and its reconstruction from UET and VNT in $W/m^2$ .100	
A.3	Code definition of SHF verification with the output variables: SHF, EVAP_F, SENH_F, LWUP_F, LWDN_F, MELTH_F, SNOW_F, IOFF_F, SHF_QSW.102	

A.4 Yearly vertically integrated KPP mixing term in $W/m^2$ .	104
---	-----

## List of Tables

3.1	CCSM variable names and definitions.	39
3.2	Sea ice volume changes due to melt and formation at three different periods: 1900-1909, at the abrupt loss events and 2090-2099. All volume changes are in $1000 \text{ km}^2/\text{y}$ .	54
4.1	CCSM3 output variables required for the energy budget.	60
4.2	CCSM4 output variables required for the energy budget.	65
5.1	Heat and volume transport through the gateways of the Arctic Ocean from ob- servations, simulated by the CCSM3 SRES A1B and simulated by the CCSM4 RCP 6.0 scenario. The gateways of the Arctic Ocean are: Fram Strait, Barents Sea Opening (BSO), Canadian Arctic Archipelago (CAA) and Bering Strait. The highlighted values do not agree with the observations.	91

# 1 Introduction

The Arctic is undergoing a rapid and critical transformation. Sea ice has been decreasing both in extent and thickness since 1979, the first year we have been able to monitor it in 1979 ([Overland and Wang, 2013](#)). The Arctic has lost 50% of its sea ice extent and 75% of its sea ice volume showing no signs of slowing or stopping. All wildlife living on sea ice must adapt forcing a major mutation of the ecosystems ([Pfirman and Tremblay, 2009](#); [Laidre et al., 2008](#)). The marine ecosystems are also adjusting to the new warmer waters entering the Arctic Ocean ([Beszczynska-Moller et al., 2011](#); [Wassmann et al., 2011](#)). The Inuit infrastructure and health are vulnerable to climate changes. Harvesting is now more dangerous and access to hunting areas is increasingly difficult ([Ford et al., 2006](#); [Ford, 2009](#)). There is also the threat of permafrost melt releasing trapped green house gases enhancing global warming ([Schaefer et al., 2012](#)). The only bright side is the opening of new, quicker, marine routes ([Johannessen et al., 2000](#)). Those new routes could lead to a decrease in fuel consumption in comparison with the usual longer paths.

[Holland et al. \(2006a\)](#) presented the results of six simulations under the Special Report on Emission Scenario (SRES) A1B from the Community Climate System Model version 3 (CCSM3). The simulations are characterized by a summer ice-free Arctic Ocean as early as 2040 preceded by a rapid loss of September sea ice extent. [Holland et al. \(2006a\)](#) hypothesize that the ocean could catalyze the rapid loss of sea ice after observing pulse of warm water entering the Arctic Ocean one or two years prior the rapid losses. The ocean heat transfer to the sea ice has been theorized to be  $2 - 4 \text{ W/m}^2$  constant throughout the year ([Maykut and Untersteiner, 1971](#)). Measurements showed that the thermal interactions between the ocean and the sea ice follow a seasonal cycle and that it differs greatly spatially ([McPhee and Untersteiner, 1982](#); [McPhee et al., 2003](#); [Perovich et al., 1989](#); [Perovich and Elder, 2002](#)).

This thesis aims at describing the exchanges of heat between the sea ice and the ocean, and the sources of ocean heat. More specifically, it focuses on the six simulations of the CCSM3 under the SRES A1B presented in [Holland et al. \(2006a\)](#). Chapter 2 presents a literature review of the Arctic Ocean and its sea ice. It also presents the CCSM3 and its features such as its grids and model components. Chapter 3 investigates all the processes affecting the sea

ice with a more acute interest for the interactions between the Arctic Ocean and its sea ice. Since only the first layer of the Arctic Ocean interacts with the sea ice, chapter 4 presents all the sources of heat affecting the top ocean layer attempting its energy-temperature budget. Chapter 5 studies the ocean advective heat fluxes through the gateways of the Arctic Ocean for both the CCSM version 3 and version 4.

## 2 The Arctic

This chapter introduces the basic notions used by the scientific community to characterise the Arctic Ocean. The covered concepts include (1) a definition of the Arctic, (2) a definition of the Arctic Ocean, circulation of the Arctic Ocean, temperature and salinity profile of the Arctic Ocean and its halocline in section 2.1, (3) a definition of sea ice, sea ice concentration measured by satellites, definition of sea ice extent, sea ice thickness measurements in section 2.2, (4) Arctic sea ice feedbacks in section 2.3, (5) ocean modelling, sea ice modelling and future projection forcing in section 2.4. While the present introduction is succinct, the curious reader is invited to read the references.

The Arctic is widely understood as the northern region of planet Earth. It comes from the Greek word *arktitos* which means *near the Bear* or *northern* referring to the Ursa constellations and Polaris, the North Star. The Arctic has two scientific definitions: (1) everything north of the polar circle and (2) where the average temperature of the warmest month, July, is below  $10^{\circ}\text{C}$ <sup>1</sup>. Both Arctic definitions are shown in figure 2.1. The polar circle marks the northernmost point at which the noon sun is barely visible on the winter solstice - no daylight - and southernmost point at which the midnight sun is barely visible on a summer solstice - no night time. A winter solstice occurs the day with the least sunlight while the summer solstice occurs the day with the most sunlight. The polar circle changes due to planet Earth axial tilt oscillation between  $22.1^{\circ}$  and  $24.5^{\circ}$  over 40 000 years. Right now the polar circle is moving northward at around  $15\text{ m/y}$ . The second definition follows the tree line, the line separating where trees can still grow and where they cannot grow (Smithson et al., 2002). By that definition, the Arctic is the region where no trees can grow. It is bound to increase with global warming.

### 2.1 Arctic Ocean

The Arctic Ocean is bordered by land from the United States (Alaska), Canada (Canadian Arctic Archipelago or CAA), Finland, Denmark (Greenland), Iceland, Norway (Svalbard), Russia and Sweden, figure 2.2. It is composed of two major basins: the Eurasian basin

---

<sup>1</sup>NSIDC, <https://nsidc.org/cryosphere/arctic-meteorology/arctic.html>, last visited December 2017



Figure 2.1: The two definitions of the Arctic domain: 1) by the polar circle in dashed blues, and 2) by the  $10^{\circ}\text{C}$  July average isotherm. This map was contributed by the United States Central Intelligence Agency, published in 2002. The map can be retrieved at the Library of Congress Geography and Map Division, Washington, D.C. or at the web site <https://www.loc.gov/resource/g3270.ct001717/>.

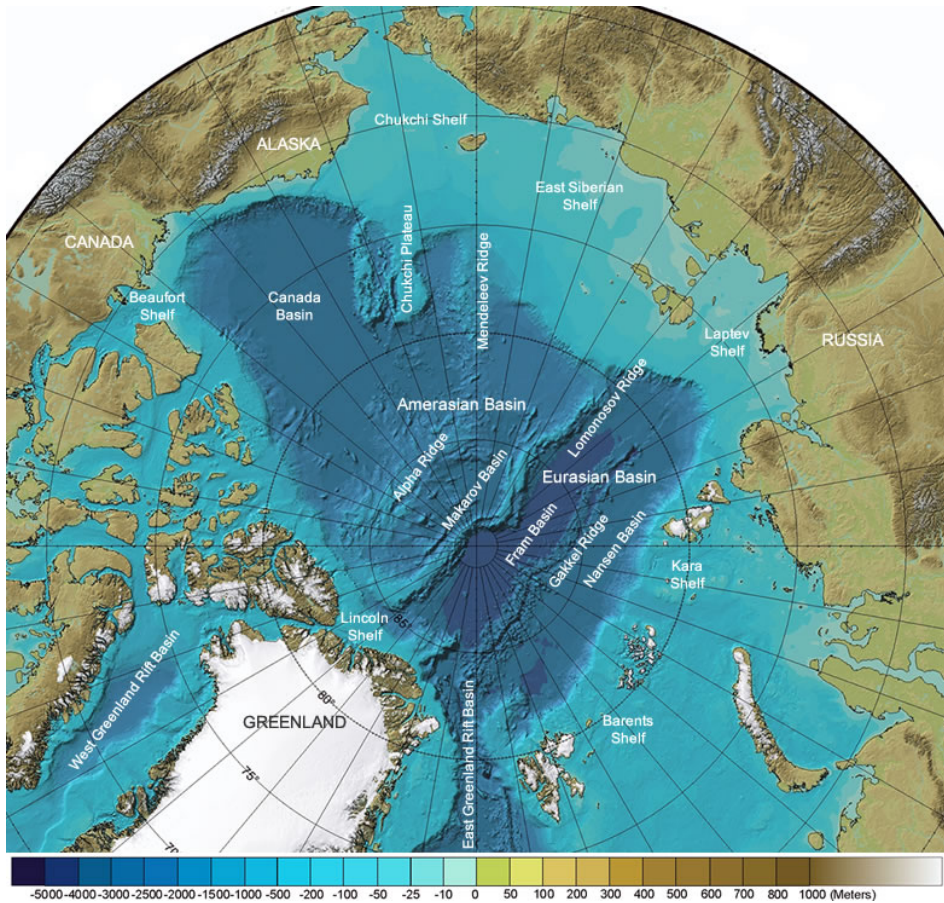


Figure 2.2: International Bathymetric Chart of the Arctic Ocean annotated with the names of basins, ridges and shelves ([Jakobsson et al., 2012](#)).

northeast of Greenland and the Amerasian basin northwest of Greenland divided by the Lomonosov Ridge. The Eurasian Basin is composed of the Amundsen or Fram Basin and the Nansen basin separated by the Gakkel ridge. The Amerasian Basin is composed of the Beauford Basin and the Makarov basin divided by the Alpha ridge. Seven seas share the Arctic Ocean: the Greenland sea that lies east of Greenland, the Beaufort Sea between Canada and Alaska and five seas that border Russia. From east to west they are the Barents Sea, Kara Sea, Laptev Sea, East Siberian Sea and the Chukchi Sea which also borders Alaska. The Arctic Ocean has the highest ratio by far of continental shelf area over ocean area with a ratio of one third, making it unique. The mean depth of the Arctic Ocean is about one kilometre with a maximum depth of 5.5 km.

The Arctic Ocean circulation is depicted in figure 2.3. Warm Atlantic waters enter the Arctic Ocean by the West Spitzbergen current west of Svalbard and by the North Cape current in the Barents Sea. The Atlantic waters are heavier than the Arctic Ocean surface

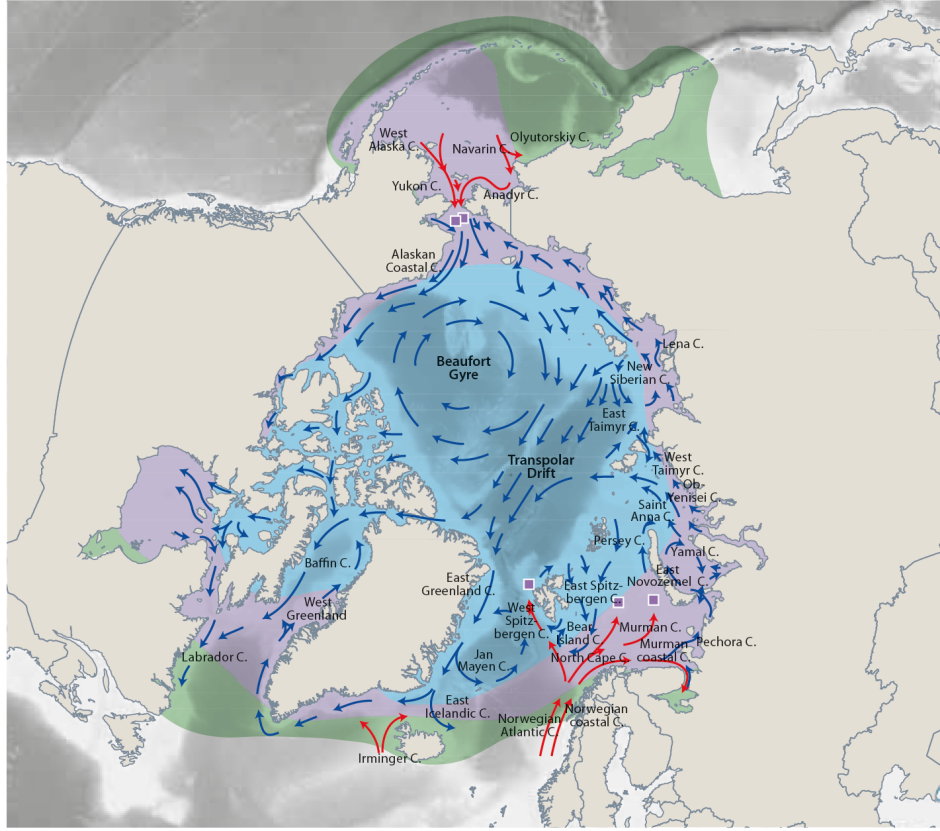


Figure 2.3: Circulation map of the Arctic Ocean. Red arrows show warm currents and blue arrows cold currents. The green region is for the Sub-Arctic, the purple region is for the Low Arctic and the blue region is for the high arctic (AMAP, 2013).

waters being saltier though warmer. They sink and turn counterclockwise at the edge of the Arctic Ocean. The Pacific waters enter the Chukchi Sea and follow the Alaskan and Canadian coast into the Canadian Arctic Archipelago. The interior of the Amerasian Basin is dominated by the Beaufort Gyre turning clockwise. The transpolar drift takes waters through the Arctic Ocean following the Lomonosov Ridge through the Fram Basin exiting the Arctic Ocean as the East Greenland current.

The vertical temperature-salinity structure of the Arctic Ocean exhibits the presence of a cold halocline layer, figure 2.4. The observed temperature-salinity profile is constant at  $-1.8^{\circ}\text{C}$  and 33.5 PSU over the first 50 meters. This continuity arises from mechanical surface forcings such as wind or ice motion causing turmoil and mixing over the first 50 meters. It is called the surface mixed layer. Between 50 and 200 metres, the ocean temperature stays at freezing point but the salinity increases. This layer is the halocline. The increased salinity makes the water denser, stabilizing the water column which diminishes the vertical mixing

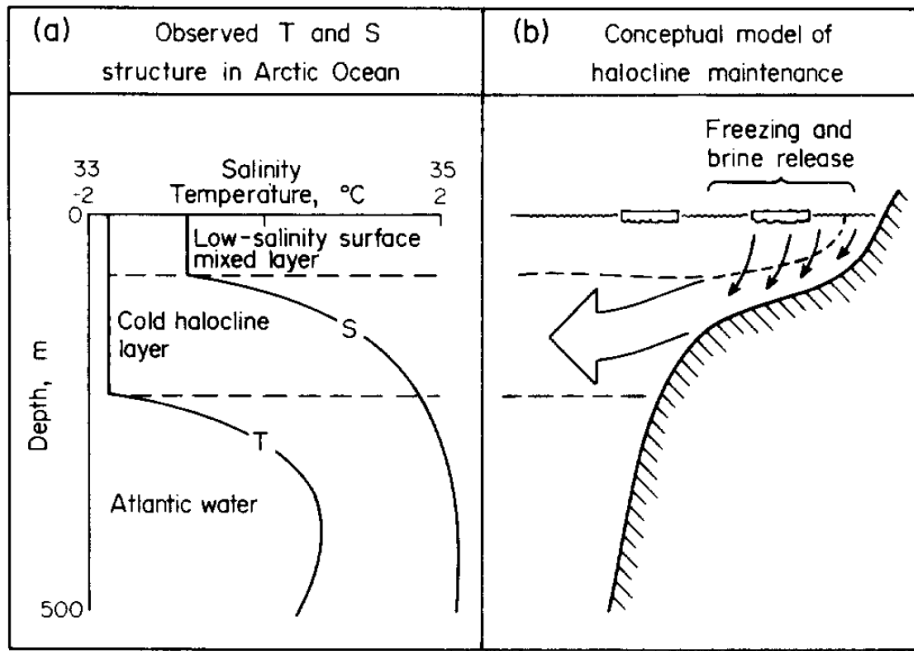


Figure 2.4: Schematic representation of the temperature and salinity structure in the upper Arctic Ocean and its maintenance. Taken from [Aagaard et al. \(1981\)](#).

insulating the sea ice from the warm Atlantic waters between 200 and 500 metres at  $1^{\circ}\text{C}$  and  $35 \text{ PSU}$  ([Steele and Boyd, 1998](#)). [Aagaard et al. \(1981\)](#) showed that the halocline is created by the salt rejection during ice formation. This salt rejection increases the salinity of cold already saline surface waters causing its density to increase and sink between 50 and 200 metres.

## 2.2 Sea ice

Ice formed from sea water contains salt therefore sea ice is a complex material. In this section, a brief introduction of sea ice as a material is presented. Section 2.2.1 defines sea ice extent and presents measurements of it. Section 2.2.2 presents sea ice thickness measurements.

Sea ice is a mixture of freshwater solid ice crystals and interstitial liquid salty brine ([Petrich and Eicken, 2010](#)). Brine trapped in sea ice can escape and reach the ocean by five processes: initial salt rejection, salt diffusion, brine expulsion, gravity drainage and flushing. [Notz and Worster \(2009\)](#) explored all five options using analytical solutions from a mushy layer ([Feltham et al., 2006](#)), numerical solutions from a one-dimensional enthalpy model ([Notz and Grae Worster, 2006](#)) and observations ([Shirtcliffe et al., 1991; Notz, 2005](#)). They

found that only gravity drainage during winter and flushing during summer contributed to salt rejection. During winter, as the surface sea ice temperature decreases, the interstitial liquid brine becomes denser creating a brine-density unstable profile. This heavier brine will push down resulting in convection replacing salty sea ice brine by ocean water. The flushing happens in summer when the ice becomes permeable. [Golden et al. \(1998\)](#) found that the ice becomes permeable at a brine volume fraction of 5%, temperature of  $-5^{\circ}\text{C}$  and salinity of 5 parts per thousand. This is known as the law of fives. When the sea ice becomes permeable, all water inside and over the ice is flushed down into the ocean leaving the ice brine free.

The Arctic Ocean is covered by sea ice. Sea ice concentration (SIC) is measured by satellite equipped with a microwave radiometer ([Markus et al., 2012](#)). The radiometer records the intensity (or brightness temperature  $T_B$ ) of electromagnetic radiation for a specified frequency  $\nu$ ,

$$T_B = \epsilon T_S e^{-\tau} + \int_0^\tau T(z) \zeta(z) e^{-\tau+\tau'(z)} d\tau' + (1 - \epsilon) \kappa e^{-\tau} \int_0^\tau T(z) \zeta(z) e^{-\tau'(z)} d\tau'(z), \quad (2.1)$$

$\epsilon$  is the emissivity of the surface,  $T_S$  is the surface temperature,  $\tau$  is the atmospheric opacity from the surface to the satellite,  $T(z)$  is the temperature at height  $z$ ,  $\zeta(z)$  is the emittance at height  $z$ ,  $\tau'(z)$  is the atmospheric opacity from the surface to height  $z$ ,  $\kappa$  is an estimate of the diffusiveness of the surface reflection. The first term of the right-hand side of the equation is the surface emission for frequency  $\nu$  reaching the satellite which is often the dominant source. The second term is the emission from the atmospheric column reaching the satellite. The third term represents the downwelling atmospheric column radiation reflected at the surface and travelling back up to the satellite. For a studied region, the brightness temperature can be rewritten as the linear sum of ice emission and ocean emission,

$$T_B = T_O C_O + T_I C_I, \quad (2.2)$$

where  $T_O$  is the brightness temperature of the ocean,  $C_O$  is the fraction of the region covered by ocean,  $T_I$  is the brightness temperature of the ice,  $C_I$  is the fraction of the region covered

by sea ice or sea ice concentration. Since  $C_O + C_I = 1$ , we can rewrite the last equation as

$$C_I = \frac{T_B - T_O}{T_I - T_O}. \quad (2.3)$$

Measuring  $T_B$ ,  $T_O$  and  $T_I$  is challenging since all the terms depends on surface temperature, atmospheric opacities and emissivity. To do so, one usually analyze three different frequencies. During winter or when the weather is dry, changes in emissivity and surface temperature can be taken into account effectively leaving only a 5% error on the sea ice concentration under optimal conditions. When the ice is scattered, the many types of surfaces - ocean, snow, first year ice, older ice - over the studied region increases the error up to 15%. During summer time, the emissivity of snow and ice is unpredictable and melt ponds are seen as ocean resulting in an error that can reach 25%. The error can be higher than 25% during severe storms and harsh weather. At the time of writing this thesis, the interior of the Arctic Ocean is still covered by highly concentrated sea ice allowing a satisfying level of confidence in satellite measurements. The National Snow and Ice Data Center (NSIDC) provides the satellite observations for the sea ice concentration.

### 2.2.1 Sea ice extent

To quantify how sea ice evolves, Arctic scientists study sea ice extent (SIE) over sea ice area (SIA). Sea ice extent is defined as the sum of all the studied region or grid cell area with more than 15% sea ice concentration while the sea ice area is the product of sea ice concentration and area. The value of 15% has been chosen based on the seven measures of ice-edge features by aircraft carrier reported in [Cavalieri et al. \(1991\)](#). They measured 11%, 20%, 20%, 13%, 15%, 15%, 15% sea ice concentration which averages at 15%. Studying sea ice extent is useful during summer where the surface melt and melt ponds appear as water even if sea ice is still present under a thin liquid layer. Because sea ice extent does not discard those regions unlike sea ice area, it gives a more reliable measurement of the total coverage of Arctic sea ice. Sea ice extent always covers a larger area than sea ice area, figure [2.5](#). Their evolution is close but not precisely the same. The four black dots display the four sea ice extent minimums of the 21<sup>st</sup> century: 2002 ([Serreze et al., 2003](#)), 2005, 2007([Stroeve et al., 2008](#)) and 2012

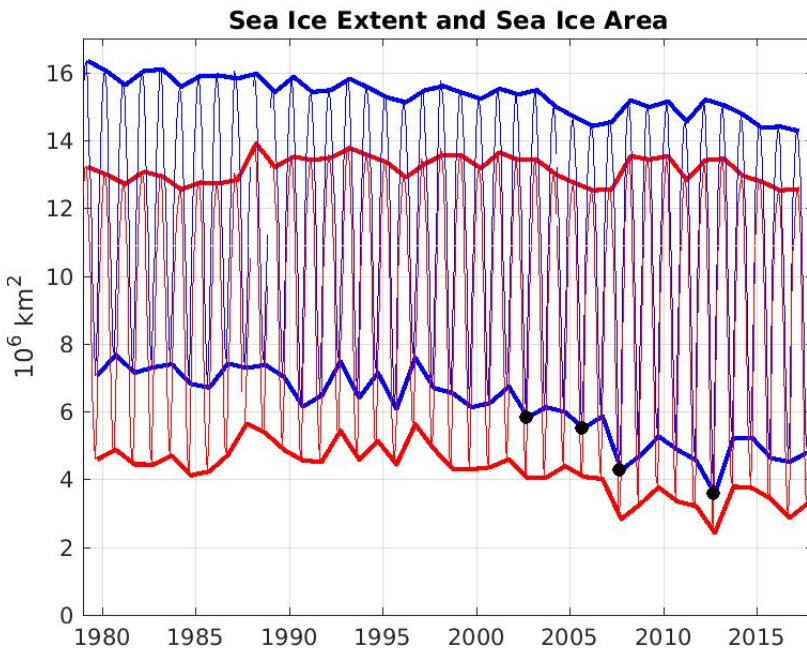


Figure 2.5: Sea ice extent in blue and sea ice area in red. Both curves are bound by their maximum or March area and minimum or September area. The four black dots display the four sea ice extent minima, 2002, 2005, 2007 and 2012. Data provided by the NSIDC [Fetterer et al. \(2017\)](#).

[\(Parkinson and Comiso, 2013\)](#).

### 2.2.2 Sea ice thickness

Sea ice thickness can be measured from different methods: (1) Upward Looking Sonar (ULS), (2) ElectroMagnetic (EM) sounding, (3) satellites or (4) direct measurement. The ULS can be attached to a submarine or moored on the sea bed. It calculates its own depth from the ambient pressure and the distance to ice from sonar reflection on the ice base ([Fissel et al., 2004](#)). The EM sounding device - called an EM bird - is towed by a helicopter and measures its distance to the sea ice by a laser altimeter and its distance to the ocean using a frequency unaffected by sea ice ([Haas et al., 2009](#)). The resulting ice thickness has an error of  $\pm 0.1 \text{ m}$ . The main satellites investigating sea ice are CRYOsat and ICESat. CRYOsat is developed by the European Space Agency (ESA) and ICESat by NASA (United States of America). They both calculate the distance from the first solid or liquid surface to the satellite, respectively [Laxon et al. \(2013\)](#) and [Zwally et al. \(2002\)](#). By using sea surface height measurement from

the satellite, it is possible to transform the sea ice height in sea ice thickness. [Lindsay and Schweiger \(2015\)](#) combined the results from ULS, EM sounding and satellites. They found that most measurements were in acceptable agreement with the annual mean sea ice thickness between 2000 and 2012. The annual mean sea ice thickness between 2000 and 2012 is roughly about 5 metres at the Northern part of Canada and decreases toward Russia down to one metre. They also found a rapid decrease in ice thickness. From 2000 to 2012, the yearly averaged ice thickness has declined by  $0.58 \pm 0.07 \text{ m}/\text{decade}$  which represents a loss of 34% while the September thickness declined by 50%. Using data from 1975 to 2012, the yearly averaged thickness decreased by 65% and the September thickness by 85%.

The worrying decay of ice in the Arctic inspired Andy Lee Robinson from Climate State to plot the dramatic Arctic Death Spiral (figure 2.6). It shows the decrease in monthly mean Arctic sea ice volume for each month from 1979 to 2017. Every month, approximately  $15 \cdot 10^3 \text{ km}^3$  of sea ice volume is lost over the time span. The Pan-Arctic Ice Ocean Modelling and Assimilation System (PIOMAS) provided the data. It consists of a coupled ocean-ice climate model. The ocean part is the Parallel Ocean Program (POP) model developed at Los Alamos ([Smith et al., 2010](#)). The ice model is a thickness-enthalpy distribution (TED) sea ice model using viscous plastic rheology ([Zhang and Rothrock, 2003](#)). The atmospheric forcing is derived from NCEP-NCAR reanalysis ([Kalnay et al., 1996](#)). PIOMAS showed reasonable agreement with observations.

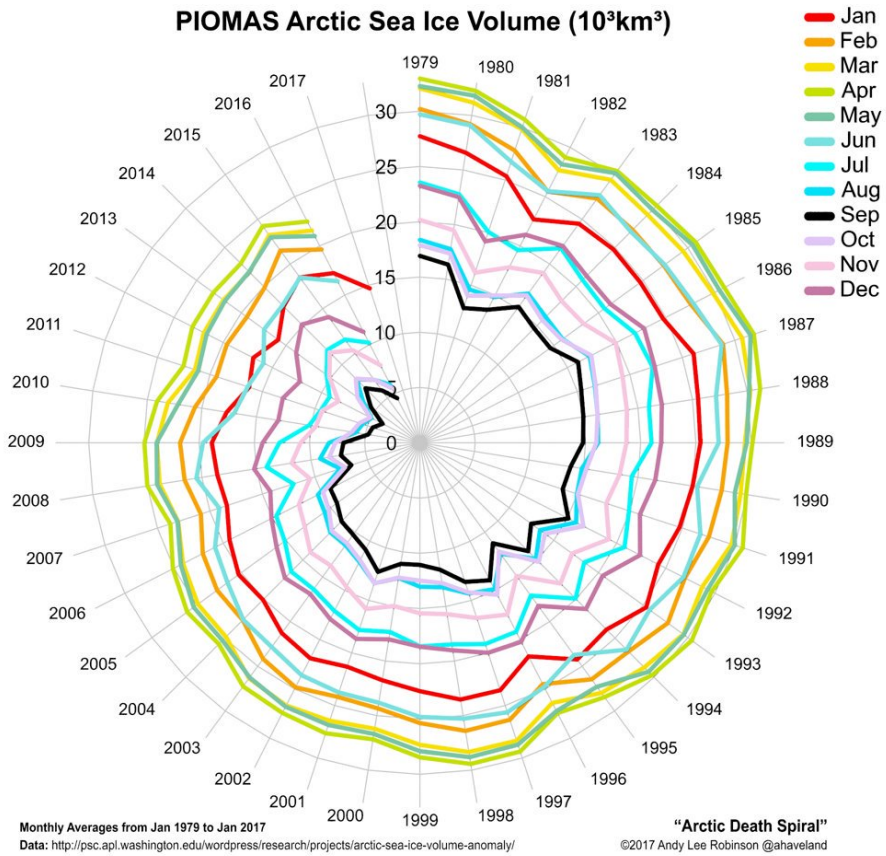


Figure 2.6: Arctic death spiral showing the evolution for each monthly sea ice volume between 1979 and 2017.

## 2.3 Feedback

The Arctic reacts more than the rest of the world to global warming because of overwhelming positive feedback processes (ACIA, 2005; Holland and Bitz, 2003). A positive feedback happens when a change in a system amplifies itself. For example, sea ice loss brings more sea ice loss. A negative feedback happens when a change in a system erodes itself. Four of the most important feedback are presented in this section: the ice-albedo feedback, thinner ice feedback, cloud-ice feedback and the thermohaline feedback.

The ice-albedo feedback is the most important feedback. Sea ice is highly reflective to shortwave solar radiation whereas ocean is a good absorber of solar radiation. The albedo or reflectivity of ocean water is 0.1, between 0.3 – 0.4 for land ice, between 0.5 – 0.7 for sea ice and between 0.75 – 0.95 for snow (Ahrens, 2009; NSIDC, 2013). If the area of open water

increases, the total absorption of solar radiation by the Arctic Ocean will be higher. This energy will lead to an increase in ocean surface temperature. A warmer ocean melts more sea ice, and therefore creates more open water.

A thinner sea-ice cover is weaker, deforms more easily and drifts faster for a given wind forcing. Sea-ice deformations primarily occur along leads where large gradient in the sea-ice velocity (shear) and some divergence or convergence are present. Divergence in the ice pack leads to more open water, more evaporation, and consequently more storms. Therefore, a stormier Arctic leads to more sea-ice deformation and faster drift. [Rigor et al. \(2002\)](#) showed that when the large-scale atmospheric circulation is more cyclonic with storms penetrating farther into the eastern Arctic, the wind pattern are such that it advects readily thick multi-year ice from the central Arctic through the Fram Strait. This was the case in the eighties and early nineties when a dramatic loss of multi-year ice was recorded ([Johannessen et al., 1999](#)).

The next mechanism is the cloud-ice feedback. If there are more clouds, there is less solar energy income during the summer. This leads to less summer melt and generally to a thicker sea-ice cover. However, liquid water clouds have a strong greenhouse effect and also lead to an increase in the downwelling surface longwave radiation and this, during the whole year ([Shupe and Intrieri, 2004; Gorodetskaya et al., 2008](#)). The resulting cloud-ice reaction is overall a positive feedback.

The last feedback is linked with the thermal insulation of the ocean. When the ice is thin, it is easier to form ice hence a negative feedback. New formed ice rejects brine. This extra brine builds a stronger cold halocline layer which insulates the top part of the Arctic Ocean and its sea ice from the warm Atlantic waters just as discussed earlier.

When global climate models include all the feedback processes, they predict the largest change of surface air temperature at high latitudes ([Holland and Bitz, 2003](#)). The ice-albedo feedback is likely to account for much of the warming. The Arctic is a magnifying glass for global warming. This is called polar amplification.

With this amplification, the Arctic Ocean could become seasonally ice free by 2050 ([Holland et al., 2006b; Stroeve et al., 2007, 2012; Wang and Overland, 2012](#)). All this occurs to the

detriment of any ice-dependent species such as narwhal, seal, polar bear, etc. (Laidre et al., 2008; Stirling and Derocher, 2012; TheCircle, 2012; Norris et al., 2002) A seasonal ice-free Arctic will lead to local warming of adjacent land and likely to an acceleration of permafrost melting which will release more greenhouse gas (Schaefer et al., 2012; Lawrence et al., 2008). Since the density of melted ice is not the same as the ocean, a fully melted Arctic would increase the sea level by an extra 47 mm (Noerdlinger and Brower, 2007) compared to 7 m for a fully melted Greenland and 60 m for a fully melted Antarctica estimated by Vaughan et al. (2013). Vulnerabilities will strengthen and develop in Inuit communities (Ford et al., 2006; Ford, 2009). On a more positive side, the maritime shipping routes through the Arctic Ocean will open reducing transport time, cost and pollution (Melia et al., 2016).

## 2.4 Community Climate System Model

In order to understand and anticipate the adversities of climate change over the Arctic, the scientific community uses Global Climate Models (GCMs). GCMs modelise the equations of climate on a global scale. Simulations start in the past up to present time and then uses predictions for the green house gases future evolution in order to estimate future climate. This thesis will focus on the results of the Community Climate System Model (CCSM) versions 3 and 4. The CCSM is a coupled climate model consisting of four modules, one for atmosphere, one for ocean, one for land, one for sea ice, and a coupler assuring communication between each module. The general results of the CCSM3 are described in Collins et al. (2006a) and in Gent et al. (2011) for the CCSM4. The CCSM3 uses the Community Atmospheric Model version 3 (CAM3) (Collins et al., 2004, 2006b), the Parallel Ocean Program (POP1) (Smith and Gent, 2004a), the Community Sea-Ice Model version 5 (CSIM5) (Briegleb et al., 2004) and the Community Land Model version 3 (CLM3) (Oleson et al., 2004; Dickinson et al., 2006; Bonan et al., 2002). The CCSM4 uses the Community Atmospheric Model version 4 (CAM4) (Neale et al., 2010), the Parallel Ocean Program version 2 (POP2) (Smith et al., 2010; Danabasoglu et al., 2012), the Los Alamos sea ice model version 4 (CICE4) (Hunke and Lipscomb, 2010) and the Community Land Model version 4 (CLM4) (Oleson et al., 2008; Stoeckli et al., 2008; Lawrence et al., 2011).

We will narrow our attention to the ocean and sea ice components of the models in sections 2.4.1 and 2.4.2 respectively. For each component, the basic equations used in both versions 3 and 4 as well as their differences are presented. A succinct presentation of the future scenarios used by the CCSM to forecast the climate up to 2100 follows in section 2.4.3. The following model discussion is technical and might be difficult to follow for beginners. It is more informative than explicative.

#### 2.4.1 CCSM ocean component - POP model

A derivation of the fluid equations and approximations can be found in [Vallis \(2006\)](#). The POP model solves the Navier-Stokes equations for  $u$ , the eastward velocity, and  $v$ , the northward velocity, on a sphere for a thin stratified fluid under the hydrostatic and Boussinesq ( $\rho = \rho_0$ ) approximation ([Smith et al., 2010](#)):

$$\frac{\partial}{\partial t} u + \mathcal{L}(u) - (uv \tan \phi)/a - fv = -\frac{1}{\rho_0 a \cos \phi} \frac{\partial P}{\partial \lambda} + \mathcal{F}_{Hx}(u, v) + \mathcal{F}_V(u) \quad (2.4)$$

$$\frac{\partial}{\partial t} v + \mathcal{L}(v) - (u^2 \tan \phi)/a + fu = -\frac{1}{\rho_0 a} \frac{\partial P}{\partial \phi} + \mathcal{F}_{Hy}(u, v) + \mathcal{F}_V(v) \quad (2.5)$$

$$\mathcal{L}(\alpha) = \frac{1}{a \cos \phi} \left[ \frac{\partial}{\partial \lambda} (u \alpha) + \frac{\partial}{\partial \phi} (\cos \phi v \alpha) \right] + \frac{\partial}{\partial z} (w \alpha) \quad (2.6)$$

$$\mathcal{F}_{Hx}(u, v) = A_M \left\{ \nabla^2 u + u(1 - \tan^2 \phi)/a^2 - \frac{2 \sin \phi}{a^2 \cos^2 \phi} \frac{\partial v}{\partial \lambda} \right\} \quad (2.7)$$

$$\mathcal{F}_{Hy}(u, v) = A_M \left\{ \nabla^2 v + v(1 - \tan^2 \phi)/a^2 + \frac{2 \sin \phi}{a^2 \cos^2 \phi} \frac{\partial u}{\partial \lambda} \right\} \quad (2.8)$$

$$\nabla^2 \alpha = \frac{1}{a^2 \cos^2 \phi} \frac{\partial^2 \alpha}{\partial \lambda^2} + \frac{1}{a^2 \cos^2 \phi} \frac{\partial}{\partial \phi} \left( \cos \phi \frac{\partial \alpha}{\partial \phi} \right) \quad (2.9)$$

$$\mathcal{F}_V(\alpha) = \frac{\partial}{\partial z} \mu \frac{\partial}{\partial z} \alpha, \quad (2.10)$$

where  $\lambda$  is the longitude,  $\phi$  is the latitude,  $z = r - a$  is the depth relative to mean sea level with  $a = 6.37122 \cdot 10^6 m$  being the Earth's radius,  $g = 9.80616 m^2/s$  is the acceleration due to gravity,  $f = 2 \cdot \sin \phi$  is the Coriolis parameter,  $\rho_0 = 1.026 g/cm^3$  is the background density of seawater,  $w$  is the vertical or radial velocity,  $P$  is the pressure,  $\Theta$  is the potential temperature,  $S$  is the salinity,  $A_M$  is the horizontal diffusion coefficient and  $\mu$  is the vertical mixing coefficient. The first term on the left-hand side of equations (2.5) and (2.6),  $\frac{\partial}{\partial t} u$  and  $\frac{\partial}{\partial t} v$ , is the temporal evolution of the horizontal velocities. The second and third terms on the left-hand side represent the advection of the velocities. The fourth and last term on the

left-hand side represents the Coriolis force. The first term of the right-hand side of (2.5) and (2.6) takes into account the pressure driven circulation. The second and third terms of the right-hand side contains velocity diffusion, both horizontal and vertical respectively. The second and third terms in brackets in equations (2.7) and (2.8) ensure that no stresses are generated due to solid-body rotation in a shallow layer (Williams, 1972). Wind forcing is applied as a boundary condition of the variable  $F_V$ . Bottom and lateral boundary conditions applied in POP are no-flux for tracers (zero tracer gradient normal to boundaries) and no-slip for velocities ( $u = v = w = 0$ ). The main parameterizations added are a mesoscale (sub-grid) eddy parameterization (Gent and Mcwilliams, 1990) and a vertical mixing K-profile parameterization (KPP) (Large et al., 1994)

The Boussinesq approximation stipulates that density changes has no effect on the circulation. Therefore, the continuity equation can be used to calculate the vertical velocity as a residual only after the horizontal velocities has been solved,

$$\mathcal{L}(1) = \frac{1}{a \cos \phi} \left[ \frac{\partial}{\partial \lambda} (u) + \frac{\partial}{\partial \phi} (\cos \phi v) \right] + \frac{\partial}{\partial z} (w) = \nabla \cdot \vec{u} = 0. \quad (2.11)$$

The hydrostatic approximation states that the pressure gradient is balanced by buoyancy only,

$$\frac{\partial p}{\partial z} = -\rho g. \quad (2.12)$$

The scalar variables or tracers such as potential temperature and salinity are calculated using the tracer transport equation,

$$\frac{\partial}{\partial t} \varphi + \mathcal{L}(\varphi) = D_H(\varphi) + D_V(\varphi) \quad (2.13)$$

$$D_H(\varphi) = A_H \nabla^2 \varphi \quad (2.14)$$

$$D_V(\varphi) = \frac{\partial}{\partial z} \kappa \frac{\partial}{\partial z} \varphi, \quad (2.15)$$

where  $A_H$  is the horizontal diffusion coefficients and  $\kappa$  is the vertical mixing coefficients. The surface heat fluxes or fresh water fluxes are applied as surface boundary conditions to vertical diffusive terms  $D_V$ . The first term of the left-hand side of the tracer equation is the temporal evolution of the tracer. The second term represents the tracer advection. The left-hand side contains the horizontal and vertical tracer diffusion.

Once the potential temperature and the salinity are solved, the CCSM calculates the density as a state function depending on potential temperature, salinity and depth. The resulting density field is used to calculate instabilities which can induce motion.

At the North Pole,  $\phi = 90^\circ$ , every term with a  $\frac{1}{\cos\phi}$  diverges. At the North Pole, latitudes and longitudes do not have defined derivatives. To avoid any problem with divergent terms, the CCSM chooses a grid with a displaced pole over Greenland (figure 2.7) with a nominal  $1^\circ$  resolution. It is also possible to choose a displaced pole over Canada or a tri-pole grid. To modify the POP model basic equations on a sphere to a different grid, we must use results from differential geometry (Pressley, 2010). Without going into details, the goal is to start with the equations using coordinates  $(\lambda, \phi, z)$  and end with the equations written with the new coordinates  $(q_x, q_y, z)$ . The differential length element,  $ds$ , is given by:

$$ds^2 = \xi_\lambda^2 + \xi_\phi^2 + dz^2 = \sum_{i,j=1}^2 h_{ij}^2 dq_i dq_j + dz^2 \quad (2.16)$$

$$h_{ij} = \sum_{k=1}^2 \frac{\partial \xi_k}{\partial q_i} \frac{\partial \xi_k}{\partial q_j}, \quad (2.17)$$

where  $\xi_k$  is the infinitesimal distance given by an infinitesimal change in  $\lambda$  ( $k = 1$ ) or  $\phi$  ( $k = 2$ ),  $h_{ij}$  is the metric coefficient of the new grid which depends on the local curvature of the new set of coordinates. This metric holds all the required information to rewrite the terms and operators of the equations.



Figure 2.7: CCSM grid with the North Pole displaced over Greenland.

The POP model uses a staggered Arakawa B-grid with tracers (scalar variables) at the centre of a cell and velocities  $u_x$  and  $u_y$  at the corners of the cell mid height as one can see on the left picture of figure 2.8. From this grid, two sub grid are considered: the T-grid (tracer-grid) and the U-grid (velocity grid). The T-grid has the tracers at the centre of the cell with velocities at its corners. The U-grid has velocities  $u_x$  and  $u_y$  at the centre of the grid and tracers at its corners. The vertical velocity,  $w$ , can be found at two locations. The first location is at the highest north-east corner of the cell and the second location is mid height on the north-east corner where the horizontal velocities are as one can see on the central panel of figure 2.8. The first location facilitates the advection calculation of the tracers while the second location facilitates the advection calculation of the velocities hence its superscript,  $w^u$ . The vertical discretization increases with depth as illustrated in the right panel of figure 2.8.

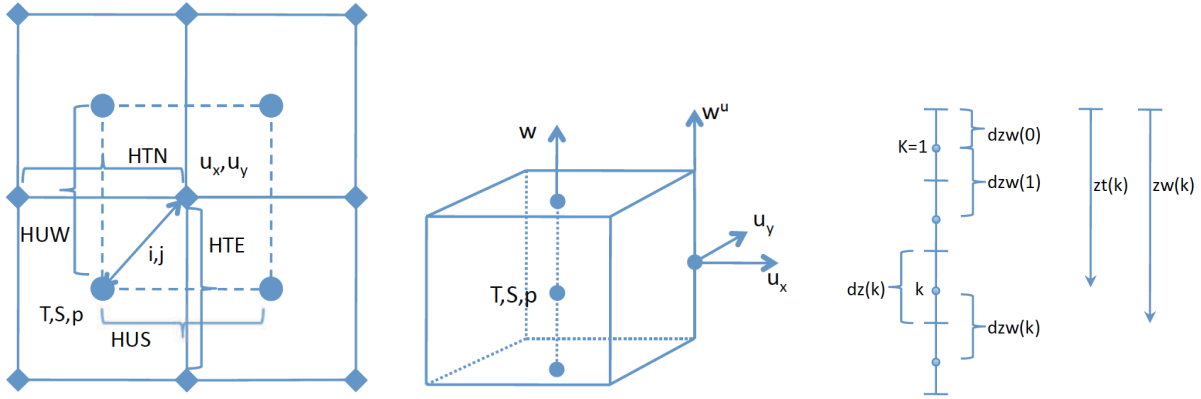


Figure 2.8: Left) Horizontal discretization of the grid showing the locations of tracers, velocities and lengths. Center) Vertical locations of tracers and velocities. Right) Vertical discretization. Taken from [Smith et al. \(2010\)](#).

The main improvements between the POP and the POP2 models are the increase of 40 vertical levels to 60 with a new bottom topography, the inclusion of the opening of Nares Strait, a near-surface eddy flux parameterization ([Ferrari et al., 2008](#)), vertically varying diffusive coefficients ([Ferreira and Marshall, 2006](#)), a submesoscale parameterization ([Fox-Kemper et al., 2008; Fox-Kemper and Ferrari, 2008; Fox-Kemper et al., 2011](#)), a deep overflow parameterization ([Briegleb et al., 2010](#)), and an abyssal tidally driven mixing parameterization ([Jayne, 2009](#)). [Jahn et al. \(2012\)](#) showed that the temperature-salinity profile of the CCSM4 worsens compared to CCSM3 compared to observations. The CCSM3 temperature-salinity profile agrees satisfactorily with observations. The CCSM4 has issues at all depth. The surface waters are too cold and too saline. Between 50 and 300 metres, the salinity is too low compared to observations while the temperature profile agrees with the observations. From 400 metres until the ocean floor, the temperature is too high and stays  $1^\circ C$  too high until the ocean floor with a salinity profile slightly too high. The observed warm Atlantic waters are located at 400 metres while the simulations place them at 750 meters. The simulated Atlantic waters in the Arctic Ocean are too deep and too warm. The CCSM3 temperature-salinity profile agreed better with observations. The general shape of the ocean circulation agrees with observations specially the inflow from the Fram Strait and the Barents and Kara seas, the cyclonic boundary current around the marginal seas, the Canadian Basin gyre, the

return flow along the Lomonosov Ridge and the return current west and north of Svalbard. The velocities are too low at the gates of the Arctic Ocean but the temperature agrees with observations leading to wrong heat fluxes entering and exiting the Arctic Ocean.

#### 2.4.2 CCSM sea ice component - CICE model and CSIM

From [Hunke and Lipscomb \(2010\)](#), the fundamental equation solved by CICE is ([Thorndike et al., 1975](#))

$$\frac{\partial g}{\partial t} = -\nabla \cdot (g\vec{u}) - \frac{\partial}{\partial t}(fg) + \psi, \quad (2.18)$$

where  $g$  is the ice thickness distribution function defined as  $g(\vec{x}, h, t)dh$  being the fractional area covered by ice in the thickness range  $(h; h + dh)$  at a given time and location,  $\vec{u}$  is the horizontal ice velocity vector,  $f$  is the rate of thermodynamic ice growth and  $\psi$  is a ridging redistribution function.

This equation is discretized horizontally on the same horizontal grid as the ocean model and in discrete thickness categories. The thickness does not become discrete, the ice still changes continuously inside its thickness category. As an example, consider a two thickness category model where the first category ranges from 0 to 1 m and the second category includes any ice thicker than 1 m. This model allows a cell with a section with sea ice less thick than 1 m and another section with ice thicker than 1 m. At the beginning of winter, the first category could start with 30% of 50 cm and 70% of 2 m sea ice. Through the cold season, both category will grow, possibly at different rate. When the first category grows up to 1 m, its sea ice will be transferred to the next category. The thickness discretization allows a number of different thicknesses inside a same cell. Without it, a cell would have one averaged thickness.

The CICE models follows three steps at each time step to solve the fundamental equation (2.18): 1) calculation of the sea ice velocities,  $u$  and  $v$ , 2) transport and ridging of sea ice accompanied with tracer transport, 3) thermodynamic processes growing and melting sea ice, affecting the temperature and salinity profiles. Each steps is explained more thoroughly in the next paragraphs.

The CICE model starts by solving ice dynamics using an elastic-viscous-plastic (EVP)

model ([Hunke and Dukowicz, 1997](#)). The EVP models treats the ice pack as a plastic material under typical stress conditions but behaves as an elastic-viscous fluid where strain rates are small. The equations of the sea ice dynamics are

$$m \frac{\partial \vec{u}}{\partial t} = \nabla \cdot \sigma + \vec{\tau}_a + \vec{\tau}_w - m f \hat{k} \times \vec{u} - m g \nabla H_0 \quad (2.19)$$

$$\vec{\tau}_a = c_a \cdot \rho_a \cdot |\vec{U}_a| \cdot (\vec{U}_a \cos \phi + \vec{k} \times \vec{U}_a \sin \phi), \quad (2.20)$$

$$\vec{\tau}_w = c_w \cdot \rho_w |\vec{U}_w - \vec{u}| [(\vec{U}_w - \vec{u}) \cos \lambda + \vec{k} \times (\vec{U}_w - \vec{u}) \sin \lambda], \quad (2.21)$$

where  $m$  is the combined mass of ice and snow per unit area,  $\vec{\tau}_a$  and  $\vec{\tau}_w$  are the wind and ocean stresses,  $\sigma$  is the internal stress tensor containing the EVP characteristics of the ice model,  $m f \hat{k} \times \vec{u}$  is the Coriolis force and  $m g \nabla H_0$  is the effect of the sea surface slope. The details of the internal stress tensor can be found in [Hunke and Lipscomb \(2010\)](#).

With the updated velocities, CICE calculates the transport and ridging of sea ice through three variables: 1) sea ice concentration  $a_{in}$  for a given grid cell and for a given thickness category  $n$ , 2) sea ice volume  $v_{in} = a_{in} \cdot h_{in}$  where  $h_{in}$  is the ice thickness and 3) internal ice energy for a given vertical layer  $k$ ,  $e_{ink} = \frac{v_{in}}{N_i} \cdot q_{ink}$  where  $N_i$  is the total number of ice categories and  $q_{ink}$  is the ice layer enthalpy which is minus the amount of energy required to melt a unit volume of ice and raise its temperature to  $0^\circ C$ . The transport equations are:

$$\frac{\partial a_{in}}{\partial t} + \nabla \cdot (a_{in} \vec{u}_i) = 0, \quad (2.22)$$

$$\frac{\partial v_{in}}{\partial t} + \nabla \cdot (v_{in} \vec{u}_i) = 0, \quad (2.23)$$

$$\frac{\partial e_{ink}}{\partial t} + \nabla \cdot (e_{ink} \vec{u}_i) = 0. \quad (2.24)$$

The equations of ridging, variable  $\psi$  in equation (2.18), are described in [Lipscomb et al. \(2007\)](#). The CICE model uses elastic-viscous-plastic (EVP) equation for sea ice. A similar set of equations is prescribed in the CICE model for snow over sea ice.

Tracers transport is calculated using the updated velocities,

$$\frac{\partial a_{in} T_n}{\partial t} + \nabla \cdot (a_{in} T_n \vec{u}_i) = 0, \quad (2.25)$$

$$\frac{\partial v_{in} T_n}{\partial t} + \nabla \cdot (v_{in} T_n \vec{u}_i) = 0, \quad (2.26)$$

$$\frac{\partial v_{sn} T_n}{\partial t} + \nabla \cdot (v_{sn} T_n \vec{u}_i) = 0, \quad (2.27)$$

Where  $T_n$  denotes the tracer value for the sea ice thickness category  $n$ .

Once the transport is calculated, the CICE model considers thermodynamics of sea ice.

The thermodynamics of sea ice include surface and bottom forcing, temperature and salinity changes, melt and growth. The surface forcings are given by

$$F_0 = F_s + F_l + F_{lw} + (1 - \alpha)(1 - i_0)F_{sw}, \quad (2.28)$$

where  $F_s = C_s(\Theta_a - T_{sf})$  is the sensible heat flux with  $C_s$  being a nonlinear turbulent heat transfer coefficient and  $\Theta_a$  being the atmosphere's surface potential temperature,  $F_l = C_l(Q_a - \frac{q_1}{\rho_a} \exp(-\frac{q_2}{T_{sf}}))$  is the latent heat flux with  $C_l$  being a nonlinear turbulent heat transfer coefficient and  $Q_a$  being the atmosphere's specific humidity at the surface,  $F_{lw} = \epsilon F_{lw\,a} - \epsilon \sigma_{SB} T_{sf}^4$  is the longwave heat flux with  $\epsilon = 0.95$  being the emissivity of snow or ice,  $F_{lw\,a}$  being the longwave atmospheric radiation reaching sea ice and  $\sigma_{SB}$  is the Stefan-Boltzmann constant,  $\alpha$  is the albedo of sea ice,  $1 - i_0$  is the fraction of absorbed shortwave flux that penetrates into the ice,  $F_{sw}$  is the incoming short wave radiation. The albedo and penetrative fraction of short wave radiation depend on sea ice thickness, surface ice optical properties, presence of melt pond or snow. They are calculated by the model. The bottom heat flux between the ocean and sea ice,  $F_{bot}$ , is given by

$$F_{bot} = -\rho_w \cdot c_w \cdot c_h \cdot u_* \cdot (T_w - T_{fr}), \quad (2.29)$$

where  $\rho_w$  is the water density,  $c_w$  is the water heat capacity,  $c_h$  is the heat exchange coefficient,  $u_* = \sqrt{|\tau_w|/\rho_w}$  is the friction velocity,  $|\tau_w|$  is the norm of the shear stress given by  $\rho_w \sqrt{\frac{\partial u}{\partial y}^2 + \frac{\partial v}{\partial x}^2}$ ,  $T_w$  is the surface water temperature,  $T_{fr} = -1.8^\circ C$  is the freezing temperature of ocean water.

The vertical salinity profile is prescribed. The midpoint salinity  $S_{ik}$  in each ice layer  $k$  is given by

$$S_{ik} = \frac{1}{2} S_{max} [1 - \cos(\pi z^{\frac{a}{b}})], \quad (2.30)$$

where  $z = (k - 1/2)/N_i$ ,  $S_{max} = 3.2$  psu and  $a = 0.407$  and  $b = 0.573$  ([Hunke and Lipscomb, 2010](#)). The snow is assumed to be fresh. The temperature profile of sea ice,  $T_i$ , is given by

$$\rho_i \cdot c_i \cdot \frac{\partial T_i}{\partial t} = \frac{\partial}{\partial z} \left( K_i \frac{\partial T_i}{\partial z} \right) - \frac{\partial I_{pen}}{\partial z}, \quad (2.31)$$

where  $\rho_i$  is the sea ice density assumed to be constant and uniform,  $c_i(T, S)$  is the specific heat of sea ice,  $K_i(T, S)$  is the thermal conductivity of sea ice,  $I_{pen}(z)$  is the solar penetrative radiation at depth  $z$ .

Melt is split into three processes based on the location of the melting: surface, bottom and lateral. Surface melting is calculated as:

$$\Delta h = (F_0 - F_{ct})/q \quad (2.32)$$

$$F_{ct} = K_h \cdot (T_{surf} - T_q), \quad (2.33)$$

where  $\Delta h$  is the change in thickness,  $F_{ct}$  is the heat conduction at the top of the ice,  $q$  is the enthalpy of pure ice,  $T_{surf}$  is the temperature at the surface of the ice. Bottom melting or growth is given by

$$\Delta h = \frac{F_{cb} - F_{bot}}{q} \Delta t, \quad (2.34)$$

$$F_{cb} = K_h \cdot (T_q - T_{bot}), \quad (2.35)$$

$$F_{bot} = -\rho_w \cdot c_w \cdot c_h \cdot u_* \cdot (T_w - T_{fr}), \quad (2.36)$$

where  $F_{cb}$  is the conductive heat flux through the bottom of the ice,  $q = -\rho_i(-c_0(\mu S + T) + L_0(1 + \mu S/T) + c_w \mu S)$  is the enthalpy of the ice with  $c_0 = 2106 \text{ J/kg/K}$  the specific heat of fresh ice at  $0^\circ\text{C}$ ,  $L_0 = 334000 \text{ J/kg}$  the latent heat of fusion of fresh ice at  $0^\circ\text{C}$  and  $\mu = 0.054 \text{ K/psu}$  the ratio between the freezing temperature and salinity of brine,  $\Delta t$  is the time step,  $K_h$  is the heat conductivity of sea ice,  $T_q$  is the temperature of sea ice calculated from enthalpy  $q$ ,  $T_{bot}$  is the temperature at the base of the ice,  $\rho_w$  is the water density,  $c_w$  is the water heat capacity,  $c_h$  is the heat exchange coefficient,  $u_* = \sqrt{|\tau_w|/\rho_w}$  is the friction velocity,  $|\tau_w|$  is the norm of the shear stress given by  $\rho_w \sqrt{\frac{\partial u^2}{\partial y} + \frac{\partial v^2}{\partial x}}$ ,  $T_w$  is the water temperature,  $T_{fr}$  is the water freezing temperature. If  $\Delta h$  is positive, basal growth is occurring. If  $\Delta h$  is negative, bottom melting is occurring. Another process adds bottom ice: frazil ice. Frazil ice develops as supercooled droplets which form small crystals of ice in the mixed layer and, due to their

buoyancy, reach the surface of the ocean. It is calculated as:

$$frazil = \frac{(T_{fr} - T_w) \cdot c_w \cdot \rho_w \cdot h_{mix}}{q_0} \quad (2.37)$$

where  $h_{mix}$  is the thickness of the ocean mixed layer,  $q_0$  is the enthalpy of newly formed ice. Finally, lateral melting is calculated as

$$F_{side} = rside \cdot E_{tot}, \quad (2.38)$$

$$rside = \frac{m_1 \cdot (T_w - T_{bot})^{m_2} \cdot \pi}{\alpha \cdot f_D}, \quad (2.39)$$

where  $E_{tot}$  is the total energy available to melt ice and snow,  $m_1 = 1.6 \cdot 10^{-6}$  and  $m_2 = 1.36$  are coming from [Maykut and Perovich \(1987\)](#),  $\alpha = 0.66$  from [Steele \(1992\)](#),  $f_D$  is the flow diameter set at 300 m. Note that the surface and bottom melt impact sea ice area when the sea ice thickness reach the thinnest thickness layer; half of the energy goes to reducing thickness while the other half goes to reducing sea ice area.

The main differences from the CSIM5 to CICE4 are an improved ridging scheme ([Lipscomb et al., 2007](#)), a melt pond parameterization ([Holland et al., 2011](#)) and a new radiative transfer scheme ([Briegleb and Light, 2007](#)) which includes effect of melt pond and absorber such as black carbon and dust on optical properties of sea ice.

The seasonal cycle of the sea ice extent of the CCSM3 was too high during winter and slightly too high during summer ([Holland et al., 2006c](#)). The CCSM4 solved both problems agreeing better with observations ([Jahn et al., 2012](#)). The CCSM3 sea ice concentration is extending too far outside the Arctic Ocean while the CCSM4 contains it better ([Gent et al., 2011](#)). The trend of sea ice extent between 1981 and 2005 is not well represented in the CCSM4 with 2 runs not simulating any significant loss. The CCSM4 has thicker ice close to Canada agreeing better with the observations than the CCSM3. The CCSM4 sea ice is too thick in the centre of the Arctic Ocean and it lacks multiyear ice ([Jahn et al., 2012](#)). The CCSM4 sea ice motion shows the standard large scale features such as the Beaufort Gyre and the Transpolar Drift Stream. Though, the simulated ice speeds are too large and show a wider distribution compared with observations.

### 2.4.3 Future projections

The CCSM simulates the present climate and projections of future climate up to 2099. The Intergovernmental Panel on Climate Change (IPCC) published studies of future projections of green house gases ([IPCC, 2007, 2013](#)). Those green house gases reflect energy that would have normally escaped our atmosphere. The sum of all the extra energy from all the green house gases is called radiative forcing. The radiative forcings for the Special Report on Emissions Scenarios (SRES) ([IPCC, 2007](#)) and the Representative Concentration Pathways (RCP) ([IPCC, 2013](#)) are shown in figure 2.9. The SRES includes six families of scenario: A1FI, A1B, A1T, A2, B1, and B2. This thesis focus strictly on SRES A1B. The RCP includes four different pathways: RCP2.5, RCP 4.5, RCP6.0, RCP8.5. The scenarios RCP8.5 and RCP6.0 strictly increase while RCP4.5 stabilizes by 2070 and RCP2.5 peaks at  $3\text{ W/m}^2$  by 2040 and then decreases. Note that before 2060, RCP4.5 is stronger than RCP6.0. The same happens for the SRES A1B and A2. Before 2050, SRES A1B is stronger than A2 even if by 2100 A2 has a higher radiative forcing than A1B. Those periods of higher forcing for weaker scenarios can have an important impact on the climate. If an important event happens due to the higher radiative forcing during those years, the simulated climate could be significantly different.

## 2.5 Conclusion

The Arctic is the northern portion of planet Earth. At its center lies the Arctic Ocean covered by sea ice. Warm waters enter through the Bering Strait, east of Fram Strait as the West Spitzbergen Current, and through the Barents Sea. Cold waters exit through the Canadian Arctic Archipelago and west of Fram Strait as the East Greenland Current. The Arctic Ocean is characterized by a cold halocline layer between  $50\text{ m}$  and  $200\text{ m}$  deep. The cold halocline layer insulates the surface ocean and its sea ice from the warm Atlantic layers  $300\text{ m}$  deep.

The sea ice is a complex material that under specific circonstances can reject its brine or keep it. The sea ice concentration of a defined region is measured by a satellite radiometer. The error on such measurements can reach up to 25%. Sea ice extent includes all area with

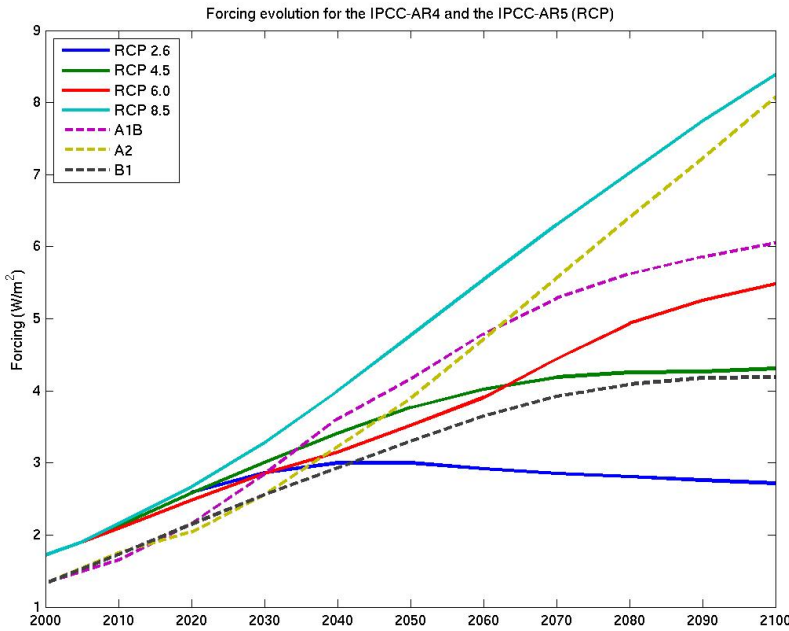


Figure 2.9: Radiative forcing evolution of the different scenarios of the IPCC-AR4 (A1B, A2, B1) and IPCC-AR5 (RCPs).

more than 15%. It counteracts most of the error on sea ice concentration. Sea ice extent is minimum over the month of September. September sea ice extent reached new low records in 2002, 2005, 2007 and 2012. Sea ice thickness is complicated to measure and observations are scarce both spatially and temporally. It can be done with the help of Ultra Light Sonar, Electromagnetic Sounding, satellites or drilled holes. All observations point to a decrease in sea ice thickness. The sea ice thickness decreased comparably more than sea ice extent.

The Arctic reacts more quickly and more intensely to climate changes. As the sea ice extent decreases, more open water is accessible to the solar radiation. While the sea ice reflects most of the solar radiation, the ocean absorbs most of it. The exposed water gets warmer and melt more sea ice which leaves more open water. It is a positive feedback named the Albedo feedback. It could thaw all summer sea ice in the next decades to come.

[Holland et al. \(2006a\)](#) observed abrupt reductions of Arctic September sea ice extent in the seven CCSM3 simulations forced by the SRES A1B leading to a summer ice free Arctic Ocean as soon as 2050. They stipulated that one to two years prior the abrupt loss of sea ice extent, pulses of ocean advective heat flux might have preconditioned the sea ice to a rapid loss. The thermodynamic interactions between the sea ice and the ocean is not well

documented. It is usually calculated as a residual of all the sea ice forcings and the change in sea ice thickness. This thesis aims at describing the exchanges of heat between the sea ice and the ocean plus the sources of ocean heat reaching the sea ice.

In order to proceed, the seven CCSM3 simulations forced by the SRES A1B will be studied. The CCSM3 has four modules - ocean, sea ice, land, atmosphere - and a coupler linking each parts. The ocean component is the POP model. It solves the Navier Stokes equations for a thin stratified fluid under hydrostatic equilibrium and Boussinesq approximation. The POP model uses a staggered Arakawa B grid with a displaced North Pole. The sea ice components is the CICE model. It has the same grid as the POP model. It solved the advection and forcings of sea ice. Its sea ice is elastic-viscous-plastic (EVP). One cell has five thickness categories plus open water. The CCSM3 has limited outputs making some analyses impossible. The CCSM4 is also studied for its extensive outputs.

Chapter 3 investigates all the processes affecting sea ice focussing on the seven CCSM3 simulations forced by the SRES A1B. Chapter 4 presents how to calculate all the energy fluxes affecting the surface ocean layer. The CCSM4 having numerous outputs, the heat budget is more readily to compute. Chapter 5 shows an analysis of the advective heat fluxes through the gates of the Arctic Ocean. Both the CCSM versions 3 and 4 are compared.

### 3 Physical processes affecting sea ice in the Community Climate System Model (CCSM) version 3

The interactions between the ocean and the sea ice are difficult to measure directly. For that reason, our understanding of those interactions is limited. Models allow profound analysis of the ocean-sea ice dynamic though. We decided to use the results of the CCSM version 3 to examine the scope of the physical processes affecting sea ice and the different simulations between themselves. The CCSM is a global climate model. Its third version predicts the increase of green house gases and warming following the SRES. The three main scenarios of the SRES are: B1 scenario being optimistic with 550 ppm CO<sub>2</sub> by 2100, the pessimistic A2 scenario with 850 ppm and the reasonable, *middle of the road*, A1B scenario with 720 ppm (IPCC, 2007). The SRES A1B is considered the most probable and acceptable scenario since it is a middle of the road scenario. It can satisfy the environmentalist and the conservators. Making it the most suitable and convincing scenario for our future. Though the A1B scenario is between A2 and B1 by 2100, it possesses the highest forcing before 2060 - the period exhibiting rapid sea ice decline. More information on the future scenarios can be found in section 2.4.3.

Holland et al. (2006a) found out that the seven simulations of the CCSM3 under the SRES A1B depicted abrupt reductions of Arctic September sea ice extent with an ice-free summer as early as 2040. This paper received a lot of attention<sup>2</sup>. The idea of an ice-free summer Arctic Ocean as soon as 2040 under a *reasonable* scenario with nonlinear evolution of the sea ice extent was unheard of.

This chapter investigates all the sources of sea ice loss with a special interest for thermodynamic processes in conjunction with the years of abrupt loss of September sea ice extent. To do so, we narrow our investigation to the SRES A1B simulations of the CCSM3 which are the same ones used in Holland et al. (2006a). Their main results are presented in section 3.1. An overview of the role of the Arctic Ocean on sea ice melting is presented in section 3.2. We directed our attention on sea ice volume, section 3.3, because any variations in ther-

---

<sup>2</sup>Cited 359 times. Verified on <https://apps.webofknowledge.com> May 26, 2017.

modynamic balance causes the sea ice volume to change. Section 3.3 marks the beginning of original results. The contributions to volume and area changes from dynamic and thermodynamic sources are presented in section 3.4. The sea ice flushed out through each gates of the Arctic Ocean is described in section 3.5. Thermodynamic processes are examined in section 3.6. They include surface, bottom and lateral melt and basal and frazil sea ice formation. A discussion of all the processes is presented in section 3.7.

### 3.1 Rapid declines

Holland et al. (2006a) defined an abrupt loss event to be an event for which the time derivative of the five-year running mean of September sea ice extent exceeds  $-0.5$  million  $km^2/y$ . When such events arose during the CCSM3 simulations, the average sea ice thickness in March declined rapidly but not in a surprising manner; there has been previous rapid decline of March thickness steeper than during the abrupt loss events. They found that the relative anomalies of ocean heat transport into the Arctic Ocean and absorbed short-wave radiation by the Arctic Ocean are highly correlated. It suggests that ocean heat transport is an important vector of sea ice loss which leaves more open water absorbing short-wave radiation. This hypothesis is supported by a one to two-year lag between the ocean heat transport and the sea ice thickness; the peaks of ocean heat transport come one to two years before sea ice thickness peaks. Once the initial loss is triggered by ocean heat transport, the albedo feedback kicks in leading to an ice-free Arctic Ocean during summer time.

For simplicity, The Arctic domain considered in this thesis follows constant latitude or longitude index in the rotated grid, see figure 3.1. The domain has a total ocean area of  $8.57 \cdot 10^6 km^3$ . All fluxes are stored in units of  $W/m^2$ . A spatial average of the flux requires to weigh the variable by the surface area to obtain units of power, watts, sum over the domain and then divide by the total area,

$$\bar{F} = \frac{\int F dA}{A} = \frac{\sum F \cdot A_{cell}}{A_{total}}. \quad (3.1)$$

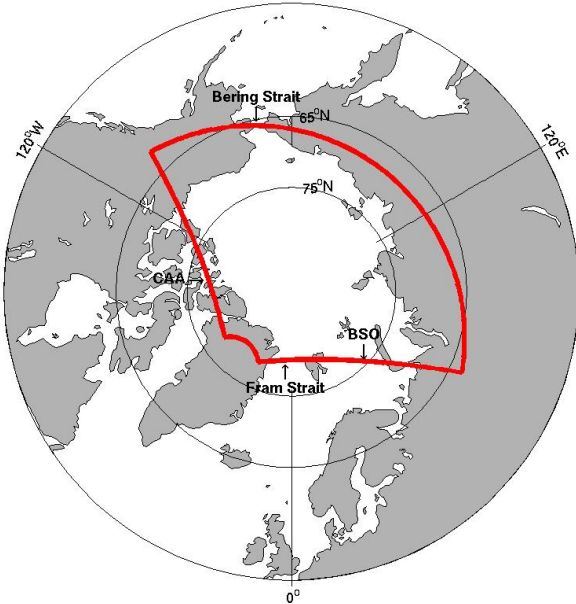


Figure 3.1: Arctic Ocean domain including the four main gates considered in this study: Fram Strait, Barents Sea Opening (BSO), Bering Strait and Canadian Arctic Archipelago (CAA). For simplicity, All gates are defined along lines of constant latitude or longitude index in the rotated grid.

### 3.2 Ocean to sea ice thermodynamic interactions

This section gathers important results on the thermodynamic interaction between the Arctic Ocean and its sea ice. It discusses: (1) the theoretical value for the ocean-sea ice heat flux along measurements supporting it, (2) measurements contradicting the theoretical value, (3) impact of the warm Atlantic waters on sea ice; these warm Atlantic waters are located 300 metres deep and could melt the entire Arctic sea ice if its energy reached the surface.

[Maykut and Untersteiner \(1971\)](#) determined that a constant ocean to sea ice heat flux of  $2\text{-}4 \text{ W/m}^2$  throughout the whole year is necessary to reproduce the measured sea-ice thickness evolution during a full seasonal cycle using a one-dimensional thermodynamic sea-ice model forced with observed radiative and turbulent heat fluxes. They also showed that with an extra  $8 \text{ W/m}^2$  of oceanic heat flux, the amount of ice melting in the summer is greater or equal to the amount of ice formation during winter, leading to an ice-free summer. This yearly average of  $2 \text{ W/m}^2$  is the expected value for the ocean-sea ice heat flux. [McPhee and Untersteiner \(1982\)](#) measured ocean heat fluxes that are close to  $2 \text{ W/m}^2$  from March to

May north of the Fram Strait supporting the results from [Maykut and Untersteiner \(1971\)](#). The experiment consisted of a thermocouple string and two thickness gauges on three sites distant by 150 metres forming a triangle. Ocean heat, sea ice latent and sensible heat are causing sea ice thickness changes. The thermocouple string measurements allow a calculation of the conductive heat flux through sea ice and sensible heat flux. The thickness gauge measurements allow a calculation of the sea ice thickness changes and latent heat flux. The only missing input is the ocean heat transfer to sea ice. It is calculated as the residual of all the other terms,

$$F_{ocn} = \frac{dh}{dt} - F_{lat} - F_{sens}. \quad (3.2)$$

[McPhee et al. \(2003\)](#) recorded an averaged oceanic heat flux of  $2.6\text{ W/m}^2$  using a buoy deployed close to the North Pole that drifted through the Fram Strait. When the buoy reached the Yerkman Plateau (North of Svalbard), the oceanic heat flux reached values as high as  $22\text{ W/m}^2$ . The sharp bathymetry and the absence of cold halocline layer led to a large ocean heat flux linked with tidal waves.

Many measurements point to a higher ocean-sea ice heat flux than the expected  $2\text{-}4\text{ W/m}^2$ . [Perovich et al. \(1989\)](#) calculated an averaged oceanic heat flux of  $14\text{ W/m}^2$  from a buoy moving through the Fram strait from December 14th<sup>th</sup> 1987 to January 2nd<sup>nd</sup> 1988. By the end of December 1987, the buoy entered warm water and measured an ocean heat flux of  $128\text{ W/m}^2$ . Using the 1975 Arctic Ice Dynamics Joint EXperiment (AIDJEX) data, [Maykut and McPhee \(1995\)](#) calculated a strong seasonal cycle of the ocean to sea ice heat flux with a yearly average of  $5.1\text{ W/m}^2$ . The maximum values of the ocean to sea ice heat flux were of  $40\text{--}60\text{ W/m}^2$  in August and almost zero in winter. The experiment consisted of Conductivity-Temperature-Depth (CTD) profilers from four drifting stations. They also concluded that the energy was mainly coming from solar short-wave radiation through sea ice rather than vertical advection of warmer waters. [Perovich and Elder \(2002\)](#) observed values of ocean to sea ice heat fluxes of  $2\text{ W/m}^2$  during fall, winter and spring and values around  $33\text{ W/m}^2$  during the summer months when solar radiation enters the ocean's surface through leads and open water, causing basal ice melt. The measurements were done at the Surface HEat Budget of the Arctic (SHEBA) experiment located North of Alaska in the Beaufort Sea and

Chukchi Sea. They used an Ice-Mass-Balance (IMB) buoy and treated the oceanic heat flux as a residual following [McPhee and Untersteiner \(1982\)](#).

The warm Atlantic waters located between 200 and 500 metres deep are a major threat to Arctic sea ice. If its energy reached the surface, the Arctic sea ice would vanish. [Timmermans et al. \(2008\)](#) used Ice-Tethered Profilers (ITP) to determine the vertical ocean heat flux in the Canada Basin. They calculated vertical ocean heat fluxes via double-diffusive staircase between 0.05 and  $0.3 W/m^2$ . This is consistent with observed diffusivity coefficients of the order of  $10^{-6} m^2/s$  obtained from measurements made in 2005 in the Canada Basin, in the Lomonosov Ridge region and the Amundsen Basin by [Rainville and Winsor \(2008\)](#). [Lique et al. \(2013\)](#) obtained the same results from four deployed moorings as part of the Beaufort Gyre Observing System in the Canada Basin during August 2003 and August 2011. On the other hand, during SHEBA a lead opened where the measuring equipment was and [McPhee et al. \(2005\)](#) showed that the heat flux along this active lead was as large as  $400 W/m^2$ . The mechanism invoked to explain such large heat fluxes is Ekman pumping associated with a positive curl in the surface ice-ocean stresses ventilating relic heat trapped beneath the mixed layer from previous summers. More information on Ekman pumping in [Vallis \(2006\)](#)

In summary, even if the expected value for the Arctic ocean-sea ice heat flux is a constant  $2-4 W/m^2$ , a strong seasonal cycle has been recorded varying from  $0 W/m^2$  in winter up to  $60 W/m^2$  in summer. The ocean-sea ice heat flux exhibits high spatial differences with higher values such as  $128 W/m^2$  close to the gates of the Arctic Ocean. The warm Atlantic waters' energy is well confined to its depth with very low vertical heat fluxes though under leads, ridges or storm, the vertical ocean heat flux can reach  $400 W/m^2$ . All the ocean-sea ice heat fluxes presented here were calculated from changes in sea ice thickness or volume. From measurements, ocean to sea ice heat exchange is an impactful component of melt and sea ice formation. Therefore it is important to study it in climate models. In order to understand the role of heat fluxes on sea ice extent, one must start by inspecting sea ice volume.

### 3.3 Sea ice volume

Sea ice volume is always affected by dynamic and thermodynamic processes unlike sea ice extent. When the sea ice concentration of a defined zone - a grid cell for example- increases over 15% its full area is added to the sea ice extent. If the sea ice concentration decreases under 15%, its full area is subtracted from the sea ice extent. The variations in sea ice extent are not continuous and the sea ice can change significantly before the sea ice extent varies accordingly. The sea ice concentration is directly affected by dynamic processes which consist of moving a parcel of sea ice from one location to another. It transfers the sea ice concentration from a region/cell to another. In contrast, thermodynamic processes do not necessarily affect sea ice concentration. Sea ice thickness can grow or melt without influencing the sea ice concentration. For example, consider a fully covered region with two metres thick sea ice growing up to three metres. In this example the sea ice concentration does not change, only the volume.

Sea ice volume better represents the state of sea ice and the effect of physical processes on it. However, most studies focus on sea ice extent. It is because sea ice extent observations are more reliable than sea ice thickness or volume that scientists are more interested in sea ice extent. Models are not restrained as are observations. It is possible to study sea ice volume and every processes associated to it if they are correctly output. This section covers: (1) a comparison between sea ice volume and sea ice extent in the literature, (2) the sea ice volume calculation in the CICE model and (3) a description of the evolution of the sea ice volume for the six simulations of the A1B SRES of the CCSM3.

[Overland and Wang \(2013\)](#) defined the study of sea ice volume over sea ice extent as *trendsetters*. Two groups of *trendsetters* are active: [Schweiger et al. \(2011\)](#) and [Maslowski et al. \(2012\)](#). [Schweiger et al. \(2011\)](#) use PIOMAS results for sea ice volume. The NSIDC sea ice extent trend during the 1979 to 2012 period has been of  $-14.2\%/decade$  while the PIOMAS sea ice volume trend for the same period is of  $-27.8\%/decade$  or  $-2.8 \cdot 1000 \text{ km}^3/y$ . The sea ice volume is changing at a faster rate than sea ice extent implying that sea ice volume offers a more insightful understanding of sea ice decline than sea ice extent. [Maslowski et al. \(2012\)](#) used the Naval Postgraduate School Arctic Modelling Effort (NAME) model

(Maslowski et al., 2004) results. The sea ice volume from NAME is stable from 1980 to 1995 where it starts to decrease at a rate of  $-1.1 \cdot 1000 \text{ km}^3/\text{y}$  predicting a summer ice-free Arctic Ocean before 2020. The actual value at which the sea ice volume decreases is controversial. The fact that sea ice volume decreases at a much faster rate than the sea ice extent is indisputable.

The CICE model computes the ice volume for each thickness category,  $n$ , per unit area as (Hunke and Lipscomb, 2010)

$$SIV_n = SIC_n \cdot h_n. \quad (3.3)$$

where  $SIC_n$  is the sea ice concentration for the specified thickness category in percentage and  $h_n$  is its ice thickness in metres. For the SRES A1B simulations of the CCSM3, the number of thickness category is five plus open water. The average thickness of a cell is given by the sum of the sea ice volume per unit area of all the thickness categories. The sea ice volume of a cell is obtained by multiplying the average thickness,  $h_i$ , by the cell area,  $A$ ,

$$SIV = h_i \cdot A. \quad (3.4)$$

Note that the subscript  $i$  refers ice.

I have calculated the sea ice volume evolution for the six SRES A1B simulations of the CCSM3. In each simulations, the yearly maximum (winter) and minimum (summer) Arctic sea ice volume decreases similarly with approximately a  $10 \cdot 1000 \text{ km}^3$  difference as illustrated in figure 3.2. The minimum sea ice volume is more interesting since it can show when the Arctic Ocean becomes ice free. For these two reasons, only the minimum sea ice volume will be described. The yearly minimum sea ice volume starts near  $25 \cdot 1000 \text{ km}^3$  for all simulations. Between 1900 and 1950, an accumulation of sea ice volume occurs which is immediately lost. Simulation c has the most prominent one with an increase of  $7 \cdot 1000 \text{ km}^3$  from 1900 to 1920 which is lost by 1930. From 1950 to 2000, sea ice volume decreases at a mean rate of  $-0.11 \cdot 1000 \text{ km}^3/\text{y}$  with simulation a losing the most sea ice volume at  $-0.18 \cdot 1000 \text{ km}^3/\text{y}$  and simulation g.ES01 losing the least sea ice volume  $-0.08 \cdot 1000 \text{ km}^3/\text{y}$ . From 2000 to 2050, the sea ice volume decreases rapidly at a mean rate of  $-0.23 \cdot 1000 \text{ km}^3/\text{y}$  with a maximum rate

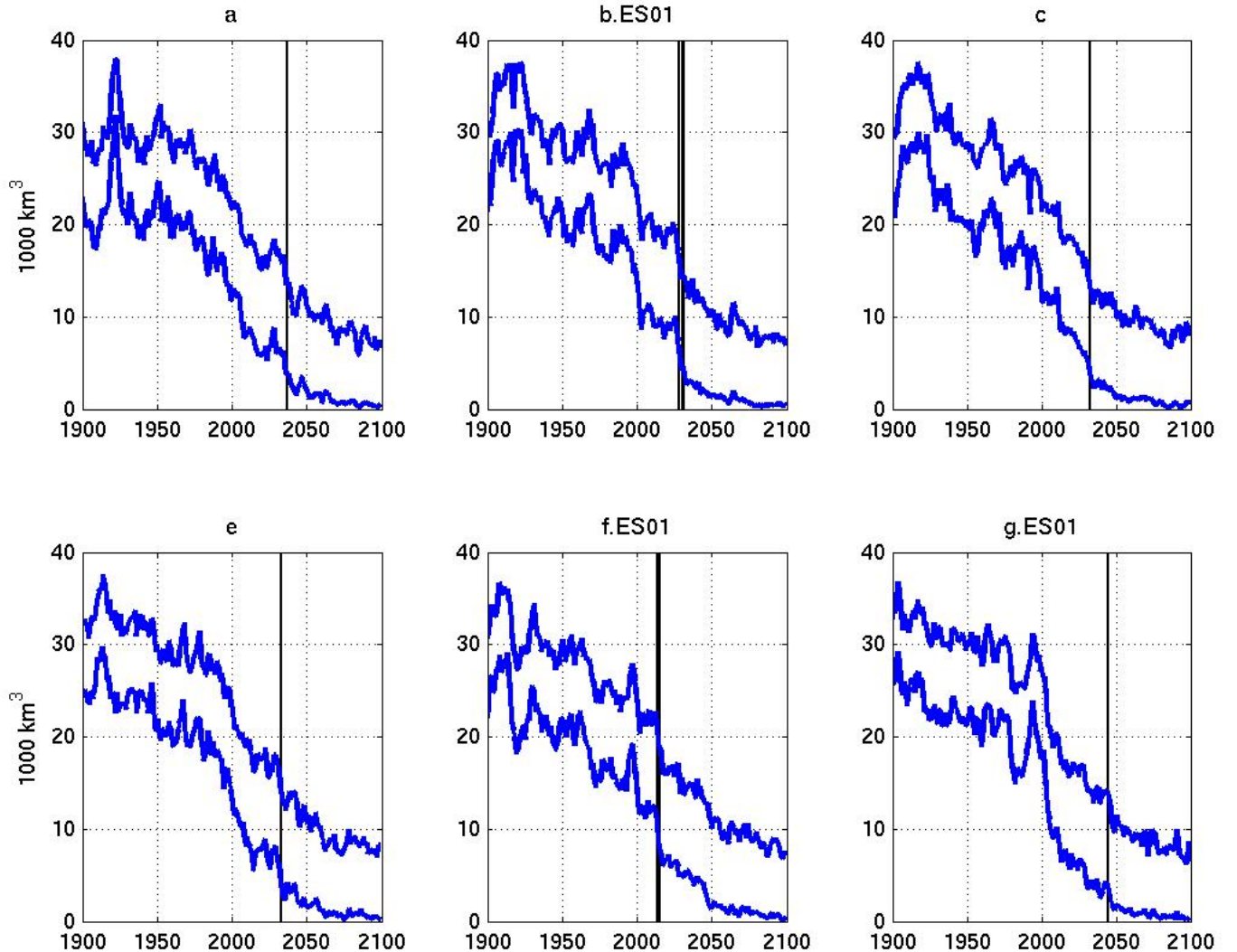


Figure 3.2: Yearly maximum and minimum Arctic sea ice volume. The vertical lines represents the years of rapid September sea ice decline.

of  $-0.25 \cdot 1000 \text{ km}^3/\text{y}$  in simulation c and g.ES01 and a minimum rate of  $-0.19 \cdot 1000 \text{ km}^3/\text{y}$  in simulation a. During the abrupt loss of September sea ice extent, the volume decreases slightly more rapidly but not in an exceptional way. It also has been described in [Holland et al. \(2006a\)](#). For the rest of the simulated time, the sea ice volume decreases slowly at a mean rate of  $-0.02 \cdot 1000 \text{ km}^3/\text{y}$  ending up close to zero by 2100.

The minimum sea ice volume decreases exponentially in function of the A1B SRES forcing, see figure 3.3. The temporal evolution of the sea ice volume does not follow a comprehensive path while it is definite as a function of the extra forcing. The half life of the sea ice volume loss is  $1 \text{ W/m}^2$ , i.e. after each forcing increase of  $1 \text{ W/m}^2$  half the sea ice is lost. Before 2000, the extra forcing is zero. Suddenly, in 2000 the extra forcing is set at  $1.03 \text{ W/m}^2$  for the A1B SRES. Half the sea ice is lost when the forcing reaches  $2.03 \text{ W/m}^2$ . At  $3.03 \text{ W/m}^2$ , only one-fourth of the initial sea ice volume is left. At  $4.03 \text{ W/m}^2$ , one-eighth is left. Etc.

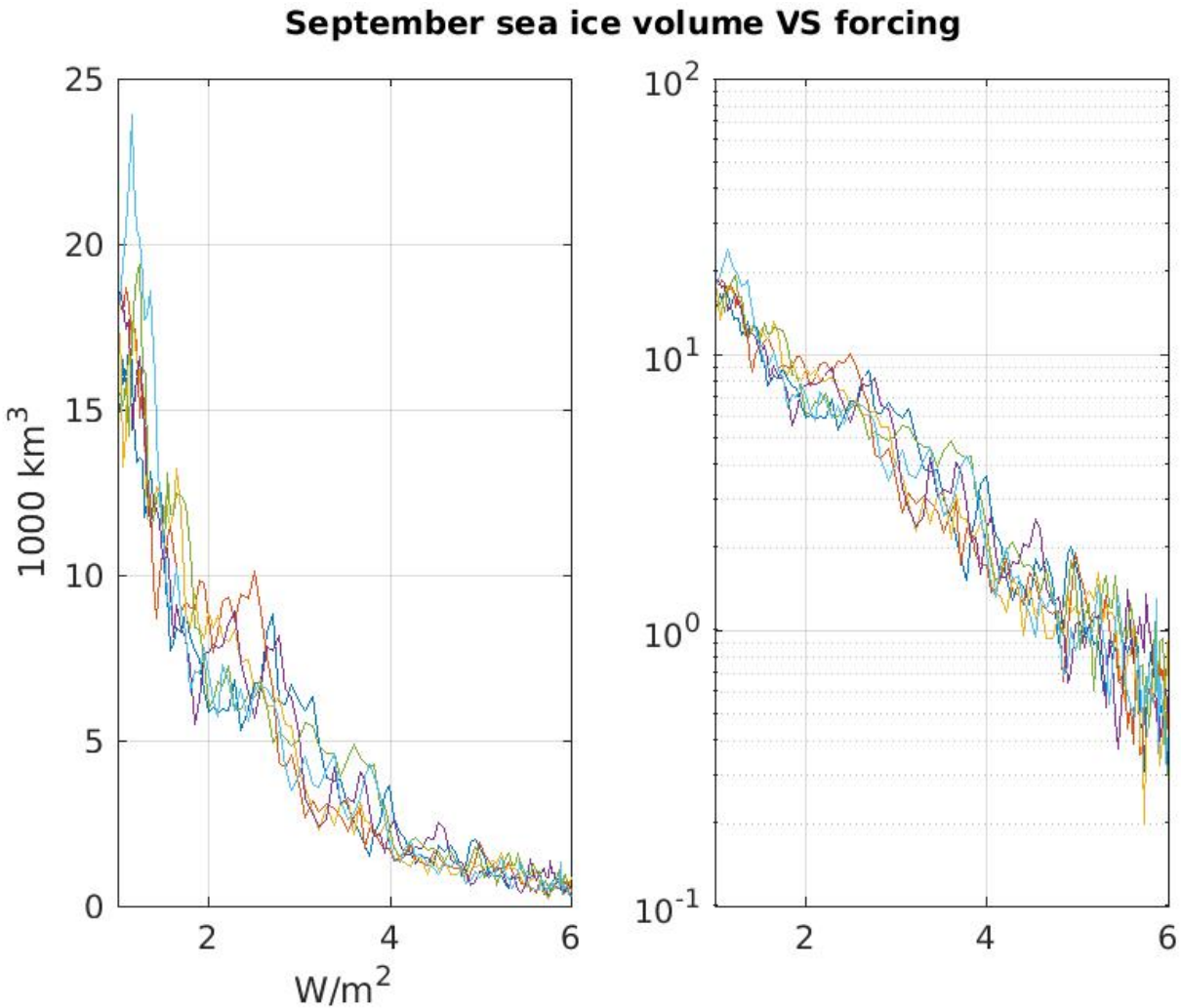


Figure 3.3: Left) Minimum sea ice volume as a function of A1B SRES forcing. Right) Semilog plot of sea ice volume in function of A1B SRES extra forcing. The linear trend of the right plot proves that the sea ice volume decreases exponentially in function of the A1B scenario forcing. Each colour represents a different simulation.

The sea ice volume evolution is determined by the forcing of the future scenario. Each forcing increment is not large enough to shock the system. If this result holds for all the other fields of the simulation, it could prove to be more effective to run models as a function of forcing instead of time. One simulation evolved through forcing offers answers for all future scenarios at once. A simulation evolved through time gives results only for a single scenario.

The September sea ice thickness spatially retreats abruptly in concurrence with the sea ice extent, see figure 3.4. Five years before the abrupt decline of September sea ice extent, the September region with sea ice thicker than one metre and the sea ice extent region are nearly the same (dotted lines of figure 3.4). In simulations a and f.ES01, the sea ice thickness

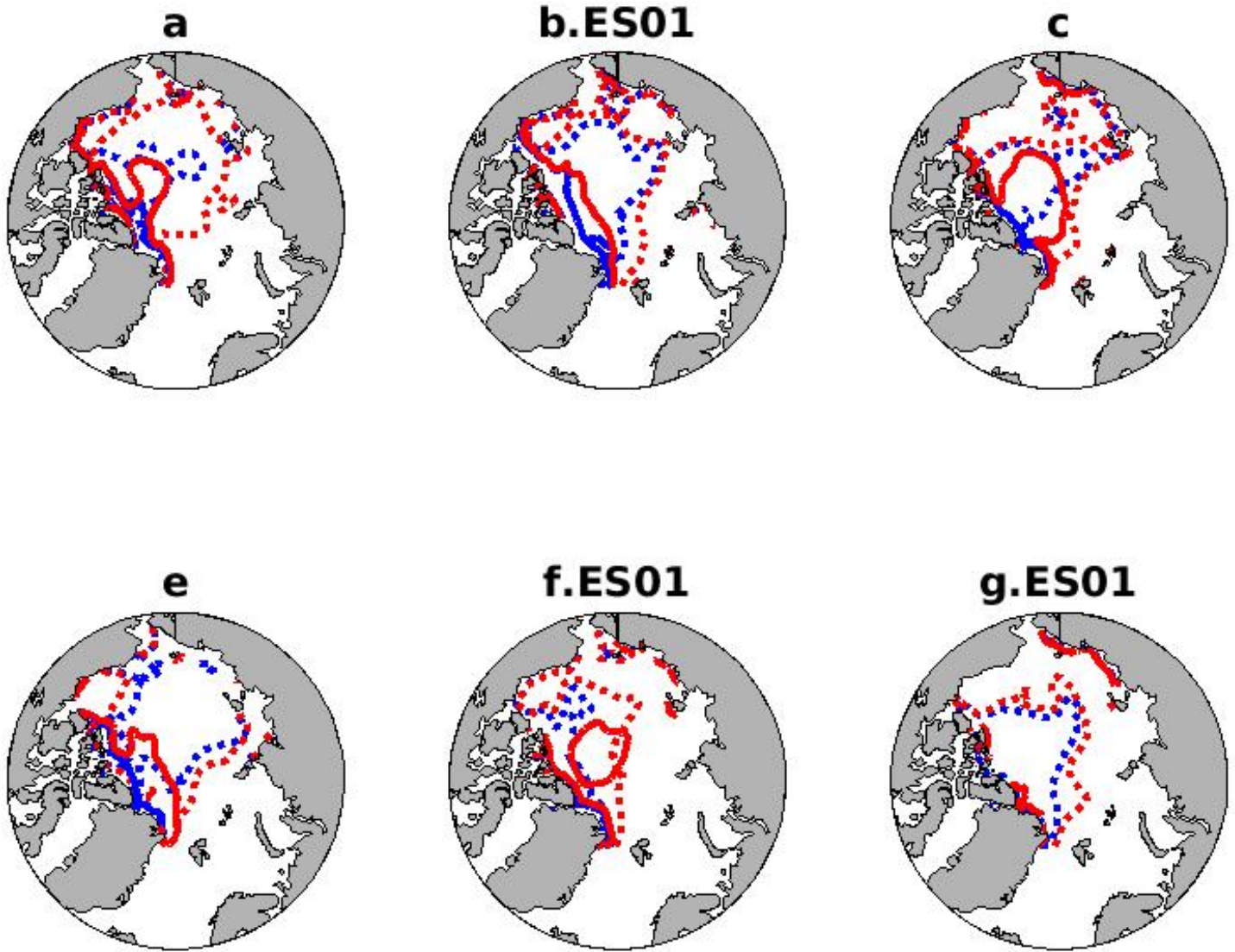


Figure 3.4: Dotted-blue) September one-metre sea ice thickness contour five years before the first rapid loss event. Solid-blue) September one-metre sea ice thickness contour five years after the last rapid loss event. Dotted-red) September sea ice extent (15% sea ice concentration contour) five years before the first rapid loss event. Solid-red) September sea ice extent (15% sea ice concentration contour) five years after the last rapid loss event.

has already started to retreat to the northern coasts of Canadian and Greenland. Simulations b.ES01, c and e show a concurrent region extending up to Russia. Simulation g.ES01 shows a concurrent region covering the centre of the Arctic Ocean but not as far as reaching Russia. Five years after the abrupt loss September sea ice extent, the region with September sea ice thicker than one metre clings to the Canadian and Greenland coasts while the September sea ice extent extends weakly to the centre of the Arctic Ocean (solid lines of figure 3.4). In simulations a, c and f.ES01, the sea ice extent does not reach beyond the centre of the Arctic Ocean. In comparison, in simulations b.ES01 and e, the sea ice extent stays close to the coasts and in simulation g.ES01, the sea ice extent clutches the coast. In each of the six

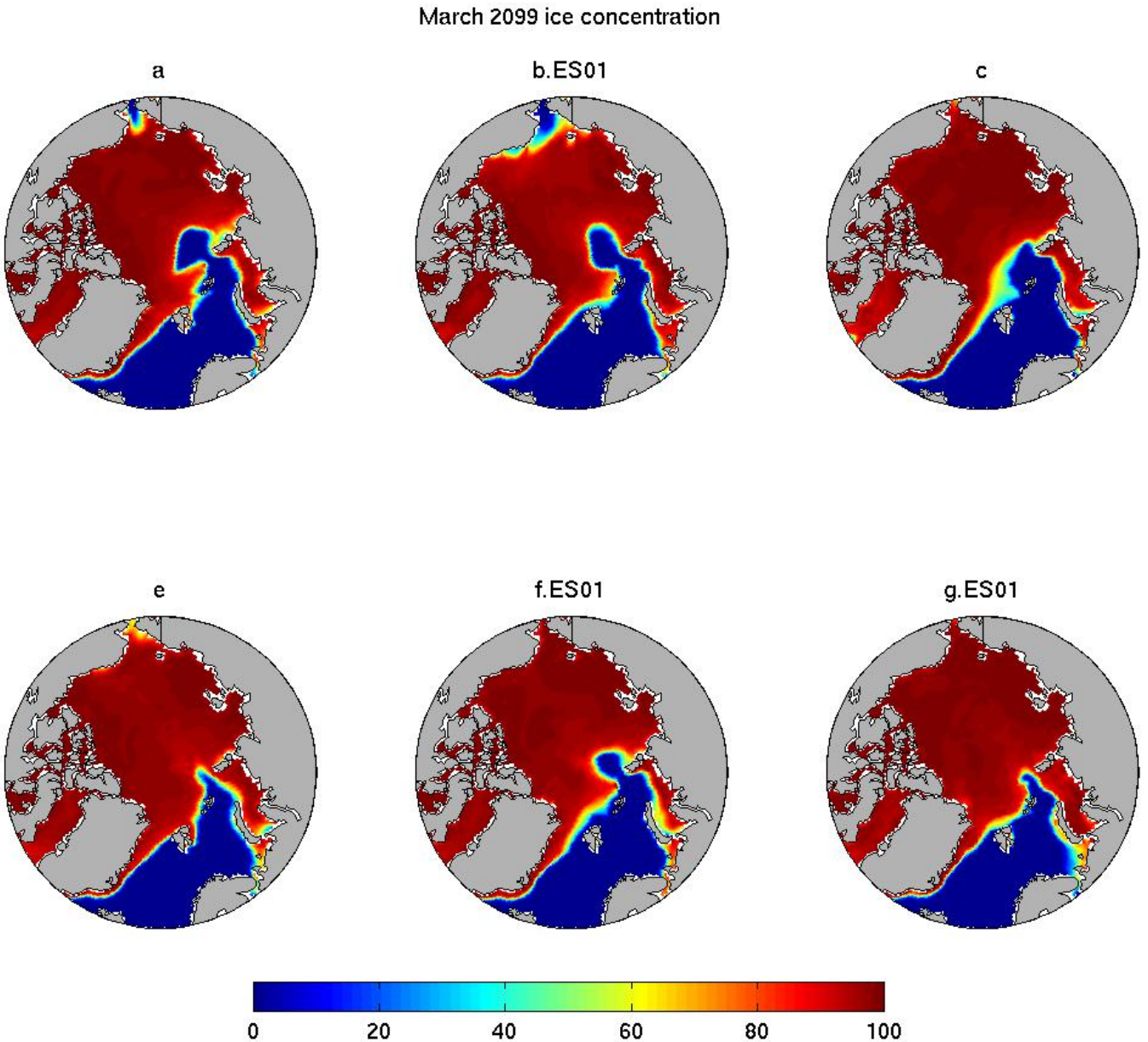


Figure 3.5: March 2099 sea ice concentration.

simulations, there is a presence of thin ice on the Russian coast of the East Siberian Sea after the abrupt loss. Simulation g.ES01 has the largest amount of sea ice on the Russian coast.

Even the winter sea ice area starts to decrease after the Arctic Ocean is ice-free during summer time. This loss is mainly located at the entrance of the Barents Sea opening (figure 3.5). There is also a retreat at the entrance of the Bering Sea in simulations a, b.ES01 and e though modest. This kind of retreat is associated to warm surface ocean fluxes through the Bering Strait melting sea ice ([Woodgate et al., 2010](#)).

On average for the month of September between 1950 and 2000, the sea ice volume of the A1B SRES simulations of the CCM3 lost 40% of the volume compared to only 8% of the sea ice extent. While the sea ice coverage decreases slowly, the sea ice volume plummets up to a

point where it cannot decrease further without strongly affecting the sea ice concentration. In the CCSM, when the sea ice thickness is in the thinnest thickness category, half of the melting reduces thickness while the other half reduces sea ice area/concentration ([Hunke and Lipscomb, 2010](#)). In these simulations, the decrease of sea ice extent under 15% of sea ice concentration is large enough to be considered an abrupt loss in the language of [Holland et al. \(2006a\)](#). Winter sea ice coverage decreases only after the summer Arctic Ocean is ice-free and is located at the gate the Barents Sea. The next section discusses the differences between the dynamic and the thermodynamic sources of sea ice volume loss.

### 3.4 Dynamic vs thermodynamic processes

[Holland et al. \(2006a\)](#) stated that the dynamic processes play little role in rapid loss of sea ice extent. The standard output of the CCSM3 includes four variables quantifying the strength of the dynamic and thermodynamic impact on SIA and SIV. Table 3.1 lists the four variables. The dynamic processes include transport out of the Arctic Ocean and are described in section 3.5 followed by the thermodynamic processes in section 3.6. The thermodynamic and dynamic impact on the sea ice area are presented first followed by their impact on the sea ice volume. The details of the dynamic and thermodynamic processes follows in sections 3.5 and 3.6 respectively.

Name	Definition	Unit
daidtd	changes of sea ice area due to dynamic processes	%/day
daidtt	changes of sea ice area due to thermodynamic processes	%/day
dvidtd	changes of sea ice volume due to dynamic processes	cm/day
dvidtt	changes of sea ice volume due to thermodynamic processes	cm/day

Table 3.1: CCSM variable names and definitions.

The thermodynamic processes increase the sea ice area by  $10 \cdot 10^6 \text{ km}^2/\text{y}$  while the dynamic processes flush out of the Arctic the same amount of sea ice area from 1900 to 2000, as can be seen from figure 3.6. The thermodynamic processes spread sea ice while the dynamic processes break and evacuate the sea ice. From 2000 to 2100 the strength of thermodynamic

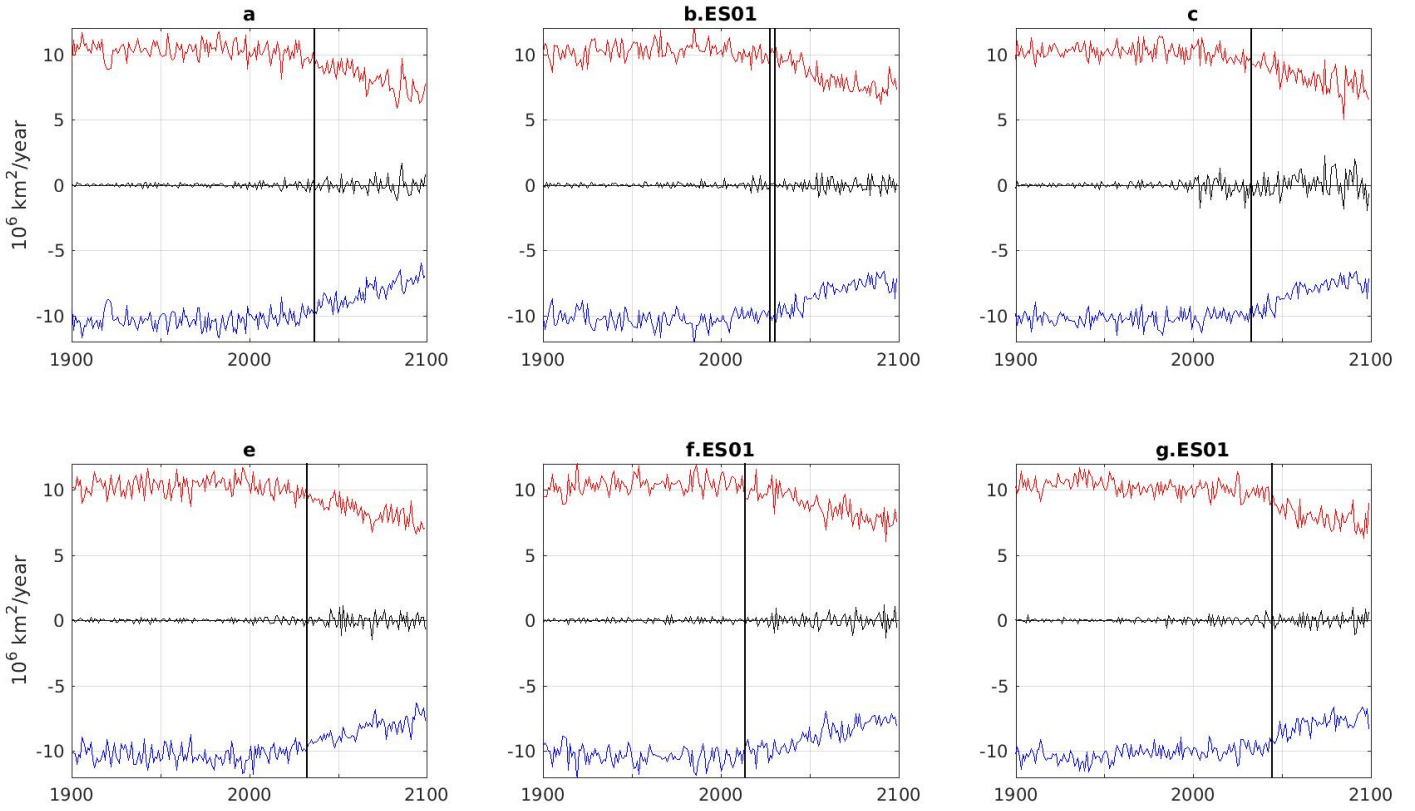


Figure 3.6: Yearly-mean thermodynamic changes (red), dynamic changes (blue) and tendency (black) of SIA. Vertical black lines represent the year of rapid September sea ice decline. These quantities are obtained from averaging over the Arctic domain presented in figure 3.1.

and dynamic processes decrease at a rate of  $0.035 \cdot 10^6 \text{ km}^2/\text{y}^2$  ending at  $7.5 \cdot 10^6 \text{ km}^2/\text{y}$ . Based on those simulations, one fourth of the creation of sea ice area will be lost by the end of the 21<sup>st</sup> century.

The thermodynamic processes affecting the sea ice volume create  $4.75 \cdot 1000 \text{ km}^3/\text{y}$  in 1900 and decreases down to  $0.9 \cdot 1000 \text{ km}^3/\text{y}$  by 2100, as can be seen from figure 3.7. It represents a loss of 80% of the sea ice volume creation. The same amount of sea ice is moved out of the Arctic Ocean by dynamic processes. The thermodynamic processes create sea ice volume while the dynamic processes evacuate it. These processes affect the sea ice area in the same way.

Over the whole Arctic Ocean domain, thermodynamic and dynamic processes impact the SIA and SIV at almost the same ratio. The thermodynamic and dynamic processes cancel each other even when averaged over the rapid loss region of September sea ice extent. It contradicts Holland et al. (2006a) who stated that dynamic processes are insignificant compared to thermodynamic processes. Nothing particular happens at the time of the rapid sea ice decline events. The values for the thermodynamic and dynamic processes concord

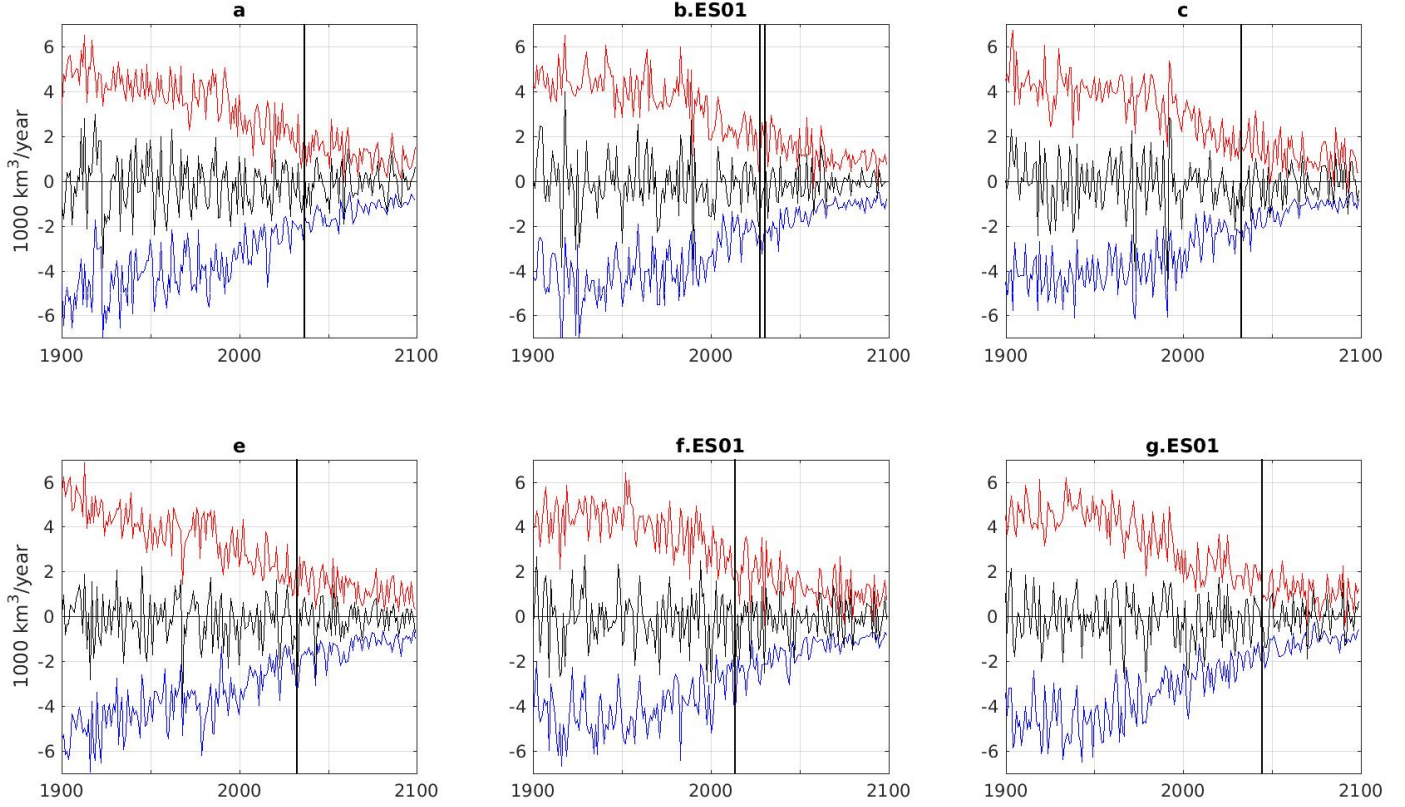


Figure 3.7: Yearly-mean thermodynamic changes (red), dynamic changes (blue) and total (black) of SIV. These quantities are obtained from averaging over the Arctic domain presented in figure 3.1. Vertical black lines represent the years of rapid September sea ice decline.

with Serreze et al. (2007) and Holland et al. (2010).

### 3.5 Transport out of the Arctic Ocean

The sea ice volume transport (SIVT) at the gates of the Arctic Ocean (figure 3.1) is calculated as the integration over the gate of the the sea-ice velocity perpendicular to the gate ( $u_{\perp}$ ) and the sea-ice thickness ( $h$ ),

$$SIVT = \int_{gate} u_{\perp} \cdot h dx \rightarrow \sum_{gate} u_{\perp} \cdot h \cdot \Delta x \quad (3.5)$$

It is not a standard output of the CCSM3. The best way to approximate this quantity using the standard output is to compute the monthly mean perpendicular velocity multiplied by the monthly mean sea ice thickness. The instantaneous quantities are linked to the averaged quantities though the next equation,

$$\overline{u_{\perp}^I \cdot h^I} = \overline{(u_{\perp} + u'_{\perp}) \cdot (h + h')} = u_{\perp} \cdot h + \overline{u'_{\perp} \cdot h'}. \quad (3.6)$$

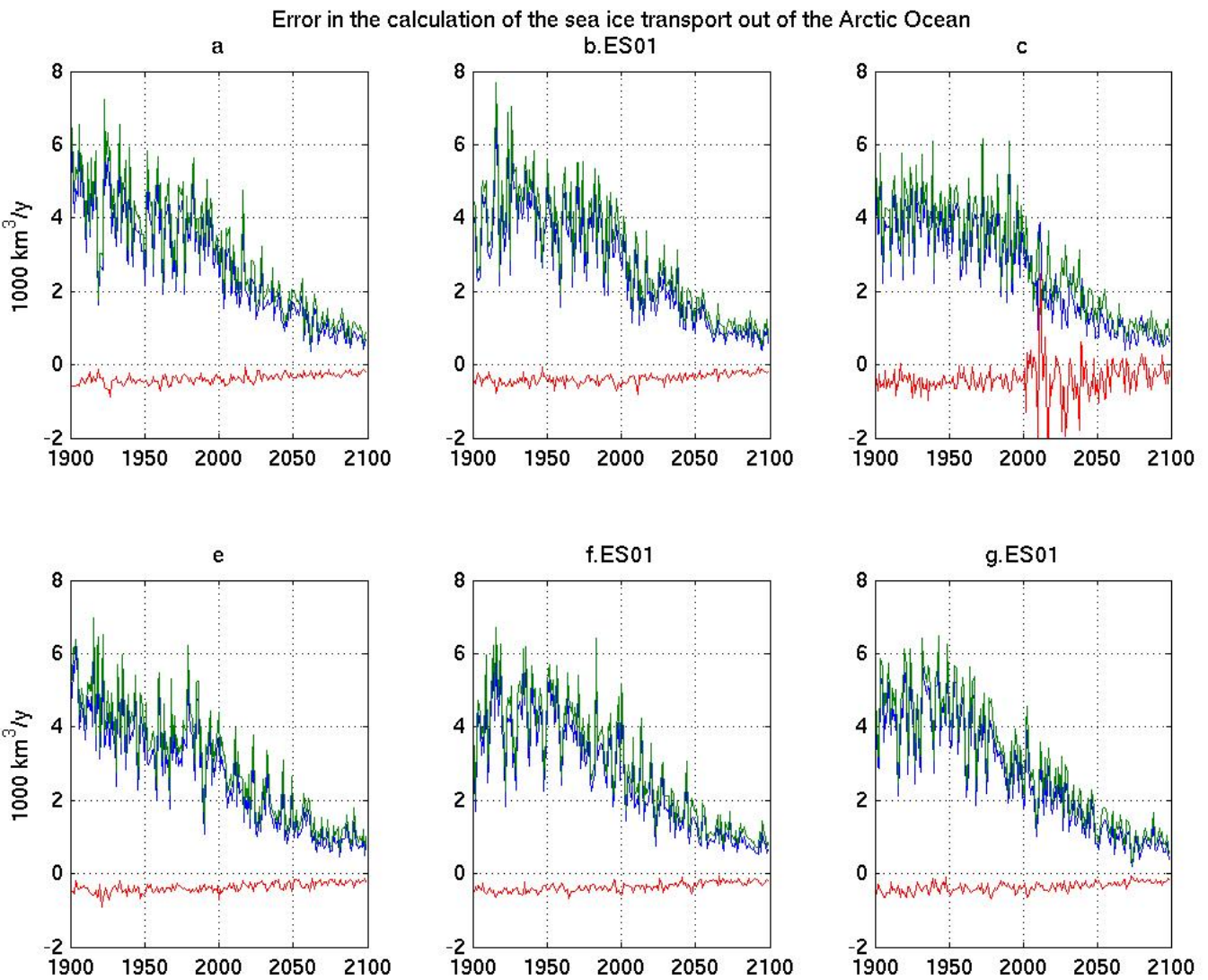


Figure 3.8: Sea ice transport out of the Arctic Ocean (blue), changes in sea ice volume caused by dynamic processes (green) and the difference between the two (red). The data represents yearly averages.

The over bar denotes monthly averaging and the high index  $I$  means instantaneous. They are both equal up to  $\overline{u'_\perp \cdot h'}$ . Based on observations, Arfeuille et al. (2000) noticed that this term is negligible for the Fram Strait.

It is possible to assess the magnitude of the error of the proposed calculation using the results from the last section. The total dynamic changes of sea ice volume over the Arctic Ocean should be equal to the sum of the sea ice volume transport through all the gates of the Arctic Ocean. The error between the SIVT and the dynamic changes in sea ice volume is acceptable (figure 3.8) except for simulation c over the 21<sup>st</sup> century. Excluding simulation c, the error decreases in time from  $0.5 \cdot 1000 \text{ km}^3/\text{y}$  down to  $0.2 \cdot 1000 \text{ km}^3/\text{y}$  with the dynamic changes in volume always being higher than the calculated transport out of the Arctic. At the beginning of the simulations the error represents 12% while it represents 30% by 2100. The presented calculation of the sea ice volume transport is not exact but the similarities

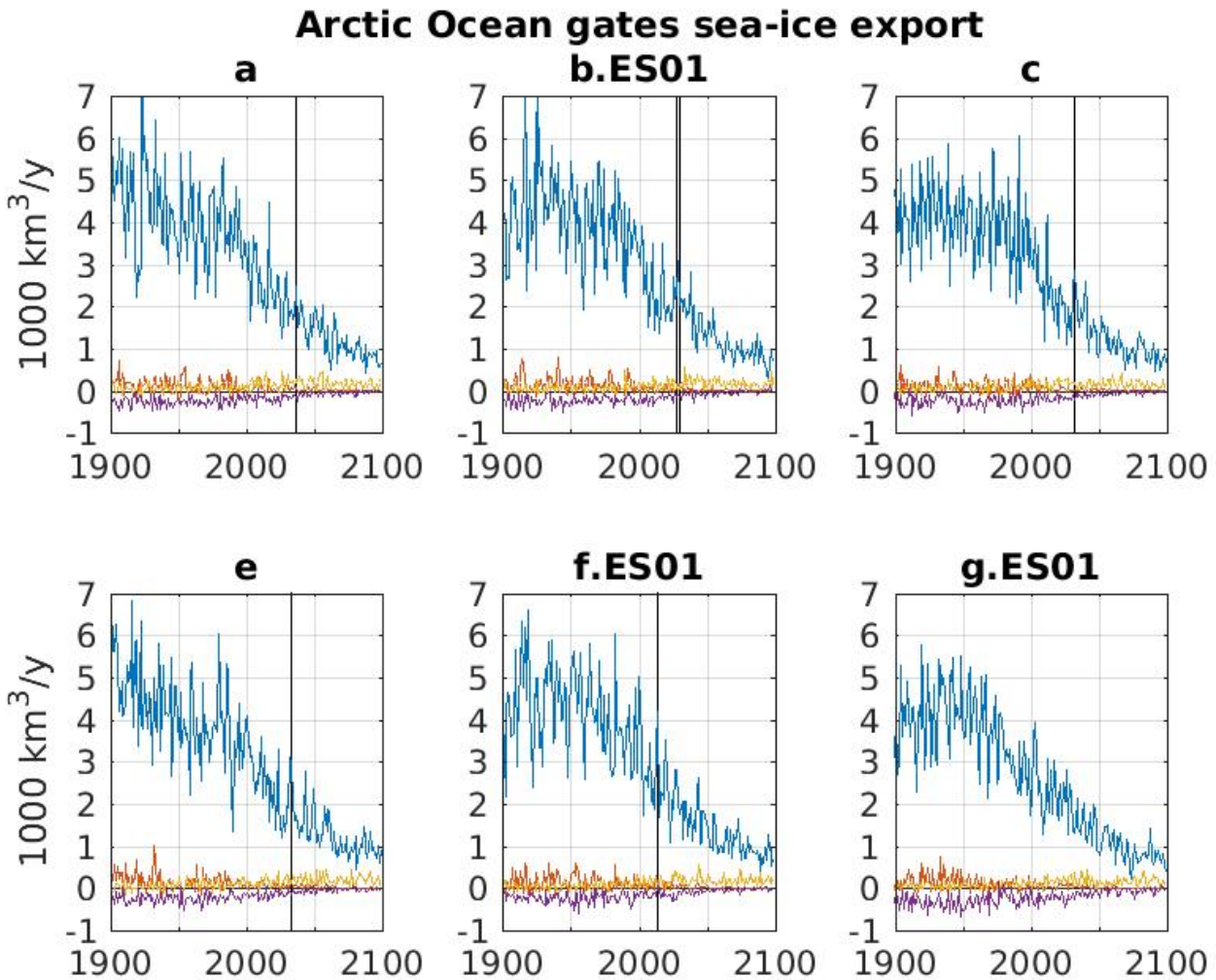


Figure 3.9: Yearly-mean Fram (blue), Barents (red), CAA (yellow) and Bering (purple) ice transport out of the Arctic Ocean.

between the different variables for the SIVT and the results from [Arfeuille et al. \(2000\)](#) point to an irrelevant error.

The Arctic sea-ice export through the Fram Strait is dominating all the other gates (see figure 3.9);  $4 \cdot 1000 \text{ km}^3/\text{y}$  for the Fram Strait,  $0.2 \cdot 1000 \text{ km}^3/\text{y}$  for the Barents sea opening,  $0.04 \cdot 1000 \text{ km}^3/\text{y}$  for the CAA,  $-0.2 \cdot 1000 \text{ km}^3$  for the Bering Strait for the 1900-1910. The export through the Fram Strait decreases linearly, between  $-0.007 \cdot 1000 \text{ km}^3/\text{y}^2$  and  $-0.02 \cdot 1000 \text{ km}^3/\text{y}^2$  through the runs, until the A1B SRES forcing starts year 2000 where it decreases exponentially until 2080 where it stabilizes at  $0.7 \cdot 1000 \text{ km}^3$ .

### 3.6 Thermodynamic

Thermodynamic processes include sea ice surface melt (section 3.6.1), bottom melt and growth (section 3.6.2), lateral melt (section 3.6.3), and frazil sea ice formation (section 3.6.4). Bottom melt and basal growth are analyzed together since they share the same equations.

### 3.6.1 Surface melt

This section describes the evolution of the surface melt and the surface fluxes. When the surface heat fluxes surpass the heat conducted through the ice, the extra energy is used for surface melt. It is not possible to conduct more energy than received and grow sea ice at the surface. The surface melt is calculated as:

$$\Delta h = (F_0 - F_{ct})/q \quad (3.7)$$

where  $F_0$  is the sum of all the surface fluxes,  $F_{ct}$  is the heat conduction at the top of the ice, and  $q$ , which is negative, is the enthalpy of surface ice ([Hunke and Lipscomb, 2010](#)). The

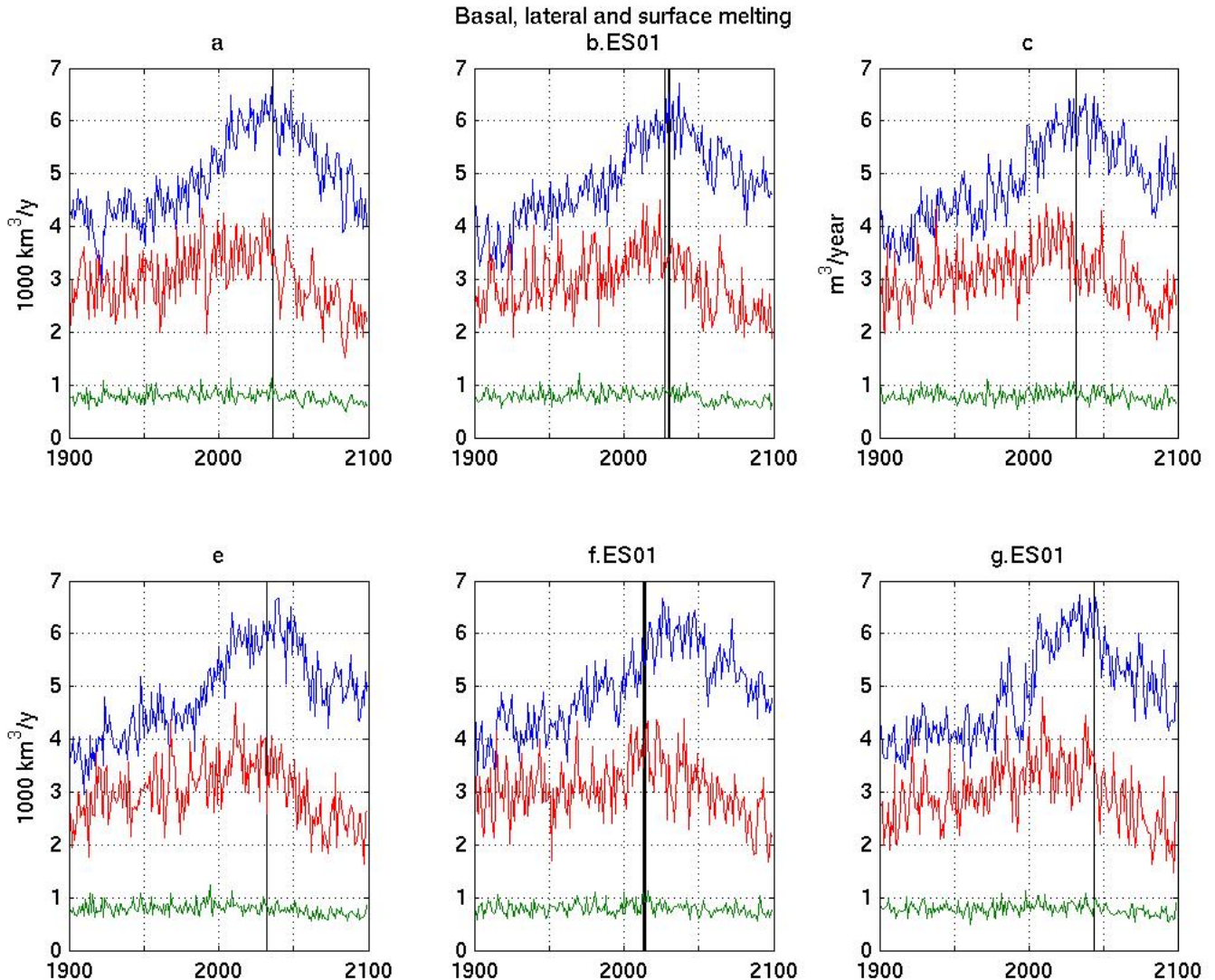


Figure 3.10: Yearly-mean basal (blue), lateral (green) and surface (red) melt integrated over the Arctic Ocean. Vertical black lines represent the years of rapid September sea ice extent decline.

surface melt increases steadily from  $2.7 \cdot 1000 \text{ km}^3/\text{y}$  in the 1900-1910 up to  $4.5 \cdot 1000 \text{ km}^3/\text{y}$  during the rapid loss events, see figure 3.10. After the rapid loss events, the surface melt decreases ending at  $2.4 \cdot 1000 \text{ km}^3/\text{y}$ . The decrease in surface melt is surprising since surface fluxes strictly increase through the simulation enhancing surface melt. But, after the rapid loss of September sea ice extent, there is far less sea ice to melt. This drastic loss of sea ice has a more important impact on the total surface energy transfer than the increase in surface fluxes. It is similar to stretching an elastic. While the stretch increases, the elastic thins up until it breaks. It then relaxes to a new broken state. The Arctic sea ice is thinned by the surface fluxes until it reaches a threshold where the sea ice extent becomes seriously affected by the surface fluxes causing the rapid sea ice declines. The remaining part of this section explores the magnitude of the different surface processes.

The surface conductive heat flux,  $F_{ct}$ , is calculated as

$$F_{ct} = K_h \cdot (T_{surf} - T_q), \quad (3.8)$$

where  $K_h$  is a turbulent conduction coefficient,  $T_{surf}$  is the temperature at the surface of the ice and  $T_q$  is the sea ice temperature calculated from its enthalpy. Unfortunately, the standard output of the CCSM does not include the turbulent conduction coefficient nor the surface atmospheric temperature nor the sea ice temperature or its enthalpy.

The surface fluxes,  $F_0$ , include sensible heat flux,  $F_s$ , latent heat flux,  $F_l$ , emitted and absorbed long wave radiation,  $F_{lw}$ , and absorbed shortwave radiation,  $F_{sw}$ . The sensible heat flux is given by the temperature difference between the atmosphere and the sea ice,

$$F_s = C_s(\Theta_a - T_{surf}), \quad (3.9)$$

where  $C_s$  is a nonlinear turbulent heat transfer coefficient and  $\Theta_a$  is the atmosphere surface potential temperature. The latent heat flux comes from a difference in humidity between the atmosphere and the sea ice. A dry surface atmosphere will force sea ice to sublimate

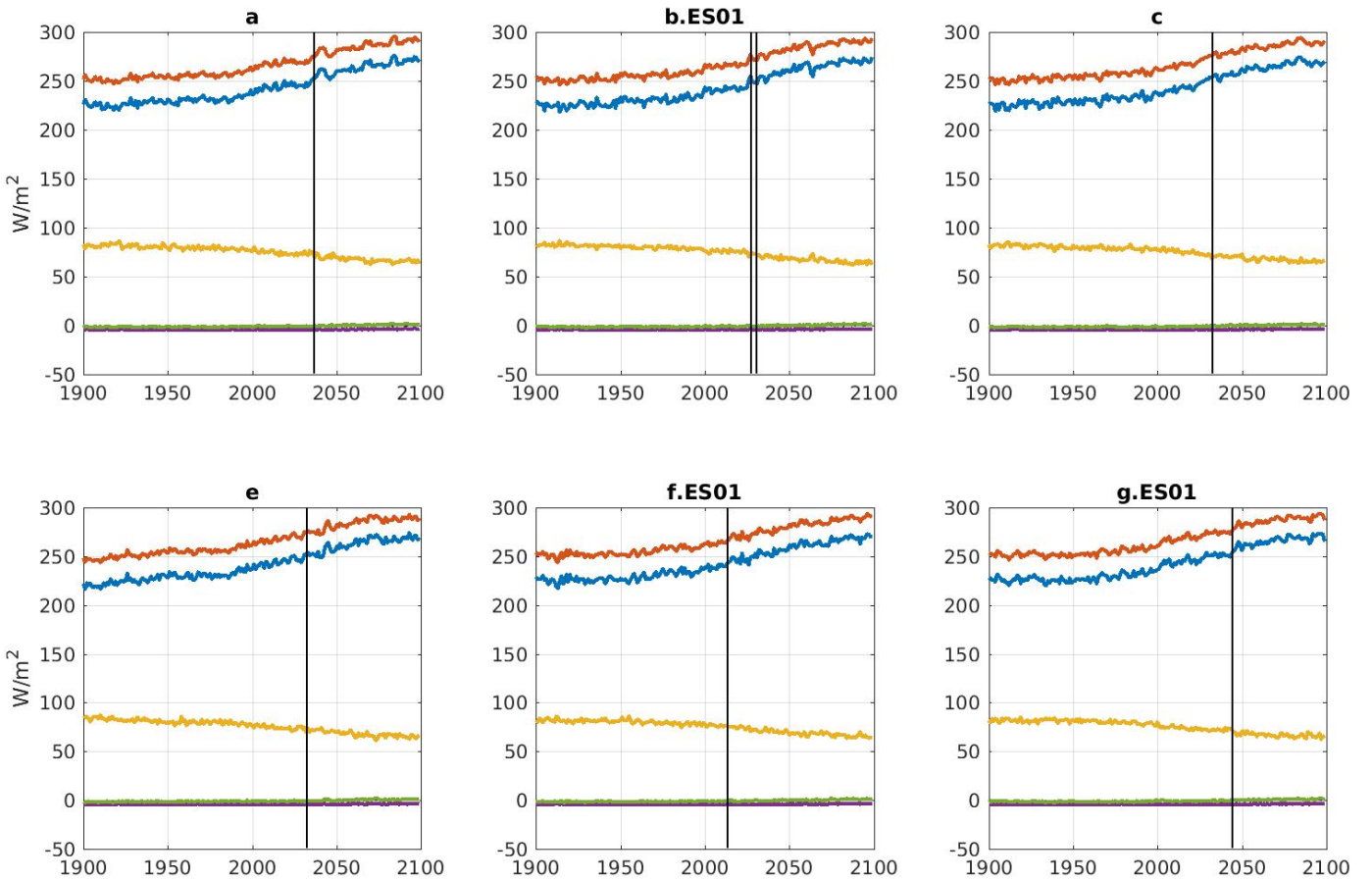


Figure 3.11: Yearly-mean sea ice surface fluxes averaged over the Arctic Ocean: red) downwelling long wave, blue) emitted longwave, yellow) shortwave radiation reaching sea ice, purple) latent, green) sensible. Vertical lines depict the years of rapid September sea ice extent decline.

absorbing the latent energy of sublimation from the sea ice. It is calculated as

$$F_l = C_l(Q_a - Q_s), \quad (3.10)$$

where  $C_l$  is a nonlinear turbulent heat transfer coefficient,  $Q_a$  is the atmosphere specific humidity at the surface and  $Q_s = \frac{q_1}{\rho_a} \exp\left(\frac{-q_2}{T_{sf}}\right)$  is the surface humidity of sea ice with  $q_1 = 1.16378 \text{ kg/m}^3$ ,  $q_2 = 5897.8 \text{ K}$  and  $\rho_a$  is the surface air density. Latent and sensible heat fluxes seem inconsequential compared to radiative fluxes being under  $5 \text{ W/m}^2$  of magnitude, see figure 3.11. They are comparable to the net longwave radiation or absorbed shortwave radiation though.

The emitted longwave radiation,  $F_{lw\,e}$ , is given by the Stefan-Boltzmann law,

$$F_{lw\,e} = \epsilon F_{lw\,a} - \epsilon \sigma_{SB} T_{sf}^4, \quad (3.11)$$

where  $\epsilon$  is the emissivity of sea ice,  $F_{lw\,a}$  is the longwave atmospheric radiation reaching sea ice and  $\sigma_{SB}$  is the Stefan-Boltzmann constant. The long wave radiation reaching sea ice starts at  $225\text{ W/m}^2$  between 1900 and 1910. It then increases slowly at a pace of  $0.1\text{ W/m}^2/\text{y}$  until 2000 where it increases at  $0.4\text{ W/m}^2/\text{y}$  until 2080. It then stabilizes at  $269\text{ W/m}^2$ . The SRES A1B predicts an augmentation of green house gases which is included in the CCSM3. Green house gases take a part of the solar radiation and reemit it as long wave radiation. They also absorb some of the longwave radiation that would exit our atmosphere and reemit it downward as longwave radiation. An increase in green house gases causes an increase in downward longwave radiation. The emitted long wave radiation starts at  $250\text{ W/m}^2$  increasing at  $0.1\text{ W/m}^2/\text{y}$  until 2000 where it increases at  $0.3\text{ W/m}^2/\text{y}$  until 2080 where it stabilizes at  $290\text{ W/m}^2$ . The increase is due to an increased sea ice surface temperature. The resulting long wave radiation is stable over the 19<sup>th</sup> century at  $-25\text{ W/m}^2$  meaning there is more energy emitted than received. From 2000 to 2080, the magnitude of the difference between long wave absorption and emission decreases at a rate of  $0.06\text{ W/m}^2/\text{y}$  stabilizing after 2080 at  $-20\text{ W/m}^2$ .

When the solar radiation reaches the sea ice, most of it is reflected at the surface. The remaining solar radiation is partly absorbed by the sea ice, a part of it is conducted through the sea ice to the ocean. The amount of reflected radiation is given by the albedo or reflectivity,  $\alpha$  of sea ice. The fraction of radiation conducted through sea ice is given by the variable  $i_0$ . The absorbed shortwave radiation is given by

$$F_{sw\,abs} = (1 - \alpha)(1 - i_0)F_{sw}, \quad (3.12)$$

where  $F_{sw}$  is the atmospheric shortwave radiation reaching sea ice. The shortwave radiation reaching sea ice starts at  $82\text{ W/m}^2$  in 1900 and end at  $65\text{ W/m}^2$  by 2100. It constantly loses magnitude to the green house gases transforming it in long wave radiation. The absorbed

shortwave radiation by sea ice starts at  $26\text{ W/m}^2$  and increases up to  $28\text{ W/m}^2$  by the time of the rapid loss. It then decreases to  $26.7\text{ W/m}^2$  by the end of the simulations. Since the shortwave radiation reaching sea ice decreases, it may seem surprising to observe an increasing absorbed shortwave but it can be explained. The level of absorption is managed by the albedo and the amount of radiation going through the sea ice to the ocean. The albedo of the Arctic sea ice has a value of 0.7 in 1900 and decreases slowly through the 20<sup>th</sup> century. Over the 21<sup>st</sup> century, the average Arctic albedo decreases rapidly reaching .55 by 2100. The amount of radiative energy going through sea ice starts at  $1\text{ W/m}^2$  in 1900 up to  $2.4\text{ W/m}^2$  by 2100. It increases slowly between 1900 and 2000 and increases rapidly between 2000 and 2100. This increase is the result of the thinning of sea ice making it easier for shortwave radiation to go through sea ice. Even with an increased amount of energy going through the sea ice, the lowered albedo allows for more radiation to be absorbed even with a less vigorous shortwave radiation reaching sea ice.

The total sea ice surface heat flux starts at  $-5\text{ W/m}^2$  in 1900 and increases linearly at a rate of  $0.02\text{ W/m}^2/\text{y}$  for 100 years reaching  $-3\text{ W/m}^2$  in 2000. It then increases linearly at  $0.065\text{ W/m}^2/\text{y}$  between 2000 and 2100 ending at  $3.5\text{ W/m}^2$ . During the 20<sup>th</sup> century, the longwave and shortwave radiation cancel each other leaving only the latent and sensible fluxes,  $-4\text{ W/m}^2$  and  $-1\text{ W/m}^2$  respectively. During the 21<sup>st</sup> century, the shortwave radiation surpasses the longwave radiation and adds to the latent and sensible heat fluxes. Averaged yearly, the surface fluxes have a cooling effect on the sea ice before the rapid declines and a warming effect after.

### 3.6.2 Basal melt and growth

Bottom melting and basal growth are driven by the ocean. They are calculated as:

$$\Delta h = \frac{F_{cb} - F_{bot}}{q}, \quad (3.13)$$

where  $F_{cb}$  is the heat conduction at the bottom of the ice and  $F_{bot}$  is the heat flux from the ocean to the ice. If the ocean transfers more heat than what the sea ice can conduct, the extra energy melts sea ice. Basal growth occurs when the sea ice is cooled by the cold

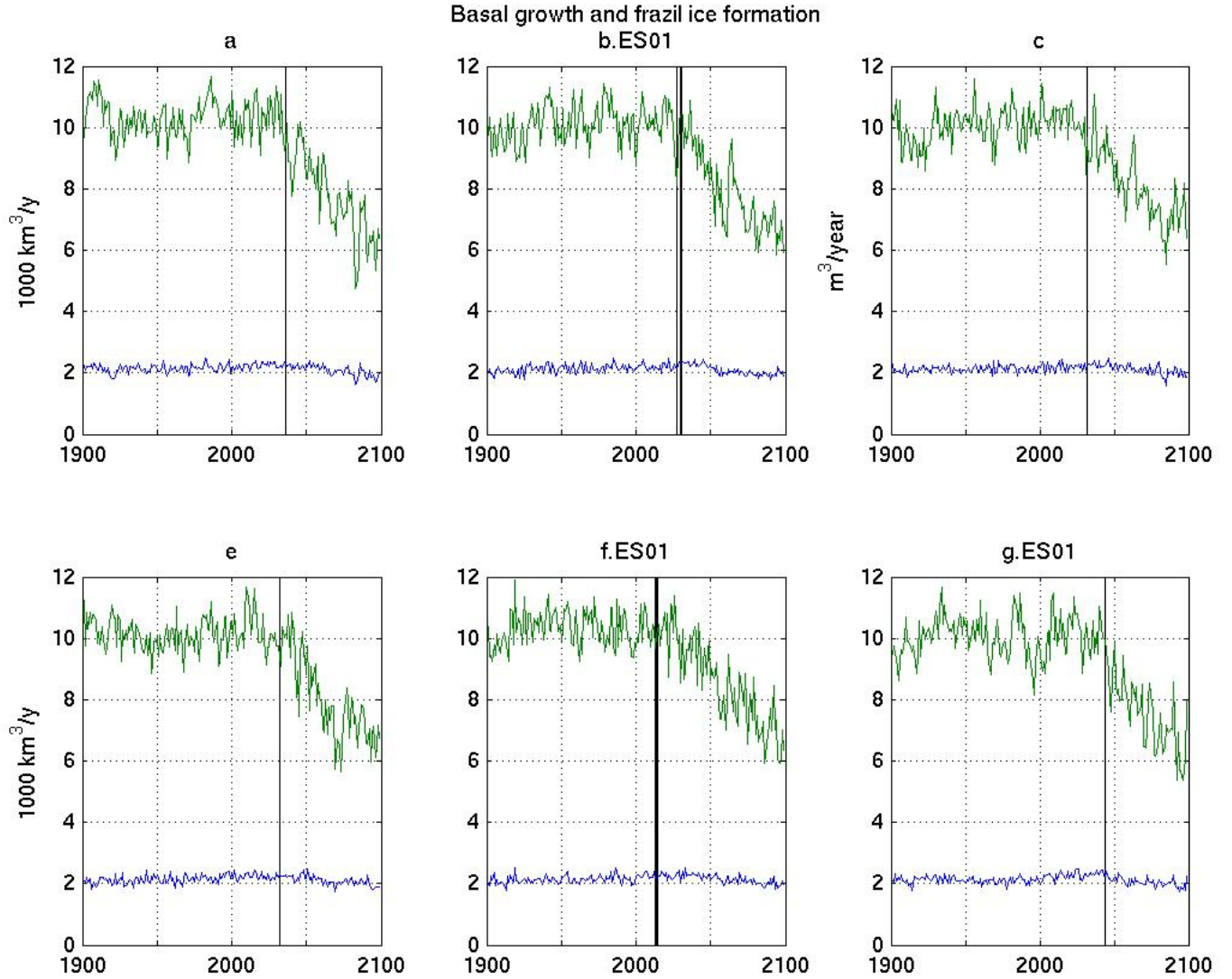


Figure 3.12: Yearly-mean frazil ice formation (blue) and basal ice growth (green) integrated over the Arctic Ocean. Vertical black lines represent the years of rapid September sea ice extent decline.

atmosphere sucking energy from the ocean through conduction. When the surface ocean reaches the freezing temperature of  $-1.8^{\circ}\text{C}$  for saline water in the CCSM, the latent heat of solidification is conducted upwards and sea ice is formed. The basal melt increases nonlinearly from  $3.9 \cdot 1000 \text{ km}^3/\text{y}$  during the 1900-1910 up to  $6.7 \cdot 1000 \text{ km}^3/\text{y}$  during the rapid loss events followed by a decrease ending at  $4.8 \cdot 1000 \text{ km}^3/\text{y}$ , see figure 3.10. During the whole simulation, bottom fluxes strictly increase, thus enhancing basal melt. After the rapid loss of September sea ice extent, the basal melt decreases because there is far less sea ice to melt. The basal ice growth is stable at  $10.1 \cdot 1000 \text{ km}^3/\text{y}$  until the rapid sea ice decline events and decreases briskly at  $-0.045 \cdot 1000 \text{ km}^3/\text{y}^2$  until 2080 where it stabilizes at  $6.8 \cdot 1000 \text{ km}^3/\text{y}$ , see figure 3.12. The loss of sea ice does not come from a lack of sea ice formation since it is mostly

stable. The rapid losses of sea ice are caused by increased melt. The components of the basal fluxes are studied in the rest of this section.

The heat flux from the ocean to the sea ice is calculated as:

$$F_{bot} = -\rho_w \cdot c_w \cdot c_h \cdot u_* \cdot (T_w - T_{fr}), \quad (3.14)$$

where  $\rho_w$  is the water density,  $c_w$  is the water heat capacity,  $c_h$  is the heat exchange coefficient,  $u_* = \sqrt{|\tau_w|/\rho_w}$  is the friction velocity,  $|\tau_w|$  is the norm of the shear stress given by  $\mu_w \sqrt{\frac{\partial u^2}{\partial y} + \frac{\partial v^2}{\partial x}}$  with  $\mu_w$  being the ocean dynamical viscosity,  $T_w$  is the water temperature,  $T_{fr}$  is the freezing temperature of the ocean set at  $-1.8^\circ C$  in the CCSM. The heat flux from the ocean to the sea ice starts at  $-34 W/m^2$  and increases in strength at a pace of  $0.09 W/m^2/y$  reaching  $-43 W/m^2$  by the year 2000, see figure 3.13. The negative sign of the flux represents a loss of heat from the ocean to the ice. From 2000 to 2080, the heat exchange between the ocean and the sea ice increases rapidly at a rate of  $0.9 W/m^2/y$  stabilizing at  $117 W/m^2$  by 2080.

The turbulent heat flux between the sea ice and the ocean is driven by the friction velocity and the sea surface temperature. The sea surface temperature increases exponentially and the rapid sea ice declines happen at  $-0.9^\circ C$  (figure 3.14). Over the full simulation, the maximum sea surface temperature increases is of  $8^\circ C$  and is located over the Barents Sea. Disappointingly, the sea surface temperature data of simulation a is missing. The friction velocity increases until the rapid sea ice decline where it starts decreasing. Averaged over the simulations, the friction velocity starts at  $0.129 m/s$  by the year 1900 and increases up to  $0.131 m/s$  during the years of abrupt ice loss and then decreases down to  $0.130 m/s$ . The variability of the friction velocity is on average  $0.019 m/s$  and peaking at 0.04. It is more significant than its trend which culminates at  $0.012 m/s$  causing an obfuscated signal. At the moment of the rapid sea ice decline, the friction velocity is not at a maximum or at an unusually high value. Therefore, the friction velocity is not impactful in terms of rapid sea ice decline. Unfortunately, the standard output of the CCSM does not include the bottom conduction or its components.

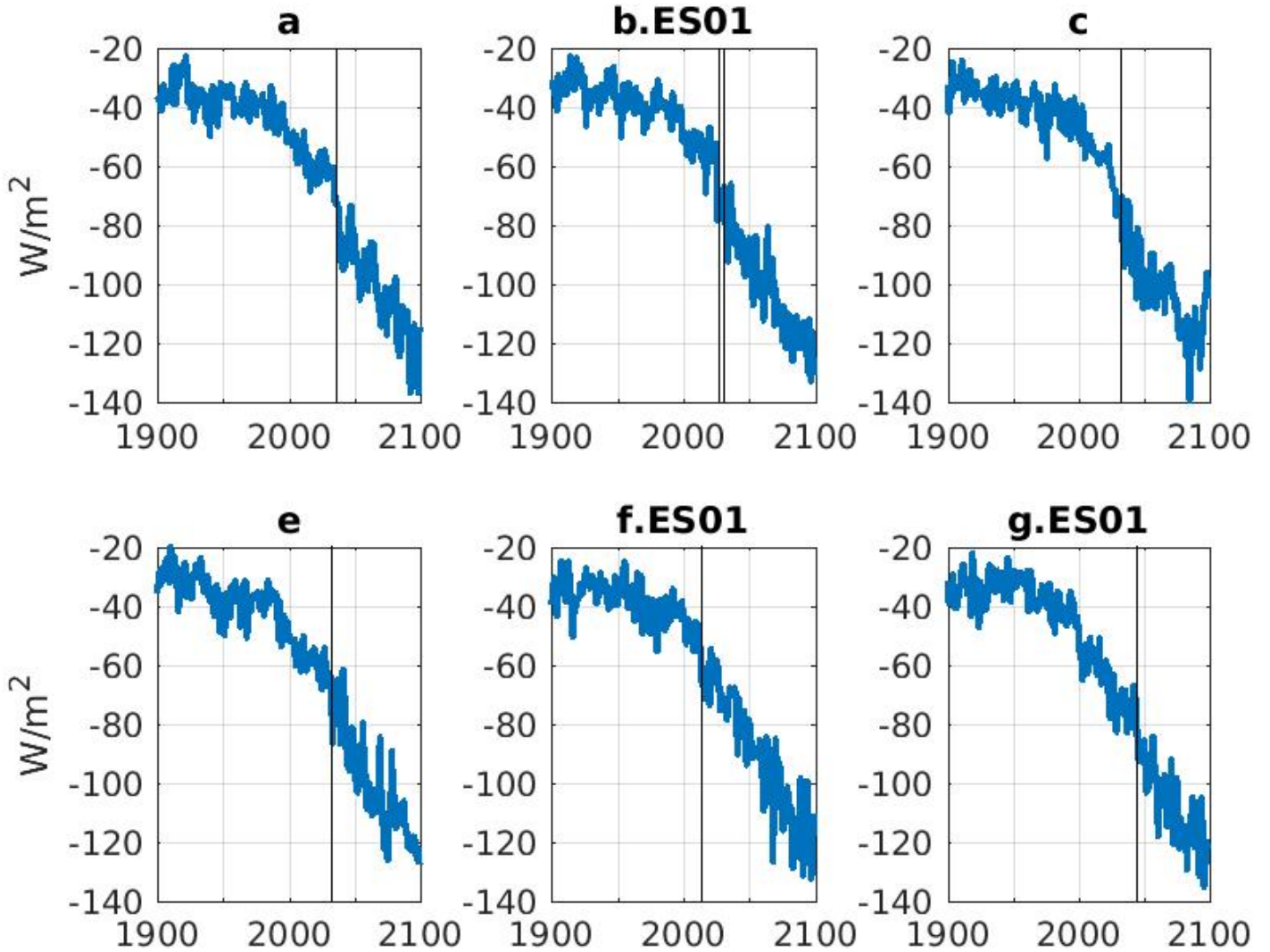


Figure 3.13: Yearly-mean turbulent heat flux between the sea ice and ocean averaged over the Arctic Ocean. A negative value represents a loss of heat from the ocean to the sea ice. Vertical black lines represent the years of rapid September sea ice extent decline.

### 3.6.3 Lateral melt

Lateral melting is calculated as

$$F_{side} = r_{side} \cdot E_{tot}, \quad (3.15)$$

$$r_{side} = \frac{m_1 \cdot (T_w - T_{bot})^{m_2} \cdot \pi}{\alpha \cdot f_D}, \quad (3.16)$$

where  $E_{tot}$  is the total energy available to melt ice and snow,  $m_1 = 1.6 \cdot 10^{-6}$  and  $m_2 = 1.36$  are coming from [Maykut and Perovich \(1987\)](#),  $\alpha = 0.66$  from [Steele \(1992\)](#),  $f_D$  is the flow diametre set at 300 m. The lateral melting decreases slightly during the full duration of the

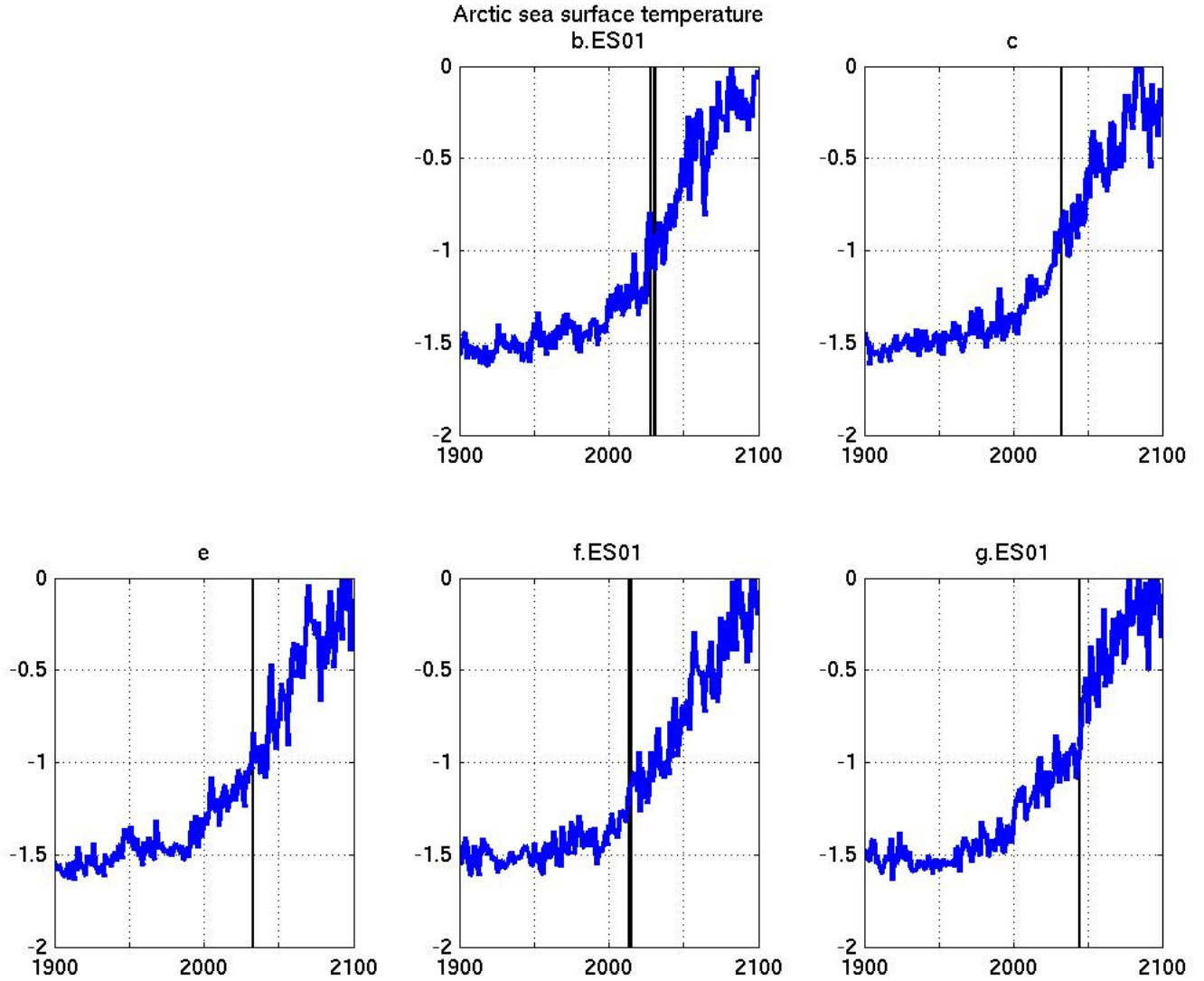


Figure 3.14: Yearly-mean sea surface temperature averaged over the Arctic Ocean in  $^{\circ}\text{C}$ . Vertical black lines represent the years of rapid September sea ice extent decline.

simulation at  $-0.4 \cdot \text{km}^3/\text{y}^2$  starting at  $0.8 \cdot 1000 \text{ km}^3/\text{y}$  in the 1900-1910.

Lateral melt is less important than surface and bottom melt and is fairly constant through the simulations. Thereby, it could not have caused the rapid sea ice declines and the analysis of this process is not pursued.

### 3.6.4 Frazil

Frazil ice develops as supercooled ocean droplets form small crystals of ice in the mixed layer and, due to their buoyancy, reach the surface of the ocean. The production rate of frazil ice

is calculated as:

$$G_{frazil} = \frac{(T_{fr} - T_w) \cdot c_w \cdot \rho_w \cdot h_{mix}}{q_0} \quad (3.17)$$

where  $h_{mix}$  is the thickness of the ocean mixed layer,  $q_0$  is the enthalpy of newly formed ice. Frazil is always less important than basal ice growth. Frazil ice formation is constant through the simulations averaging at  $2.1 \cdot 1000 \text{ km}^3/\text{y}$ .

Frazil ice formation is less important than basal growth and is fairly constant through the simulations. Hence, it could not have caused the rapid sea ice declines and the analysis of this process will not be pursued.

### 3.7 Discussion

I based my analyses of the abrupt loss of Arctic September sea ice extent on sea ice volume. In the CCSM3, sea ice volume decreases sooner and faster than the sea ice extent, respectively a loss of 40% and 8% between 1950 and 2000. During the years of the abrupt reductions of Arctic September sea ice extent, the sea ice volume decreases rapidly but not in a surprising way. The sea ice volume loss during the years of abrupt loss has been observed at earlier periods. The Arctic sea ice thinned until it reached a threshold where it could not thin much anymore and then started to lose coverage rapidly, hence the rapid loss of September sea ice extent.

The CCSM3 outputs the amount of sea ice area and volume changes from dynamic and thermodynamic processes separately. Using these variables, dynamic and thermodynamic processes are equal in weight for both sea ice area and sea ice volume. Over the short period of rapid loss of September sea ice extent, both dynamic and thermodynamic processes are almost equal with dynamic processes slightly increasing suggesting a modestly more important contribution from dynamic processes than thermodynamic processes. These results differs from [Holland et al. \(2006a\)](#) who stated that dynamic processes played little role in the abrupt loss of September sea ice extent.

Sea ice transport out of the Arctic Ocean mainly happens through the Fram Strait while the transport through the Barents sea opening, the Canadian Arctic Archipelago and the Bering Strait are negligible in comparisons. Table 3.2 describes the relative strength of the

different processes during the early 20<sup>th</sup> century before the rapid declines, at the time of the rapid declines, and by the end of the 21<sup>st</sup> century after the rapid declines.

Processes	1900-1909	Events	2090-2099
Surface melt	-3	-3.5	-2
Bottom melt	-4	-6	-5
Lateral melt	-1	-1	-1
Basal growth	10	10	6
Frazil formation	2	2	2
Total Melt	-8	- 9.5	-8
Total formation	12	12	8
Thermodynamic	4	2.5	0
Transport	-4	-2	-1

Table 3.2: Sea ice volume changes due to melt and formation at three different periods: 1900-1909, at the abrupt loss events and 2090-2099. All volume changes are in  $1000 \text{ km}^2/\text{y}$ .

Rapid loss events are caused by increased melt. Until the rapid loss of September sea ice extent events, melt increases, formation stagnates and transport decreases leaving only the melt to cause major modification of the sea ice. The surface melt is driven by surface fluxes. The sum of all the surface fluxes is of  $-5 \text{ W/m}^2$  in 1900 and increases up to  $3.5 \text{ W/m}^2$  by 2100, a  $8.5 \text{ W/m}^2$  gain over 200 years. It went from cooling the sea ice to warming it. The bottom melt is driven by the turbulent heat flux from the sea ice to the ocean. It starts at  $-20 \text{ W/m}^2$  in 1900 and ends at  $-120 \text{ W/m}^2$  in 2100. The ocean heat transfer increased by  $80 \text{ W/m}^2$  over 200 years. This massive increase of ocean heat transferred to sea ice is intriguing and it will be addressed in chapter 4. The heat exchanges between the ocean and sea ice are driven by the friction velocity and the sea surface temperature. While the friction velocity increases mildly the sea surface temperature increases considerably. Therefore, the sea surface temperature governs the turbulent heat flux between the ocean and the sea ice. It can be observed from the similarities between the sea surface temperature and the turbulent heat flux curves; they are alike up to a minus sign.

Since the ocean fluxes contributed more to the sea ice melt than the surface fluxes and has undergone more significant changes, it must be the primal energy source causing sea ice decrease. At this point, not a single process can solely explain the rapid loss of sea ice extent. I still agree with the conclusion of [Holland et al. \(2006a\)](#) which stated that the rapid loss of September sea ice extent is caused by years of high annual variability in conjunction with thinner sea ice.

The next chapter of this thesis aims at understanding the incredible increase of ocean heat transferred to the sea ice. Sea surface temperature is the main contributor to this heat exchange. The energy sources affecting the sea surface temperature will be investigated through the energy budget of the ocean part of the CCSM, the POP model.

## 4 Energy budget of the ocean component of the CCSM

As demonstrated in chapter 3, the ocean plays an important role in the sea ice mass balance. The sea surface temperature is the most important factor controlling the amount of energy transferred from the ocean to the sea ice. The CCSM sea surface temperature is defined as the temperature of the top layer of the ocean component. We want to quantify the different elements affecting the top layer of the ocean.

Reconstructing the temperature-energy equation - proving that the temperature is conserved - would confirm that all the energy sources are accounted for and provide an accurate analysis. We refer to this exercise as closing the temperature-energy budget. The CCSM3 is known to be energy conservative (Smith and Gent, 2004b) but it does not mean that the standard output allows the user to close the energy budget.

This chapter can be read as a tutorial on how to close the energy budget of a global climate model and how to obtain the code definition of variables in the model. The tutorial sections can be skipped to obtain only the results of the energy budget. Closing the energy budget of a climate model proved to be a tedious and challenging task. This chapter could be helpful to any researcher attempting similar calculations. Similar projects occurred and my work on the energy budget of the CCSM has already been helpful to A. Nummelin and M. Gervais.

The derivation of the theoretical energy equation is presented in section 4.1. How to access a list of the output variables for the CCSM3 is explained in section 4.2 along with the temperature budget of the ocean component of the CCSM3. Results of the temperature budget of the CCSM4 can be found in section 4.3. The coding of the temperature equation in the CCSM4 is presented in section 4.4. Concluding remarks are in section 4.5.

### 4.1 Energy equation

The CCSM is based on the Navier-Stokes equations and the energy equation for fluids. We could directly jump to the temperature or internal energy equation, however, it would be relevant to review the theoretical derivation of the energy equation. The energy density ( $J/m^3$ ) of a fluid can be split into three parts: kinetic, potential and internal. The kinetic

energy density,  $K$ , is given by:

$$K = \frac{u^2}{2}, \quad (4.1)$$

where  $u^2 = \vec{u} \cdot \vec{u}$  is the norm of the velocity vector  $(u, v, w)$  squared. The potential energy density,  $U$ , is given by:

$$U = g z, \quad (4.2)$$

where  $g$  is the gravitational constant and  $z$  is the height. In the case of an ideal gas, the internal energy is proportional to the temperature;  $I = c_{p,v}T$  where  $c_{p,v}$  is the heat capacity with constant pressure with the subscript  $p$  and with constant volume with subscript  $v$ . Taking the thermodynamic definition of the internal energy applied for an incompressible fluid ( $\rho = \rho_0$ ,  $dV = 0$  if the temperature is constant), we obtain

$$dI = c_v \cdot T + \left[ T \frac{\partial P}{\partial T} - P \right] dV = c_v \cdot T \Rightarrow I = c_v \cdot T. \quad (4.3)$$

The internal energy is proportional to the temperature,

$$I = c_p T. \quad (4.4)$$

The total energy,  $E$ , of a volume  $V$ , is:

$$E = \int_V \rho (K + U + I) dV. \quad (4.5)$$

where  $\rho$  is the density. The temporal change of the total energy must be equal to the energy flux integrated over the surface,  $S$ , of the volume:

$$\frac{\partial E}{\partial t} = - \oint_S \rho (K + U + I) \vec{u} \cdot \hat{n} dS, \quad (4.6)$$

where  $\hat{n}$  is a unit vector perpendicular to the surface and pointing outward.

Other sources of energy includes: pressure work, diffusion and surface interactions. The pressure work done on the system per surface area is given by the pressure,  $P$ , times the

displacement,  $\vec{x}$ ,

$$W = P \hat{n} \cdot \vec{x}. \quad (4.7)$$

Over a small time increment, the pressure can be considered constant leading to:

$$\frac{\delta W}{\delta t} = \frac{\delta(P \hat{n} \cdot \vec{x})}{\delta t} = P \hat{n} \cdot \frac{\delta \vec{x}}{\delta t} = P \hat{n} \cdot \vec{u}. \quad (4.8)$$

The total pressure work done per unit of time over the volume  $V$  with surface  $S$  is given by:

$$\frac{\Delta W}{\Delta t} = \oint_S P \hat{n} \cdot \hat{u} dS. \quad (4.9)$$

The diffusion,  $\vec{q}$ , can be written using Fourier's law for heat fluxes,

$$\vec{q} = -\chi \nabla T, \quad (4.10)$$

where  $\chi$  is the thermal conductivity in  $W/(m K)$ . The total diffusive heat flux over a volume is given by:

$$\oint_S \vec{q} \cdot \hat{n} dS. \quad (4.11)$$

The last piece of the energy budget is the surface interactions: radiation, latent and turbulent heat fluxes. We define the surface interaction term,  $\vec{F}$ , as zero inside the volume  $V$  and equal to  $F$  at the top surface of the volume. The total energy income from surface interactions can then be written as:

$$\oint_S \vec{F} \cdot \hat{n} dS. \quad (4.12)$$

Note that some of the fluxes will be transmitted through the fluid (e.g. solar flux) and will contribute to  $F$  even if the surface of the volume  $V$  is not at the surface of the ocean.

Using the equations 4.5, 4.6, 4.9, 4.11 and 4.12, the energy equation can be written as:

$$\int_V \frac{\partial}{\partial t} [\rho(K + U + I)] dV = \oint_S \left[ -\rho \vec{u} \left( K + U + I + \frac{P}{\rho} \right) - \vec{q} + \vec{F} \right] \cdot \hat{n} dS. \quad (4.13)$$

Using the divergence theorem on the right hand side of the equation, we obtain

$$\int_V \frac{\partial}{\partial t} [\rho(K + U + I)] dV = \int_V \nabla \cdot \left[ -\rho \vec{u}(K + U + I + \frac{P}{\rho}) - \vec{q} + \vec{F} \right] dV. \quad (4.14)$$

The last equation is valid for any volume implying that the integrands must be equal, leading to:

$$\frac{\partial}{\partial t} [\rho(K + U + I)] = \nabla \cdot \left[ \rho \vec{u}(K + U + I + \frac{P}{\rho}) - \vec{q} + \vec{F} \right]. \quad (4.15)$$

Equation 4.16 is the energy equation for a three-dimensional fluid.

Most models do not solve that equation directly. Usually, their advection scheme balances kinetic energy plus potential energy and pressure,

$$\frac{\partial}{\partial t} [\rho(K + U)] = \nabla \cdot \left[ \rho \vec{u}(K + U + \frac{P}{\rho}) \right]. \quad (4.16)$$

Under those conditions, the energy equation becomes the internal energy equation:

$$\frac{\partial}{\partial t} [\rho I] = \nabla \cdot \left[ \rho \vec{u}I - \vec{q} + \vec{F} \right], \quad (4.17)$$

which can be rewritten in terms of the temperature,

$$\frac{\partial}{\partial t} [\rho c_p T] = \nabla \cdot \left[ \rho \vec{u}c_p T - \vec{q} + \vec{F} \right]. \quad (4.18)$$

The ocean part of the CCSM, the POP model, solves this equation.

## 4.2 Energy budget for the CCSM3

In order to complete the energy budget for the CCSM3, we must retrieve every term of equation 4.18 as a variable output from the simulations. The standard output of the CCSM3 can be found in the monthly history files. Those files include all the output fields averaged monthly. It is possible to access one of the history file through the Earth System Grid web site<sup>3</sup>. If the reader owns a NCAR YubiKey, typing ‘hs1’ in a terminal connects the user to

---

<sup>3</sup><https://www.earthsystemgrid.org/home.html>

Name	Definition	Unit
SHF	Surface fluxes absorbed by the ocean.	$W/m^2$
QFLUX	Frazil ice formation.	$W/m^2$
HDIIFT	Vertically integrated horizontal divergence of heat diffusion.	$cm\text{ }^\circ C/s$
UET	Advective flux of Heat in grid-x direction	$^\circ C/s$
VNT	Advective flux of Heat in grid-y direction	$^\circ C/s$
WTT	Advective flux of Heat in grid-z direction	$^\circ C/s$
ADVT	Vertically integrated temperature advection tendency	$cm\text{ }^\circ C/s$
TEMP	Potential temperature	$^\circ C$
TAREA	Area of T cells	$cm^2$
dz	Thickness of layer k	$cm$
cp_sw	Specific heat of sea water	$erg/g/K$
rho_sw	Density of sea water	$g/cm^3$

Table 4.1: CCSM3 output variables required for the energy budget.

NCAR High Performance Storage System (HPSS) where all the outputs are stored. The ocean history files are located at /CCSM/csm/"RunName"/ocn/hist/. Using the command ‘get’, the user can transfer the file to his or her own account and then work with the data. The list of the variables included in a file can be shown by using NETCDF<sup>4</sup> command ‘ncdump -h "FileName" | less’. The option ‘-h’ only shows the variables’ description and not the data. The option ‘| less’ will show enough information to fit the terminal size. It is then possible to go through the list pressing *Enter*. The heat transfer related variables include: surface fluxes, frazil ice formation, vertically integrated horizontal divergence of heat diffusion, advective heat fluxes in all three spatial directions, vertically integrated temperature advection tendency, potential temperature and some constants, see table 4.1.

The surface fluxes include evaporation, sensible heat, emitted and absorbed longwave, melt, snow, ice runoff and absorbed short wave. The units of the fluxes are different. The surface fluxes and the frazil ice formation are in units of  $W/m^2$ . The advective heat fluxes are in  $^\circ C/s$ . The vertically integrated divergence of heat units is  $cm\text{ }^\circ C/s$ . We must convert the heat fluxes to a unique unit. We chose the watt (J/s). The surface fluxes and the frazil ice formation must be multiplied by the surface area in unit of meters instead of centimeters. The advective and diffusive fluxes must be multiplied by the surface area, the sea water density and the specific heat of sea water in unit of  $J/g/K$  instead of  $erg/g/K$ .

---

<sup>4</sup>For more information on NETCDF visit <https://www.unidata.ucar.edu/software/netcdf/docs/faq.html#whatisit>, last visited May 9, 2018.

From table 4.1, the only missing process is the heat diffusion in the three spatial directions. We have the vertically integrated horizontal divergence of heat diffusion though. The vertical divergence of heat diffusion is not required because it sums up to zero. When vertically integrated, the only remaining terms are the surface and the ocean floor diffusion. There cannot be oceanic heat diffusion from the atmosphere or the ocean floor. Hence, both are defined as zero. Only the vertically integrated heat budget can be done without neglecting the heat diffusion. If this budget is accurate, the heat diffusion of each cell can be calculated as the residual of the energy budget of that cell.

All the heat fluxes of the vertically integrated budget are accounted for; the right hand side of equation 4.18. We still have to retrieve the internal energy temporal derivative; the left hand side of equation 4.18. The column internal energy is calculated as the monthly mean temperature times the cell volume, integrated vertically and then multiplied by the sea

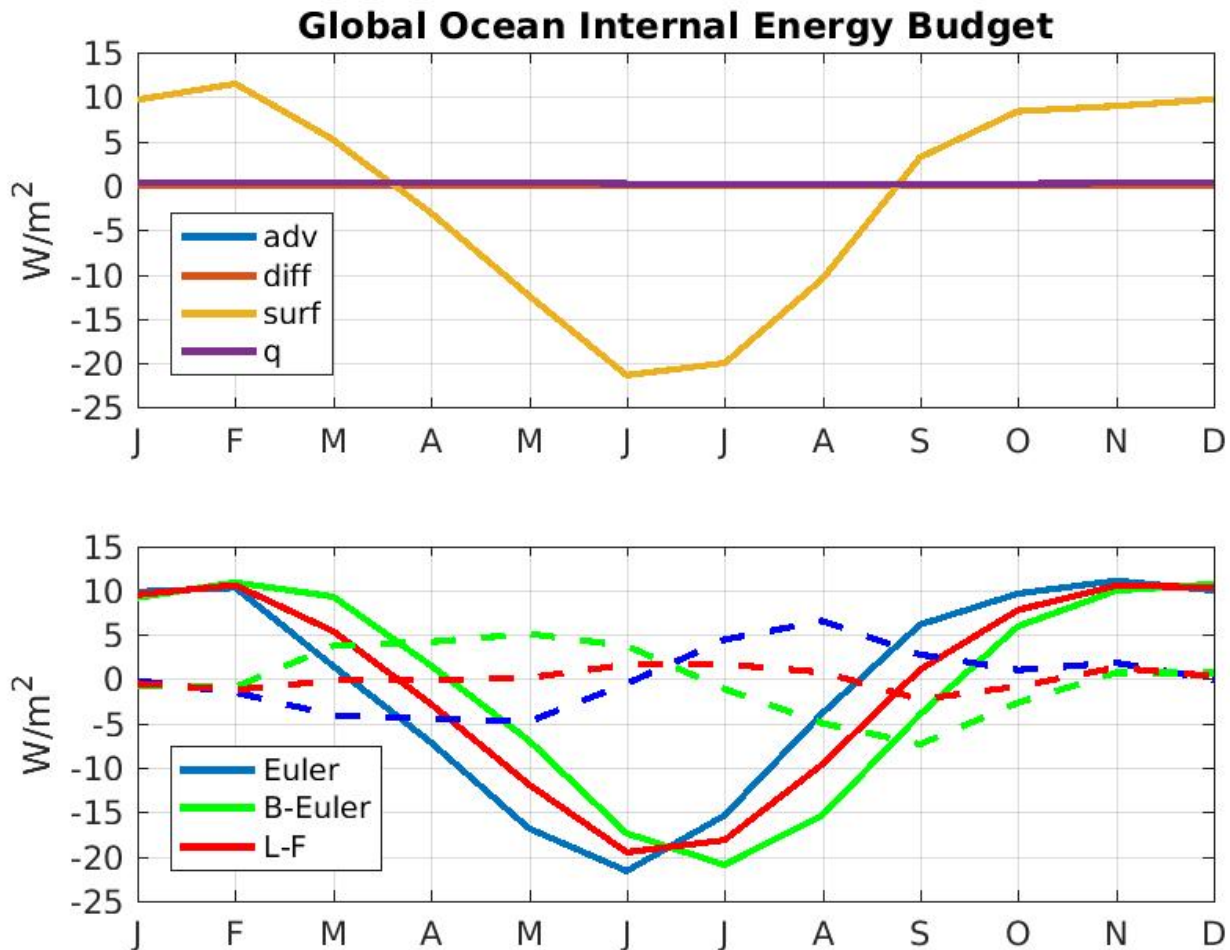


Figure 4.1: Top) Global forcings for the year 1950. Bottom) Temperature temporal derivative for the year 1950 from three schemes (solid) and their associated budget error (dashed): Euler (blue), backward Euler (green) and Leap-Frog (red).

water heat capacity and the sea water density<sup>5</sup>,

$$I = c_p \cdot \rho \cdot \int_{column} T dV. \quad (4.20)$$

The temporal derivative of the internal energy can be calculated using the Euler scheme,

$$\frac{dI}{dt} = \frac{I_{t+1} - I_t}{\delta t}, \quad (4.21)$$

the backward Euler scheme,

$$\frac{dI}{dt} = \frac{I_t - I_{t-1}}{\delta t}, \quad (4.22)$$

or the leapfrog scheme,

$$\frac{dI}{dt} = \frac{I_{t+1} - I_{t-1}}{2\delta t}. \quad (4.23)$$

The results of each scheme are presented.

Every term of the vertical integration of equation 4.18 can be calculated. The column heat budget is ready to be computed. We chose to study the simulation b30.030b.ES01 because it is the main simulation studied by [Holland et al. \(2006a\)](#). It is characterized by the longest and the most apparent rapid September sea ice extent decline. First, we start our analysis of the budget for the oceans altogether. Second, we study the Arctic Ocean budget and third we analyze the column budget. All calculations are for the months of the year 1950.

On a global scale, there is no input of energy from advection or diffusion. All the oceans are boarded by coast. No ocean advection or diffusion can come from it. Only the surface fluxes are bringing energy into the ocean peaking at  $11 W/m^2$  in February and  $-21 W/m^2$  in July, see the top panel of figure 4.1). Note that the surface fluxes are cooling the ocean over the full course of year 1950. The budget error - or the difference between the heat fluxes and the temporal derivative of the internal energy - when using the Euler schemes ranges from  $-7 W/m^2$  and  $6 W/m^2$ . The calculations made with the leapfrog scheme offer the smallest

---

<sup>5</sup>Using the output of the CCSM, the column internal energy is calculated as,

$$cp\_sw \cdot 10^{-7} \cdot rho\_sw \cdot TAREA \cdot \sum_k [TEMP_k \cdot dz_k]. \quad (4.19)$$

We must multiply the heat capacity of sea water by  $10^{-7}$  to change its unit from ergs to joules.

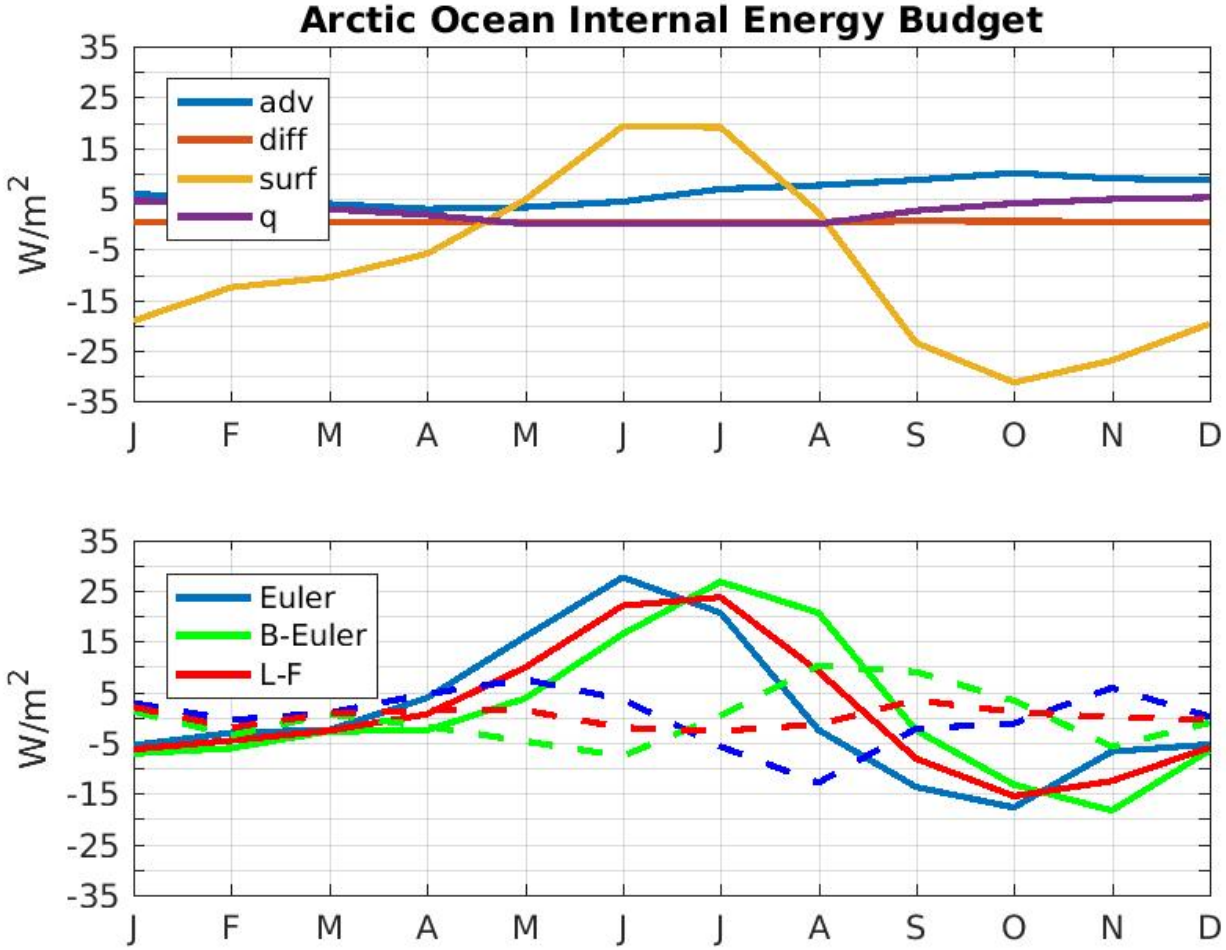


Figure 4.2: Top) Arctic forcings for the year 1950. Bottom) Temperature temporal derivative for the year 1950 from three schemes and its associated budget error (dashed): Euler (blue), backward Euler (green) and Leap-Frog (red).

error, as expected, ranging from  $-2 \text{ W/m}^2$  and  $2 \text{ W/m}^2$ . We expect the vertical diffusive heat fluxes in the ocean to be less than  $1 \text{ W/m}^2$ . It would be impossible to discern between actual vertical diffusive heat fluxes and the budget error.

Over the Arctic Ocean, the surface fluxes are positive, warming the ocean, for four months peaking in June and July at  $19 \text{ W/m}^2$ , see the top panel of figure 4.2). During the winter months, the surface fluxes are cooling the ocean at a minimum of  $-31 \text{ W/m}^2$  in October. The frazil ice formation releases up to  $5 \text{ W/m}^2$  during winter and nothing during summer. The advection of heat inside the Arctic Ocean ranges between  $3$  and  $10 \text{ W/m}^2$  during fall. The diffusion has smaller values than  $1 \text{ W/m}^2$ . The calculations using the the Leapfrog scheme are giving better results over the Euler schemes with a budget error of  $\pm 3 \text{ W/m}^2$  and  $\pm 12 \text{ W/m}^2$  respectively. Alike the global ocean, the budget error is higher than the expected vertical heat fluxes.

Since the leapfrog scheme gave better results globally and over the Arctic Ocean, we

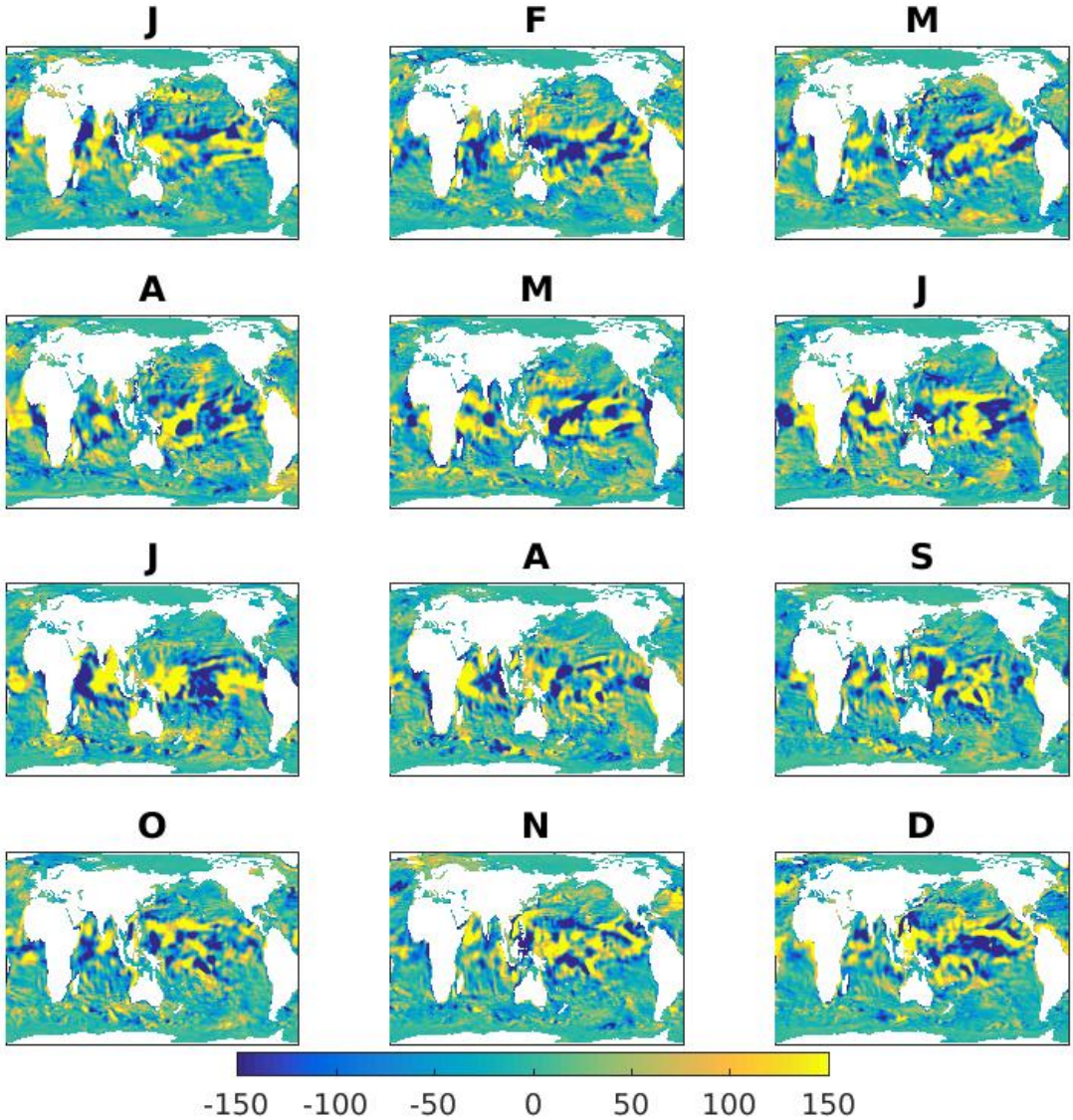


Figure 4.3: Column budget error using the leapfrog scheme for the temporal derivative for every month of year 1950.

decided to look at the column energy budget using that scheme. The averaged column error is of  $\pm 150 \text{ W}/\text{m}^2$  as can be seen in figure 4.3. Though, the column error surpasses  $1000 \text{ W}/\text{m}^2$  for certain columns . Some regions switch from a highly negative error to a highly positive error from a month to the next. North of Australia and New Zealand, there is an area with an error over  $150 \text{ W}/\text{m}^2$  dropping under  $-150 \text{ W}/\text{m}^2$  in February. Then, a combinations of columns with an error of  $150 \text{ W}/\text{m}^2$  and  $-150 \text{ W}/\text{m}^2$  can be found in the same location for the months of March and April. The error becomes over  $150 \text{ W}/\text{m}^2$  again in May and then under  $-150 \text{ W}/\text{m}^2$  in June, etc. The column error decreases significantly when averaged yearly.

The calculated error of the temperature budget is not satisfying using the output of the CCSM3. We believe the error comes from the temporal derivative. Even if the leapfrog

Name	Definition	Unit
SHF	Surface fluxes absorbed by the ocean.	$W/m^2$
QFLUX	Frazil ice formation.	$W/m^2$
HDIIFT	Vertically integrated horizontal divergence of heat diffusion.	$cm\text{ }^\circ C/s$
UET	Advective flux of Heat in grid-x direction	$^\circ C/s$
VNT	Advective flux of Heat in grid-y direction	$^\circ C/s$
WTT	Advective flux of Heat in grid-z direction	$^\circ C/s$
ADVT	Vertically integrated temperature advection tendency	$cm\text{ }^\circ C/s$
TEMP	Potential temperature	$^\circ C$
TAREA	Area of T cells	$cm^2$
dz	Thickness of layer k	$cm$
cp_sw	Specific heat of sea water	$erg/g/K$
rho_sw	Density of sea water	$g/cm^3$
HDIFE_TEMP	Advective flux of Heat in grid-x direction	$^\circ C/s$
HDIFN_TEMP	Advective flux of Heat in grid-y direction	$^\circ C/s$
HDIFB_TEMP	Advective flux of Heat in grid-z direction	$^\circ C/s$
KPP_SRC_TEMP	KPP non local mixing term	$W/m^2$

Table 4.2: CCSM4 output variables required for the energy budget.

scheme improves the results, it is still an approximation. The exact temporal derivative is given by the difference of two instantaneous temperature snapshots. For monthly mean fluxes, the temperature field at 0:00 the first day of the month and the temperature field at 0:00 the first day of the next month are required. But it is not possible with the CCSM3 output. Indeed, it is possible to retrieve restart files for the CCSM3 containing temperature snapshot every 10 years of January 1<sup>st</sup> at 0:00. This temporal resolution is of no use for us since we want to follow rapid sea ice declines spanning over a period of less than 10 years. For that reason, we decided to turn to the CCSM version 4. This version stored restart files yearly providing temperature snapshot every first of January at 0:00.

### 4.3 CCSM4

The CCSM4 uses the same variables as the CCSM3 with the same names plus numerous more, see table 4.2.

It outputs yearly temperature snapshots the 1<sup>st</sup> of January at 0:00. It is now possible to compute an exact temporal derivative of the temperature or internal energy. Since we will be working with yearly variations, it is required to convert all monthly averaged fluxes,  $\overline{F_m}$ , into yearly average,  $\overline{F_y}$ . Note that there are no leap years in the CCSM. All the analyses

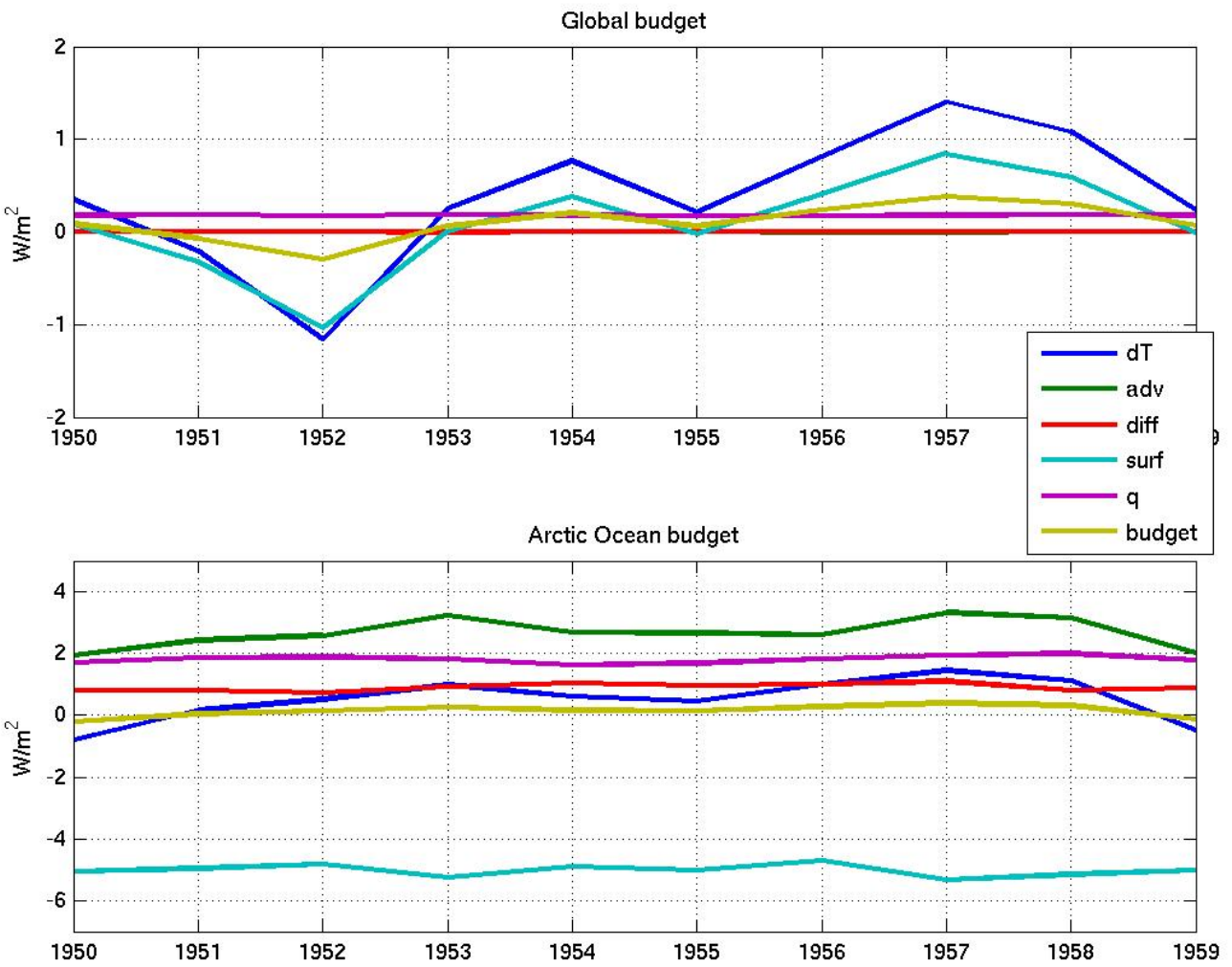


Figure 4.4: Top) Yearly global internal energy budget of the CCSM4. Bottom) Yearly Arctic Ocean internal energy budget of the CCSM4. Following the legend,  $\text{dT}$  stands for the yearly internal energy variation,  $\text{adv}$  for advection,  $\text{diff}$  for diffusion,  $\text{surf}$  for surface,  $\text{q}$  for frazil ice formation and  $\text{budget}$  represented the internal energy variation minus the fluxes.

shown in this chapter are based on the simulation *b40.20th.track1.1deg.012*. We chose this simulation because it contains more output than usual runs being part of the Mother Of All Runs (MOAR). The studied period spans between 1950 to 1959.

The yearly global budget closes up to  $\pm 0.4 \text{ W/m}^2$ . One can see in figure 4.4 that the advection and diffusion sum up to zero. The yearly surface flux varies between  $-1 \text{ W/m}^2$  and  $0.85 \text{ W/m}^2$ . The internal energy temporal derivative varies from  $-1.2 \text{ W/m}^2$  up to  $1.4 \text{ W/m}^2$ . The frazil ice formation is fairly constant over the years at  $0.18 \pm 0.01 \text{ W/m}^2$ . These values are consistent with the yearly mean obtained from the CCSM3.

The yearly Arctic budget closes up to  $\pm 0.4 \text{ W/m}^2$ , see figure 4.4. The fluxes are almost constant through the ten-year period 1950-59. The surface flux is the most important energy sink at  $-5 \text{ W/m}^2$ . The advective flux is the highest energy income at  $2.7 \text{ W/m}^2$  followed by the frazil ice production at  $1.8 \text{ W/m}^2$  and then the diffusion of heat at  $0.9 \text{ W/m}^2$ . The

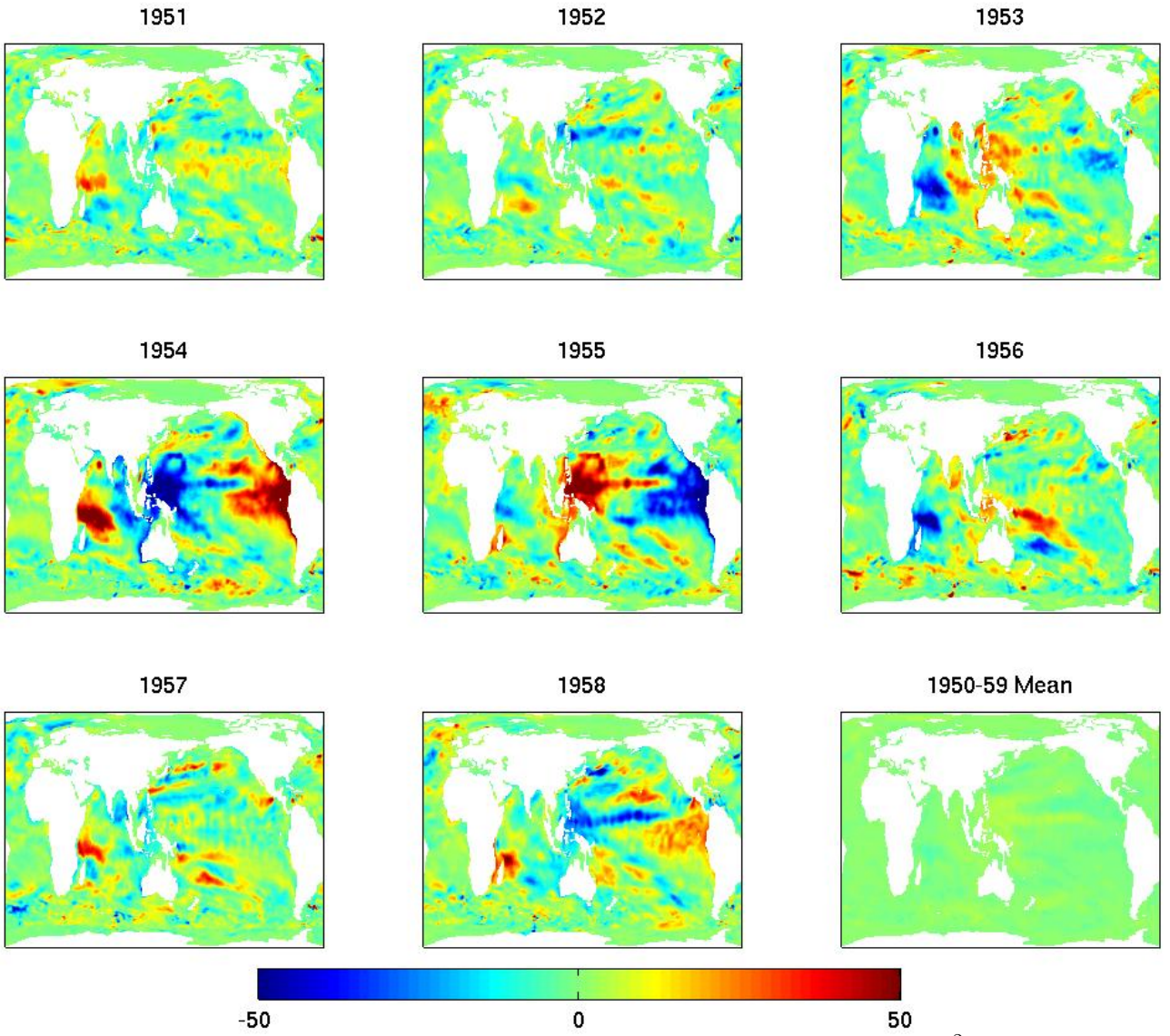


Figure 4.5: Error of the vertically integrated internal energy budget in  $W/m^2$  for the years 1951 to 1958 and in the bottom right corner, the average error over 1950-59.

internal energy temporal derivative ranges from  $-0.8 W/m^2$  to  $1.4 W/m^2$ .

Even if the error of the budget closes satisfactorily globally and over the Arctic Ocean, it is not the case over the ocean columns, see figure 4.5. The column error can reach up to  $\pm 150 W/m^2$  and broad regions are at  $\pm 50 W/m^2$ . It also changes from very positive to very negative between each year. For example, north of Australia and New Zealand, the error is  $50 W/m^2$  in 1953 then switches to  $-50 W/m^2$  in 1954 and back to  $50 W/m^2$  in 1955. It is an improvement compared to the CCSM3. The average error when from  $\pm 150 W/m^2$  for the CCSM3 down to  $\pm 50 W/m^2$  for the CCSM4. The maximum error when from  $1000 W/m^2$  for the CCSM3 down to  $150 W/m^2$  for the CCSM4.

Once averaged over the decade, the column error shrinks down to  $\pm 10 W/m^2$  with the majority of the domain being at  $\pm 1 W/m^2$ . Since the model solves the temperature equation, it should be possible to close it up to machine accuracy using the right variables. The missing

process or processes have the following properties: (1) they range between  $\pm 150 \text{ W/m}^2$ , (2) they cancel when integrated globally, (3) they cancel when integrated over the Arctic Ocean, (4) their value decreases significantly when averaged over a decade. After inspecting carefully the complete list of output variables, we conclude that the missing field is not included in the standard output of the MOAR. In the next section, we delve into the CCSM4 code to investigate which physical process is missing.

#### 4.4 CCSM coded temperature equation

Tracking the definition of a variable in a gigantic code such as the CCSM is laborious. There are no direct ways to follow a variable through the code up to its equation. The variables are constantly changing names and are sometimes calculated as temporary variables in a specific routine. The approach I followed consisted of taking one variable at a time and following its lead as far as possible. First, I found all the occurrences of the variable name using the terminal command 'grep VarName \*.F90'. Second, I scrutinize all the entries in the terminal directly in the Fortran90 code file. Third, if the name of the variable changes, I restart at step one with the new name. At some point, the code and the variables start revealing themselves making searches easier and faster. How to obtain the CCSM versions 3 and 4 code is explained in appendix A. Every code part required to understand the different variables of the internal energy budget of the CCSM can be found in appendix A.

The temperature equation of the CCSM4 adds the results of six subroutines: (1) horizontal diffusion, (2) advection, (3) vertical diffusion, (4) reset temperature, (5) KPP parameterization, (6) short wave radiation absorption. The horizontal diffusion is the first element of the temperature budget being called. There are three diffusion schemes: laplacian, biharmonic and Gent-McWilliams. The simulation *b40.20th.track1.1deg.012* used the Gent-McWilliams scheme. The Gent-McWilliams scheme is described in [Gent and Mcwilliams \(1990\)](#). The CCSM calculates the horizontal diffusion of heat through a side of a cell as the product of the side area of the cell ( $A_{side}$ ), the spatial derivative of the temperature perpendicular to

the side area ( $\frac{dT}{dx_{\perp}}$ ) and a diffusive coefficient ( $\kappa$ ),

$$D = A_{side} \cdot \frac{dT}{dx_{\perp}} \cdot \kappa. \quad (4.24)$$

The diffusive coefficient includes conventional and Gent-McWilliams diffusive coefficients. The MOARs have more output which includes eastward and northward heat diffusion. Usually, only the vertically integrated divergence of heat diffusion is output,  $\int(D_{west} - D_{east} + D_{south} - D_{north})dz$ .

The second element of the temperature budget is the heat advection. It is output as the eastward, northward and bottom heat fluxes and also as the vertically integrated divergence of heat advection. The heat advection on a side of a cell is given by  $Adv = A_{side} \cdot T_{side} \cdot u_{side}$ .

The third element of the temperature equation is the vertical diffusion. It is calculated as the difference between the top and the bottom vertical diffusion,  $T_{bottom} \cdot \kappa_{bottom} - T_{top} \cdot \kappa_{top}$ . For the surface layer, several surface interactions are added: evaporation, sensible heat, emitted and absorbed longwave, melt, snow and ice runoff. They are output separately or as a bundle with the shortwave radiation. The vertical diffusion is not part of the standard or MOAR output.

The fourth element is the reset temperature process. When the ocean temperature goes under the freezing point, the model resets the ocean temperature back at the freezing point. The involved energy is used to form frazil ice. There is a variable for frazil ice formation in the standard output. However, nothing in the code seemingly ties this variable to what is calculated in the temperature equation. We will use the standard output frazil formation variable to cover this part of the temperature equation.

The fifth element of the temperature equation treats of vertical KPP mixing parameterization. [Large et al. \(1994\)](#) developed it. It is given by the product of all the surface forcings times a nonlocal diffusivity coefficient,  $F_{surf} \cdot \kappa_{kpp}$ . This nonlocal term is bewildering and is still misunderstood in the community though well accepted. It is based on boundary layers physics for the atmosphere, which is well developed, and adapted for the ocean. The divergence of KPP mixing is part of the standard output of the CCSM4 as KPP\_SRC\_TEMP. This variable was not present in our previous analysis whereas its vertical integration is nul.

There is no mixing at the surface of the ocean or at the ocean floor.

The sixth, and last, element of the temperature budget is the short wave absorption. It is part of the standard output and in a bundle including all surface fluxes excluding frazil ice formation.

All the parts of the temperature equation have been reviewed. There are outputs to calculate the results for five of the six elements of the temperature equation. Only the vertical diffusion is missing. A vertically integrated budget brings that term to zero. The only new process that was missing is the non-local KPP mixing parameterization. It does not alter the previous results since it is null when vertically integrated. In the end, all this code verification does not improve the internal energy budget done in the previous sections of this chapter.

## 4.5 Conclusion

Our goal was to study all the energy sources affecting the first layer of the Arctic Ocean. The CCSM3 is lacking the vertical diffusive heat fluxes and the snapshot temperature for an exact temperature temporal derivative. It is tempting to calculate the vertical heat diffusion as a residual of all the other fluxes. While it is possible to calculate the heat advection through a truncated column using eastward and northward advective heat fluxes, it is not possible for the diffusion since the variables are not output. All the horizontal and vertical diffusion would end up in the residual. The estimated error on that result would be the budget error,  $3 W/m^2$ . Since the vertical heat fluxes are generally low, under  $1 W/m^2$  in the Arctic Ocean, we find this error too important.

The MOAR of the CCSM4 offers more options since the eastward and northward diffusive heat fluxes are output with the KPP vertical mixing. Yearly temperature snapshots allow for an exact calculation of the temporal derivative. Again, the vertical heat diffusion is not output. It is now possible to compute the mean vertical diffusion globally or over the Arctic Ocean with an estimated error of  $0.4 W/m^2$ . Even if this error is acceptable in terms of vertical diffusion, we have not been able to close the internal energy budget for the columns. Its error reaches over  $150 W/m^2$  for both the CCSM versions 3 and 4. This uncertainty does

not raise enough confidence to trust the estimated error of  $0.4\text{ W/m}^2$  without a reasonable explanation. We do not hold any convincing explanation for the extremely high column budget error. We regretfully stop our analysis of the first layer of the CCSM ocean model for that reason.

The oceanic temperature has a considerable effect on the sea ice and the Arctic as shown in chapter 3. It is mandatory to understand the sources of heat affecting it if we want to understand the future of the Arctic. To do so, a reconstruction of the temperature/heat equation is required. This chapter showed the limit of the CCSM output to reconstruct the temperature/heat equation.

Even if it is not possible to study in detail each source of heat reaching the surface layer of the Arctic Ocean, it is possible to study the evolution of some sources. The next chapter is dedicated to the advective heat transport through the gateways of the Arctic Ocean.

## 5 Ocean advective heat fluxes through the gateways of the Arctic Ocean simulated by the CCSM version 3 and 4

The heat fluxes entering the Arctic Ocean are increasing. There are intrusions of anomalously warm water (1) from the Atlantic (Holliday et al., 2008; Schauer et al., 2008), (2) from the Pacific (Woodgate et al., 2010), (3) over the Arctic shelves (Dmitrenko et al., 2010), (4) along the Arctic continental margin (Dmitrenko et al., 2008), (5) into the central Arctic (Polyakov et al., 2005) and (6) in the Canada Basin (McLaughlin et al., 2009). The waters entering the Arctic are warmer and penetrates further than before. They contribute to the Arctic warming which results in a decline in sea ice coverage, thickness, and volume (Kwok et al., 2008). Understanding the advective heat fluxes entering the Arctic Ocean is key to forecast the future of its sea ice. The model community does not extensively study the heat transport through the gateways of the Arctic Ocean. It concentrates its energy on freshwater transport (Wijffels, 2001; Lehner et al., 2012) since it has a considerable effect on the global thermohaline circulation. Holland et al. (2006a) considered the total heat transport through the 55<sup>th</sup> parallel. This type of analysis is the norm for the model community concerning heat transport. This chapter studies the heat transport to the Arctic region defined in figure 3.1 and separates the contribution from each gateway.

### 5.1 Introduction

As seen in chapter 3, the ocean plays an important role in the sea ice mass balance. For the six A1B SRES simulations of the CCSM3, the ocean heat transfer to the sea ice has increased more significantly than any other process. The temperature of the top ocean layer is the main factor of this heat transfer. Disappointingly, it is impossible to account for all the heat fluxes affecting the first layer of the ocean model of the CCSM as shown in chapter 4. It is possible to study available heat fluxes though.

In this chapter we study the advective heat fluxes through the Arctic gateways as simulated by the CCSM versions 3 and 4. The CCSM version 3 has 40 vertical levels and version

4 has 60 vertical levels which required a reshaping of the Arctic Ocean gateways. One would expect that these changes in shape would alter the simulated fluxes through the gateways. The changes in shape are described in each according section. Five of the six CCSM3 simulations of the SRES A1B presented in chapter 3 are studied. Simulation *a* does not have the correct output for this analysis. To the five simulations of the CCSM3, the five simulations of the CCSM4 under the RCP 6.0 scenario are added. The RCP 6.0 scenario is the closest scenario to the SRES A1B.

Each gate is analyzed separately: Fram Strait (section 5.2), Barents Sea Opening (section 5.5), Canadian Arctic Archipelago (section 5.4) and Bering Strait (section 5.5). The locations of each gate are depicted in figure 3.1. Each section presents the bathymetry of the gateway, its heat transport, its volume transport and its temperature. Only the mean values of the simulations of each model are discussed here. As will be seen further, the interannual variability of the different simulations is less important than the trend of their means; the variations between simulations are low compared to their the trend evolution. The heat and volume transports are compared to observations. In the discussion, section 5.6, the volume and heat transport budget of the Arctic Ocean are analyzed.

Advectional heat fluxes are calculated as:

$$F_{adv} = C_p \cdot \rho \cdot A \cdot T \cdot u, \quad (5.1)$$

where  $C_p$  is the heat capacity,  $\rho$  the density,  $A$  is the area the current goes through,  $T$  is the temperature of the current and  $u$  is its velocity. When it comes to advective heat fluxes - such as the heat transport through the gateways of the Arctic Ocean -, a partial heat budget is equivocal due to the Divergence Theorem (Stoke's Theorem),

$$\int_V \frac{dT}{dt} dV = \int_A (T \cdot u) dA. \quad (5.2)$$

Only a complete budget integrated over the full area of the volume has a clear impact on the temperature. The next examples illustrate the various complications arising for working with advective heat fluxes.

First example, if the temperature is negative, the current contributes a negative amount of energy which is erroneous. To make up for the negative heat flux, one avenue is to calculate the heat flux as the velocity multiplied by the difference between the freezing temperature and the actual temperature,

$$F \propto v \cdot (T - T_f). \quad (5.3)$$

This approach nullifies the problematic negative amount of energy. Also, it does not impair the result of the complete budget under the Boussinesq approximation.

With the advective heat flux calculation from equation 5.3, all entering fluxes are now positive. It may seem any entering current provides energy and therefore warms the body of water it enters which is also erroneous. As a second example, imagine a  $5^{\circ}C$  current entering a body of water. If the body of water is at  $10^{\circ}C$ , the current would cool it. If the body of water is at  $2^{\circ}C$ , the current would warm it. In each situation, the body of water receives the same amount of heat but the effects are opposite. To fix this problem, one could calculate the heat flux using the difference between the temperature and the temperature of the close region the current floes into,

$$F \propto v \cdot (T - T_{next}). \quad (5.4)$$

When integrated over the full area of the volume, this approach does not hold the same result as the usual definition of the heat flux. This method gives a better insight regarding warming or cooling in the vicinity but it loses the ability to give the correct amount of energy transferred to the volume it enters. One might hope that using the mean temperature of the volume could solve that problem but it does not. The mean temperature is bound to change with time which will affect any time related averaging, integration and derivation.

The work in this chapter uses the usual definition of the advective heat flux as in equation 5.1. We keep in mind the complications presented in the last paragraphs by comparing the relative strength of the different heat fluxes avoiding any speculations on how much warming or cooling they cause.

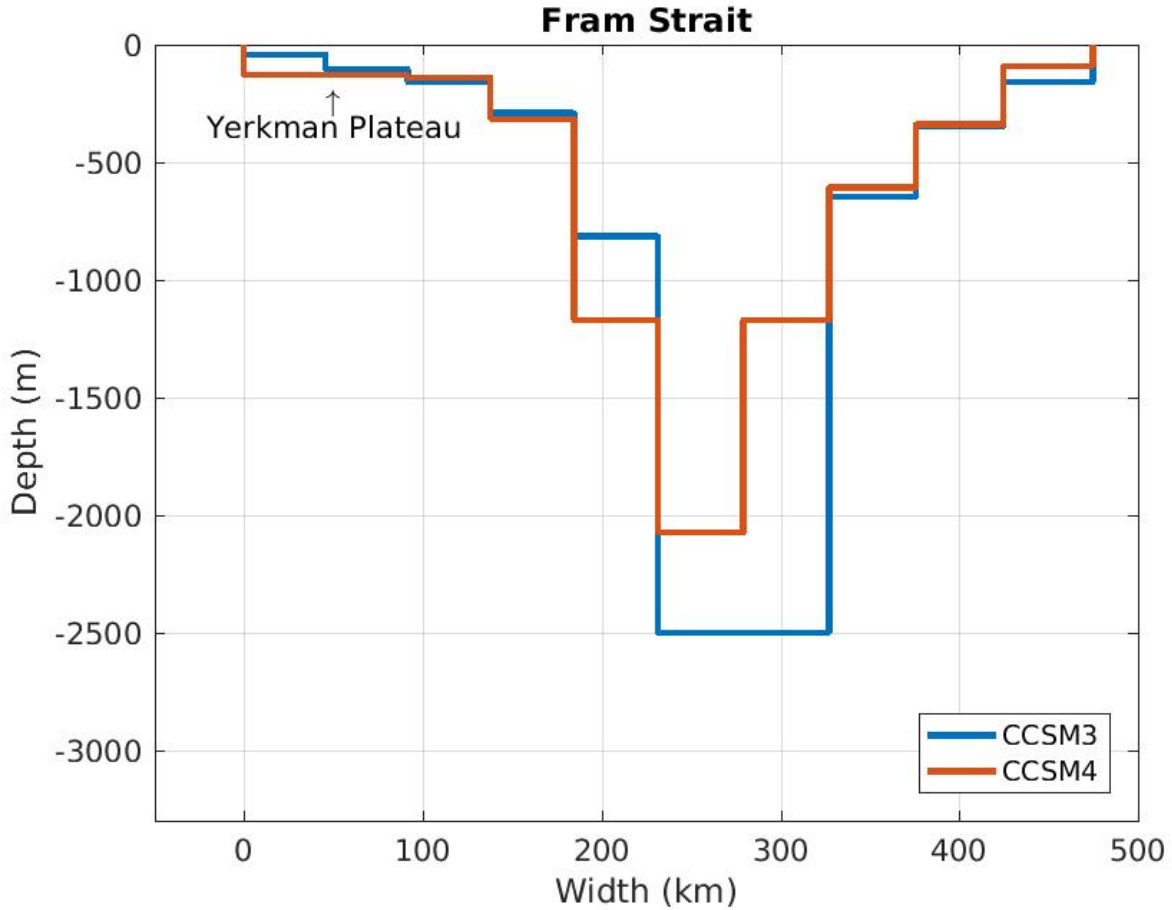


Figure 5.1: Bathymetry of the Fram Strait for the CCSM version 3 in blue and version 4 in red. The Yerkman Plateau is located on the left side (west) of the Fram Strait. Completely on the left (west) is Greenland and on the right (east) side is Svalbard.

## 5.2 Fram Strait

The Fram Strait is the main sea ice export location as seen in chapter 3. Its shape is presented in figure 5.1. The reshaping of the Fram Strait made it shallower and narrower. Its maximum depth is 2500 m for the CCSM3 and 2075 m for the CCSM4. The total area of the Fram Strait is 361 km<sup>2</sup> for the CCSM3 and 291 km<sup>2</sup> for the CCSM4 which represents a loss of 20% of the CCSM3 area. From observations, the Fram Strait has a plateau 2500 m deep expanding over 200 km (Beszczynska-Moller et al., 2011). The CCSM3 modelled Fram Strait is not wide enough at the bottom compared to observation. The CCSM4 modelled Fram Strait is not wide enough at the bottom and is too shallow compared to observations.

The yearly advective heat flux through the Fram Strait ranges between 2 TW and 20 TW averaging at 9 TW for both the SRES A1B and the RCP 6.0 during the 20<sup>th</sup> century, as seen in the first row of figure 5.2. Over the 21<sup>st</sup> century, the advective heat flux of the SRES

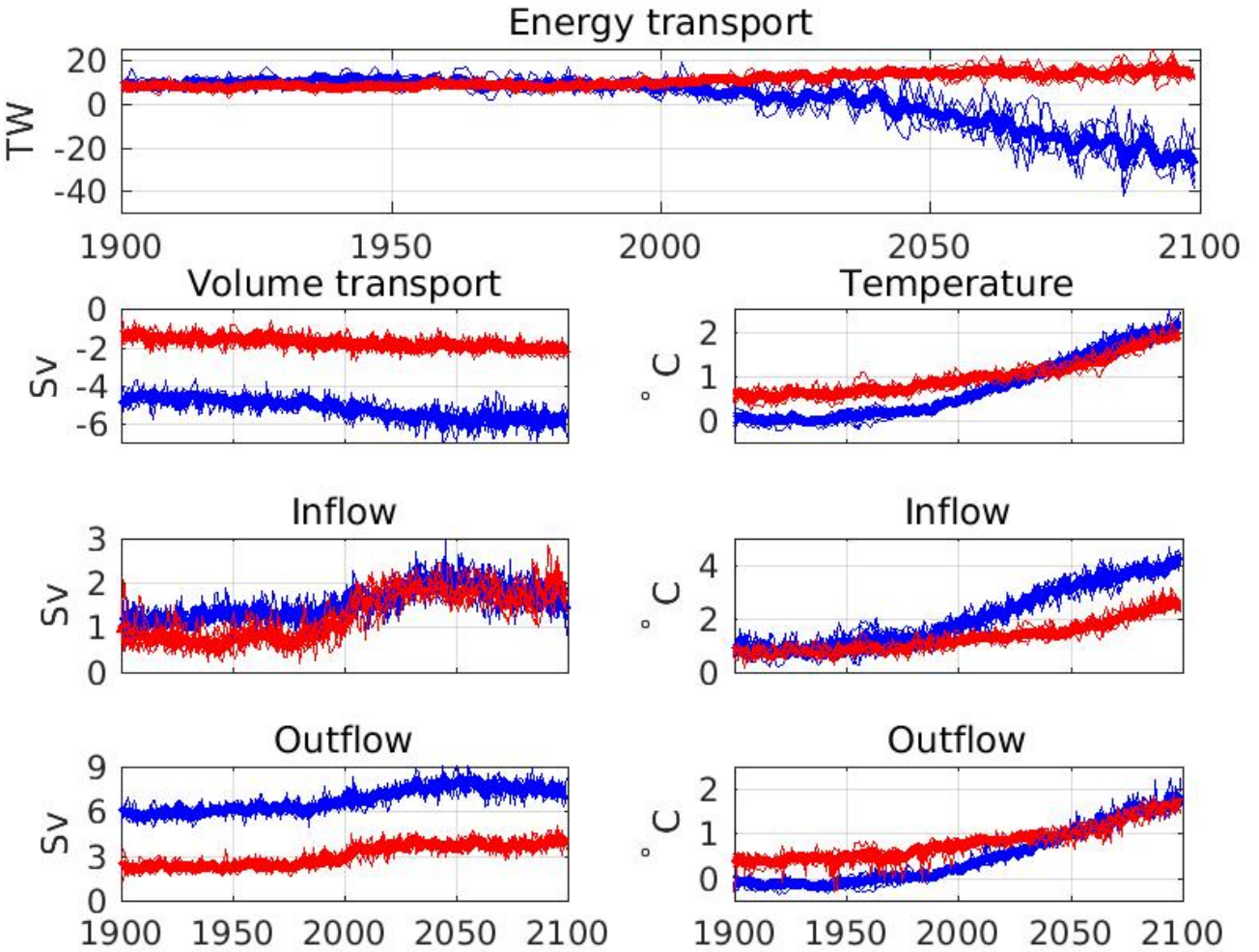


Figure 5.2: Fram Strait energy transport, volume transport and temperature for the CCSM3 in blue and the CCSM4 in red. The volume transport and temperature are divided as: averaged over the full gateway (second row), averaged over the inflow (third row), averaged over the outflow (fourth row).

A1B simulations decreases rapidly at a rate of  $-0.35 \text{ TW}/y$  ending at  $-25 \text{ TW}$ . The heat flux from the RCP 6.0 simulations increases steadily at  $0.05 \text{ TW}/y$  ending at  $15 \text{ TW}$ . Schauer and Beszczynska-Moeller (2009) measured a mean advective heat flux of  $36 \pm 6 \text{ TW}$  between 1997 and 2009 from moorings. Curry et al. (2005) measured  $29 \text{ TW}$  during the years 1980-2005. During the period 1980-2010, the mean heat transport is  $8 \text{ TW}$  for the CCSM3 and  $9 \text{ TW}$  for the CCSM4. The maximum values of the different simulations are under  $20 \text{ TW}$ . The simulated heat transport through the Fram Strait is too weak compared to observations.

The total volume of water through the Fram Strait is negative and steadily increases in magnitude, see the left plot of the second row of figure 5.2 . It starts at  $-4.7 \text{ Sv}$  for the CCSM3 and ends at  $-5.7 \text{ Sv}$ . For the CCSM4, it starts at  $-1.4 \text{ Sv}$  and end at  $-2.1 \text{ Sv}$ . Schauer et al. (2008) measured  $-2.0 \pm 2.7 \text{ Sv}$  between 1997-2007 while Rudels et al. (2008) obtained  $-1.7 \text{ Sv}$ . For the years 1980-2010, the CCSM3 simulated  $-5 \text{ Sv}$  and the CCSM4

$-1.8 \text{ Sv}$ . CCSM3 and CCSM4 simulations agree with measurements.

The simulated inflow through the Fram Strait has three phases, see the left plot of the third row of figure 5.2. For the CCSM3, the first phase starts at  $1.1 \text{ Sv}$  and increases at a pace of  $0.0025 \text{ Sv}/y$  until 1980. The second phase consists of a rapid increase of  $0.01 \text{ Sv}/y$  reaching  $2.4 \text{ Sv}$  by 2050. During the third phase, the inflow through the Fram Strait decreases steadily down to  $1.5 \text{ Sv}$ . The first phase of the CCSM4 inflow starts with a plateau at  $0.7 \text{ Sv}$ . The second phase is made of a rapid nonlinear increase up to  $2 \text{ Sv}$  by 2050. The third phase is a plateau at  $1.8 \text{ Sv}$ .

The simulated outflows follow a similar three phases design, see the left plot of the fourth row of 5.2. First, the CCSM3 outflow increases slowly from  $5.9 \text{ Sv}$  in 1900 up to  $6.2 \text{ Sv}$  in 1980. Second, it increases rapidly until 2050 reaching  $8.2 \text{ Sv}$ . Third, it decreases down to  $7.2 \text{ Sv}$  by 2100. The first phase of the outflow of the CCSM4 is a plateau at  $2.3 \text{ Sv}$ . The second phase consists of a nonlinear increase up to  $4.2 \text{ Sv}$  by 2030. The third phase is a plateau at  $3.8 \text{ Sv}$ . The outflow increase is more important in the CCSM3 than the CCSM4.

The simulated inflow and outflow temperatures increase exponentially, see the three plots on the second column of figure 5.2 from the second to the fourth row. The inflow temperatures of both the CCSM3 and CCSM4 are at  $1^\circ\text{C}$  in 1900 increasing up to  $4.1^\circ\text{C}$  for the CCSM3 and  $2.6^\circ\text{C}$  for the CCSM4 by 2100. The outflows are at  $-0.1^\circ\text{C}$  in 1900 for the CCSM3 and  $0.4^\circ\text{C}$  for the CCSM4 both increasing up to  $1.7^\circ\text{C}$  by 2100. The mean ocean temperature over the Fram Strait starts at  $0.07^\circ\text{C}$  for the CCSM3 and  $0.6^\circ\text{C}$  for the CCSM4. They both increase over the whole simulation ending close to  $2^\circ\text{C}$ .

The CCSM3 and the CCSM4 simulated an increased heat flux west of Svalbard as the West Spitsbergen Current, as can be seen on the first row of figure 5.3. The intensification in the CCSM3 is more important than the CCSM4. A decrease of similar magnitude occurs over the East Greenland Current. The decrease is more apparent close to the surface but it reaches down  $800 \text{ m}$  deep in the CCSM3. In the CCSM4, the decrease spreads over a thin line close to the ocean surface.

The internal variability of the model is lower than the variations caused by the trends as can be seen on figure 5.3. Hence, the study of the average of all the simulations from one

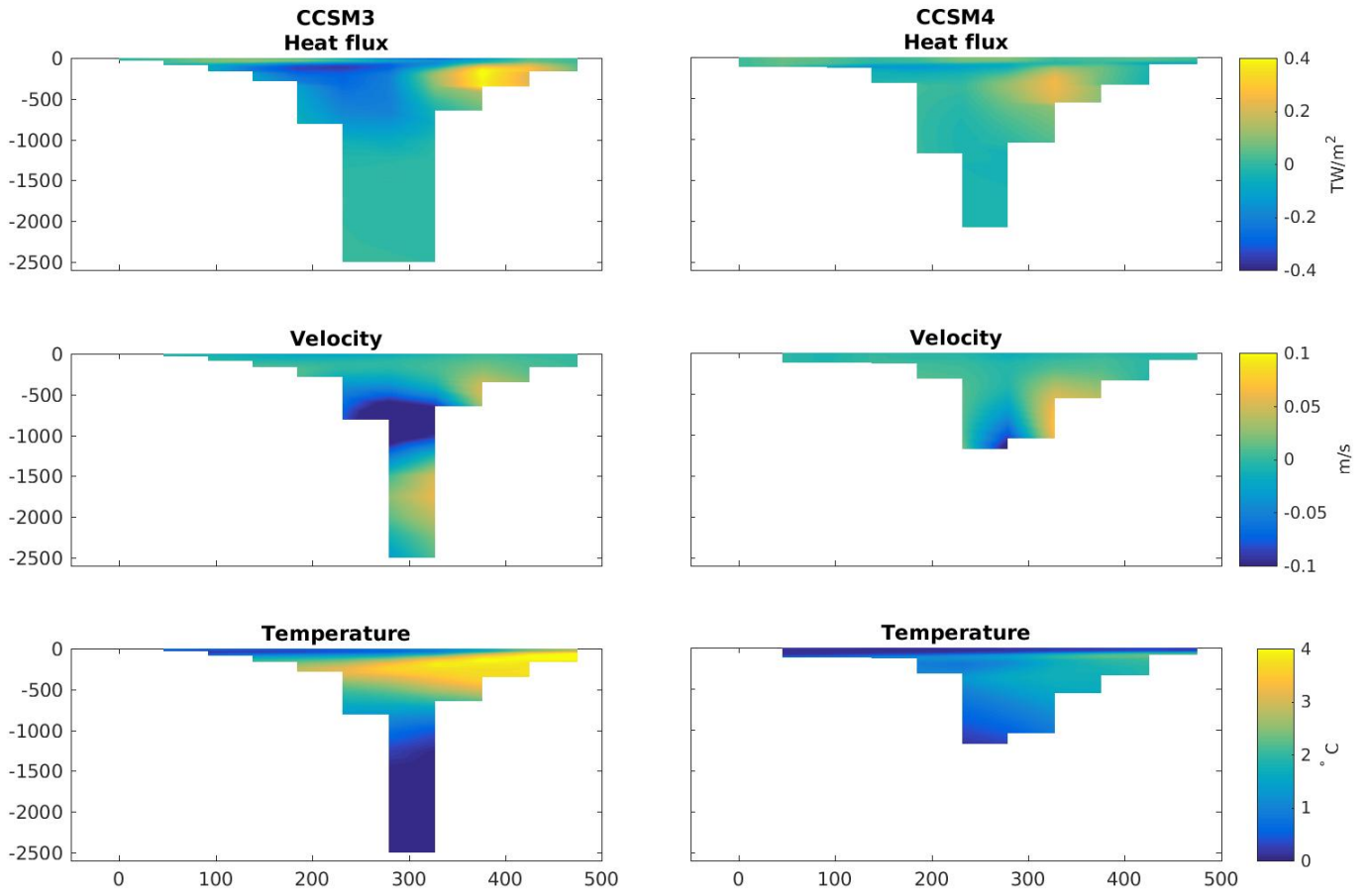


Figure 5.3: Fram Strait spatial variations in heat flux, velocity and temperature. The left column is dedicated to the CCSM3 and the right column is dedicated to the CCSM4. The variations are calculated from the difference between the 2050-2099 average and the 1900-1950 average. The depth axis is in metres and the x-axis is in kilometres.

model under one scenario represents adequately the behaviour of the model. For that reason, only the average over the simulations of a model is studied in this chapter.

Both models predict an increase in velocity over the West Spitsbergen Current and an increased outflow 1000 m deep, see the centre plots of figure 5.3. The CCSM3 simulated a second important increase in velocity 1800 m deep. Note that the gate shape presented for the heat fluxes is not the same as the velocity gate shape. The velocity field is defined on the northeast corner of the cell resulting in a narrower gate. For example, consider a two cell gate such as presented in figure 5.4. The first cell has a defined temperature and velocity. The second cell has a defined temperature but its side ends on the wall of the gate which sets the velocity to zero. The two temperature cell gate is a one velocity cell gate. Hence the different shape of the gate.

The increase in temperature is located 500 m deep close to Greenland and widening up eastward, see the bottom plots of figure 5.3. The temperature increase is more important in the CCSM3 than the CCSM4. The spatial graphs for the temperature increase were made

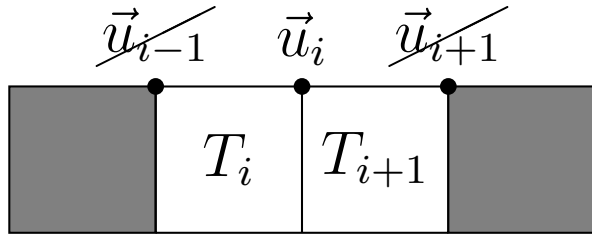


Figure 5.4: Example of a two cell Arakawa B-grid bordered by land. The orientation of the grid is on the x-y plane. The ocean temperature of the second and third cells is defined while the temperature of the first and fourth cells is undefined since they are land cell. Only the second cell has a defined velocity. The first and third cell velocity ends on land and is defined as zero. The velocity of the fourth cell is undefined since there is no water bordering it.

on the same shape as the velocity fields for an easier comparison.

The East Greenland Current of the CCSM3 intensifies greatly over the length of the simulation while the West Spitsbergen Current increases less resulting in a dramatic decrease of the value of the heat flux. The CCSM3 and the CCSM4 simulated very different outcomes for the Fram Strait.

The important features of the Fram Strait are (1) a positive heat transport during the 20<sup>th</sup> century, (2) a massive decrease in heat transport for the CCSM3 and (3) a slight increase for the CCSM4. For the CCSM3, the positive heat transport through the first simulated century arises from an outflow temperature close to zero contributing almost nothing to the heat transport. The inflow is the only source of heat transport with a positive temperature. For the CCSM4, the positive heat transport cannot be understood from the volume transport and the temperature plots. The heat transport is calculated as the volume transport multiplied by the temperature at each time step and then averaged,  $\bar{uT}$ . The volume transport and temperature presented in figure 5.2 are yearly means. The difference from both calculations,  $\bar{uT} \neq \bar{uT}$ , leads to a positive heat transport in the CCSM4. The observed massive decrease of heat transport through the Fram Strait in the CCSM3 is explained by an increased outflow of up to 2  $Sv$  with a  $2^{\circ}C$  temperature increase. The inflow of the CCSM3 is too weak in comparison. It cannot stop the decrease of heat transport even if its temperature augmented by  $3^{\circ}C$ . The slight heat transport increase in the CCSM4 comes from a more important increase of the inflow than the outflow, with their temperature increasing similarly. When comparing the simulations to the observations, the heat fluxes from the CCSM are too weak

but the total volume transport compares well to measurements.

### 5.3 Barents Sea Opening

The Barents Sea Opening starts on the east side of Svalbard, goes over Novaya Zemlya Island and over the tight opening between the Barents Sea and the Kara Sea, leading to Russian soil. The bathymetry of the Barents Sea Opening considered in this study is shown in figure 5.5. The CCSM3 cross-section of the Barents Sea Opening is very similar to the CCSM4 with the CCSM3 bathymetry being slightly deeper. The total area of the Barents Sea Opening is  $104 \text{ km}^2$  for the CCSM3 and  $114 \text{ km}^2$  for the CCSM4 with a maximum depth of  $212 \text{ m}$  and  $244 \text{ m}$  respectively.

The advective heat flux through the Barents Sea Opening of the CCSM3 starts at  $25 \text{ TW}$  and increases until 1980 at  $0.24 \text{ TW}/\text{y}$ , see the first row of figure 5.6. From 1980 up to 2070,

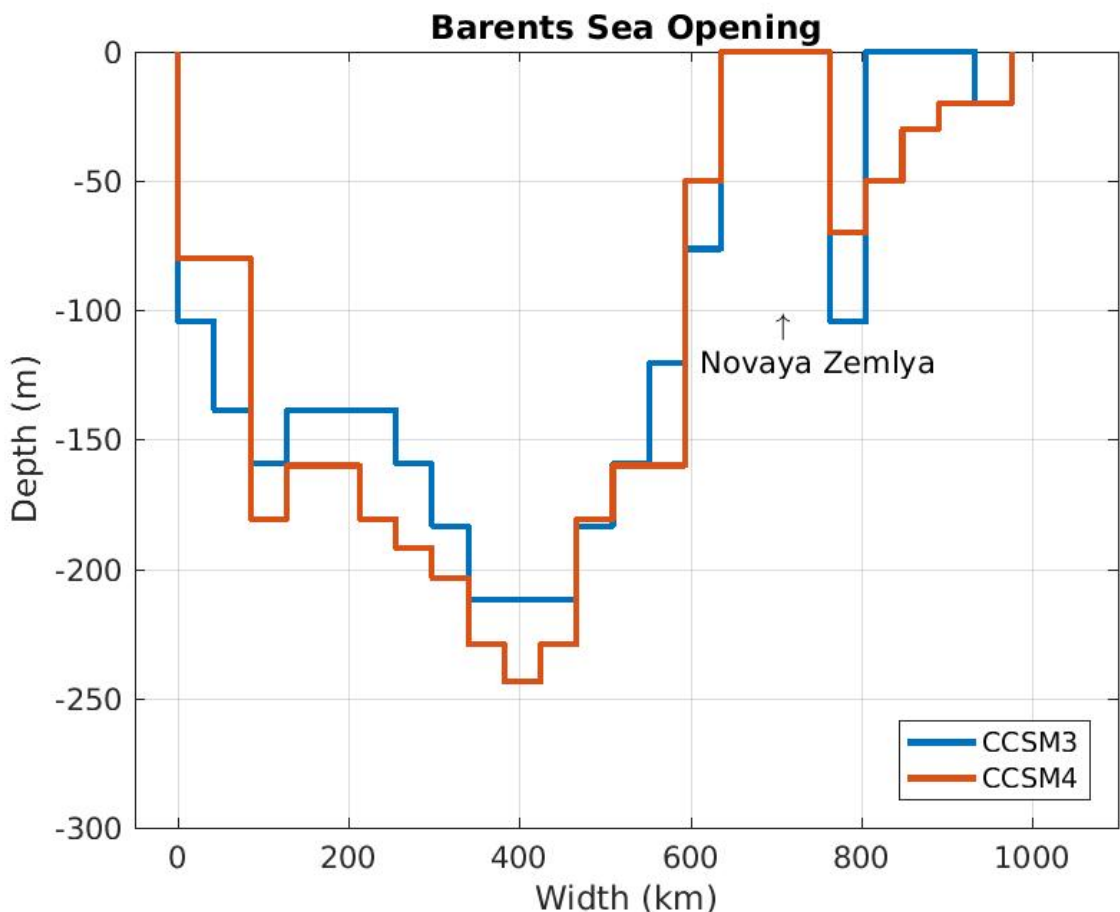


Figure 5.5: Bathymetry of the Barents Sea Opening for the CCSM version 3 in blue and version 4 in red. The location of Novaya Zemlya island is showed. On the left side (west) is Svalbard. On the right side (east) is Russia.

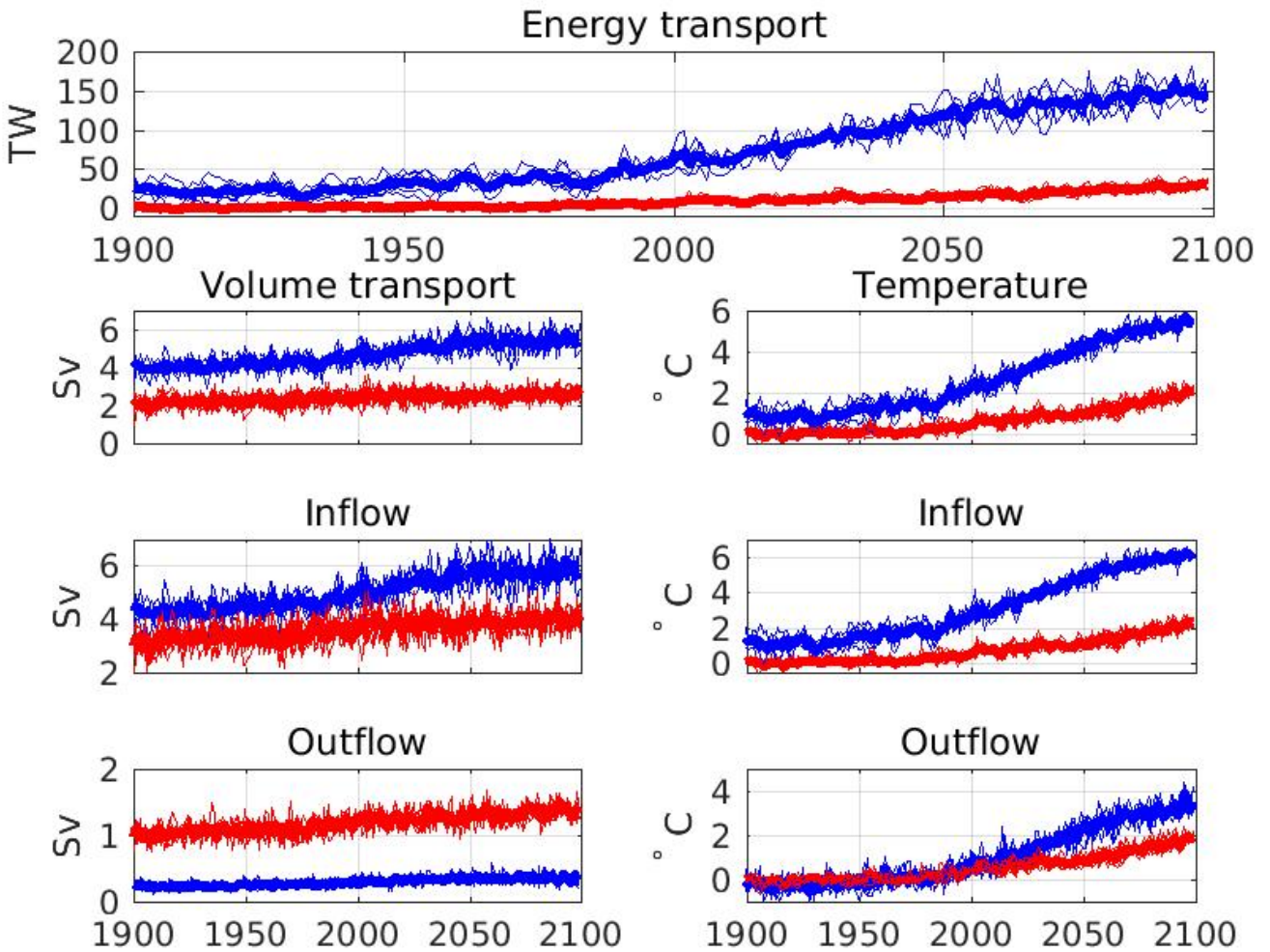


Figure 5.6: Barents Sea Opening energy transport, volume transport and temperature for the CCSM3 in blue and the CCSM4 in red. The volume transport and temperature are divided as: averaged over the full gateway (second row), averaged over the inflow (third row), averaged over the outflow (fourth row).

it increases rapidly at  $1.2 \text{ TW}/y$ . For the remaining of the century, it increases at  $0.6 \text{ TW}/y$  ending at  $147 \text{ TW}$ . The heat flux of the CCSM4 starts at zero and is stable until 1980 where it increases at a rate of  $0.2 \text{ TW}/y$  ending at  $29 \text{ TW}$ . [Skagseth et al. \(2008\)](#); [Smedsrød et al. \(2010\)](#) measured advective heat fluxes entering the Barents Sea of  $50 - 70 \text{ TW}$  between 1997-2007. The CCSM3 simulated  $60 \text{ TW}$  during the same period while the CCSM4 simulated  $8 \text{ TW}$ . The CCSM3 agrees with the observations, where the CCSM4 simulated far too weak heat transport.

The total amount of water through the Barents Sea opening starts at  $4.1 \text{ Sv}$  and ends at  $5.4 \text{ Sv}$  for the CCSM3 compared to  $2.1 \text{ Sv}$  and  $2.6 \text{ Sv}$  for the CCSM4, as can be seen on the left plot of the second row of figure 5.6. [Skagseth et al. \(2008\)](#) and [Smedsrød et al. \(2010\)](#) observed a mean volume transport through the Barents Sea Opening of  $2 \text{ Sv}/y$  between 1997-2007. During the 1997-2007 period, the total volume transport of the CCSM3 was of  $4.7 \text{ Sv}$

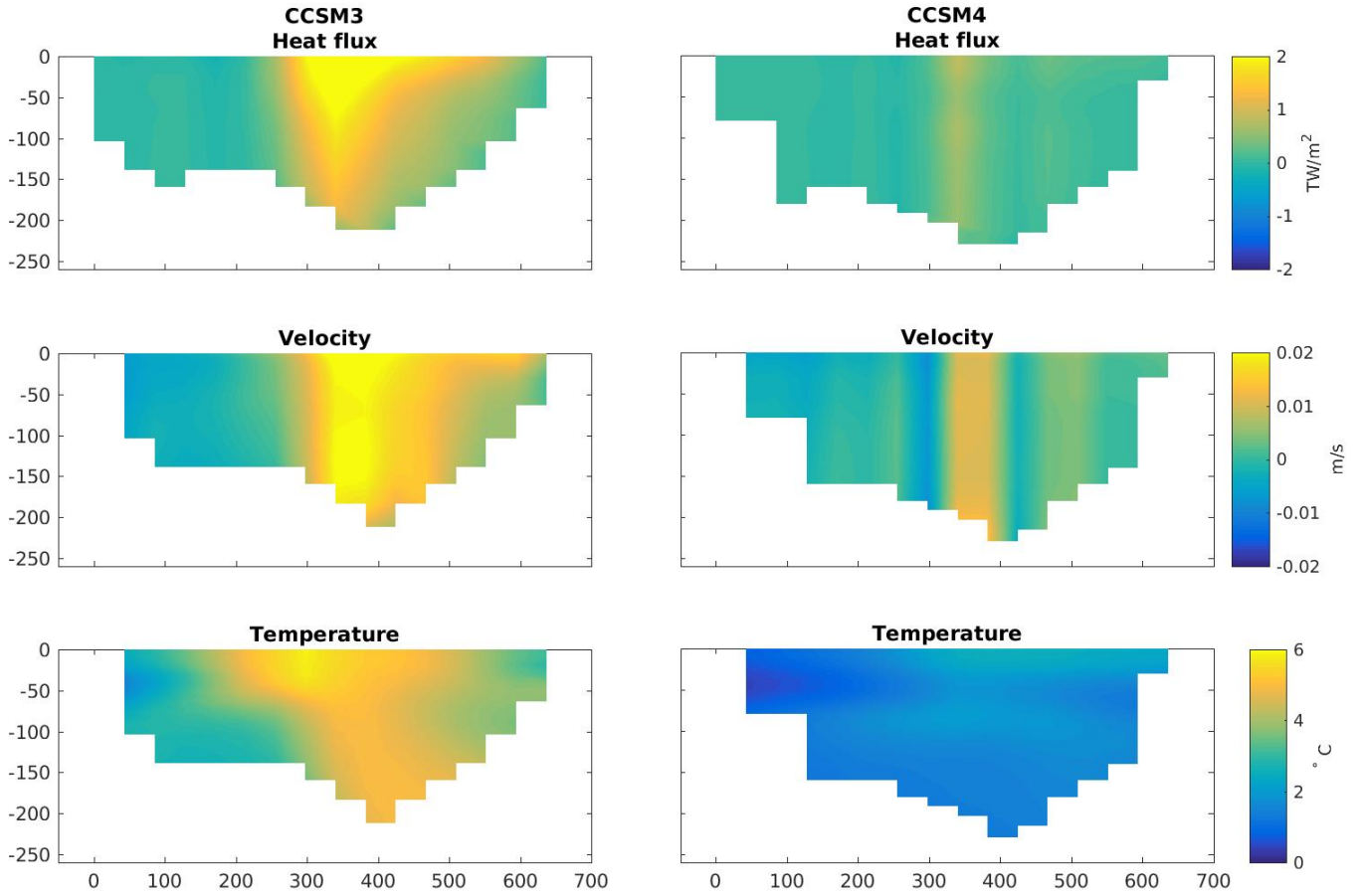


Figure 5.7: Barents Sea Opening spatial variations in heat flux, velocity and temperature. The left column is dedicated to the CCSM3 and the right column is dedicated to the CCSM4. The variations are calculated from the difference between the 2050-2099 average and the 1900-1950 average. The depth axis is in metres and the x-axis is in kilometres. Note that the colour axis changed from figure 5.3

and the CCSM4 volume transport was of  $2.5\text{ Sv}$ . The volume transport of the CCSM3 is too large compared to measurements. The CCSM4 volume transport is more in line with measurements. Note that the moorings which provided the observations are not located at the same place as the Barents Sea Opening defined in this thesis. The moorings link Svalbard directly to Norway while the gateway defined here goes to Russia. This difference could cause a larger than expected difference between the simulations and the observations.

The volume of water entering the Arctic Ocean through the Barents Sea Opening increases steadily for both the CCSM3 and the CCSM4, see the left plot of the third row of figure 5.6. It starts at  $4.3\text{ Sv}$  for the CCSM3 and increases up to  $5.8\text{ Sv}$  by 2100. For the CCSM4, it starts at  $3.1\text{ Sv}$  and ends at  $4\text{ Sv}$ . The outflow of the CCSM3 through the Barents Sea Opening is negligible compared to the inflow, see the left plot of the fourth row of figure 5.6. It starts at  $0.25\text{ Sv}$  in 1900 and ends at  $0.33\text{ Sv}$  in 2100. The outflow of the CCSM4 is more important starting at  $1\text{ Sv}$  and ending at  $1.3\text{ Sv}$ .

The temperature increases exponentially over the Barents Sea Opening, as can be seen

on the right plots from the second to the fourth row of figure 5.6. The temperature of the inflow for the CCSM3 starts at  $1.3^{\circ}\text{C}$  and increases up to  $6.1^{\circ}\text{C}$ . The outflow temperature is cooler at  $-0.2^{\circ}\text{C}$  in 1900 increasing to  $3.5^{\circ}\text{C}$  in 2100. The CCSM4 inflow temperature starts at  $0.1^{\circ}\text{C}$  and increases up to  $2.2^{\circ}\text{C}$  by 2100. Its outflow temperature starts at  $0^{\circ}\text{C}$  and increase up to  $1.8^{\circ}\text{C}$ . The mean temperature of the Barents Sea opening starts at  $1^{\circ}\text{C}$  and  $0^{\circ}\text{C}$  and increases up to  $5.5^{\circ}\text{C}$  and  $2^{\circ}\text{C}$  respectively for the CCSM3 and the CCSM4.

The CCSM3 heat transport though the Barents Sea opening increases mainly at its centre expanding to the east, see the top row of figure 5.7. The CCSM4 increase in heat transport is located over a thin vertical line at the centre of the opening. The heat flux increase seen in the CCSM3 is more important than the CCSM4. The velocity field increase is centered over the same region as the heat transport but spans a wider area. The increase in velocity is weak though with changes of the order of  $0.01\text{ m/s}$  over 200 years. The temperature of the Barents Sea Opening increases over the whole gateway. The highest increase occurs at the centre of the opening over the first  $50\text{ m}$ . The temperature increase of the CCSM3 goes over  $6^{\circ}\text{C}$  while CCSM4 increase in temperature caps at  $3^{\circ}\text{C}$ .

The most notable feature of the Barents Sea Opening is the considerable heat flux increase through the Barents Sea Opening predicted by the CCSM3 compared to the more modest increase of the CCSM4. The heat transport increase observed in the CCSM3 is caused by an important inflow increase coupled with an inconsequential outflow. The inflow increase is less important in the CCSM4 and its outflow is more important. The resultant is an increasing heat transport but not as large as seen in the CCSM3. The CCSM3 heat transport agrees with observations but its volume transport is too strong. On the other hand, the CCSM4 volume transport agrees with observations but its heat transport is too weak.

## 5.4 Canadian Arctic Archipelago

The bathymetry of the Canadian Arctic Archipelago along the line defined in figure 3.1 is presented in figure 5.8. It consists of four compact gateway: 1) Amundsen Gulf close to the Beaufort Sea, 2) M'Clure Strait, 3) The body of water between Melville Island and Ellesmere Island, 4) Nares Strait. The bathymetry of the CCSM4 reaches deeper than the CCSM3

with respective depth of 338 m and 212 m. On two openings, the CCSM3 is wider than the CCSM4. On the two other openings, the width is the same for both the CCSM3 and CCSM4. The resulting area,  $64 \text{ km}^2$ , is the same for both models. When it comes to observations of the gateways across the Canadian Arctic Archipelago, each gateway is studied separately by different teams of researchers. The observations are scarce and limited. None calculated the heat transport. Hence, we cannot provide any comparisons with observations. The openings of the Canadian Arctic Archipelago are narrow and when spatially plot, most of the openings is lost over the velocity grid. Also, the spatial variations are very modest. Therefore, there will be no spatial variation study of heat fluxes, velocity and temperature.

The heat flux through the Canadian Arctic Archipelago for the SRES A1B simulations starts at  $2.2 \text{ TW}$  and stays stable until 2000 where it decreases at a rate of  $-0.015 \text{ TW/y}$  ending at  $0.76 \text{ TW}$ , see the first row of figure 5.9. The CCSM4 exhibits the same two phases. Its heat flux starts at  $10.5 \text{ TW}$  and is stable for 100 years where it decreases in magnitude

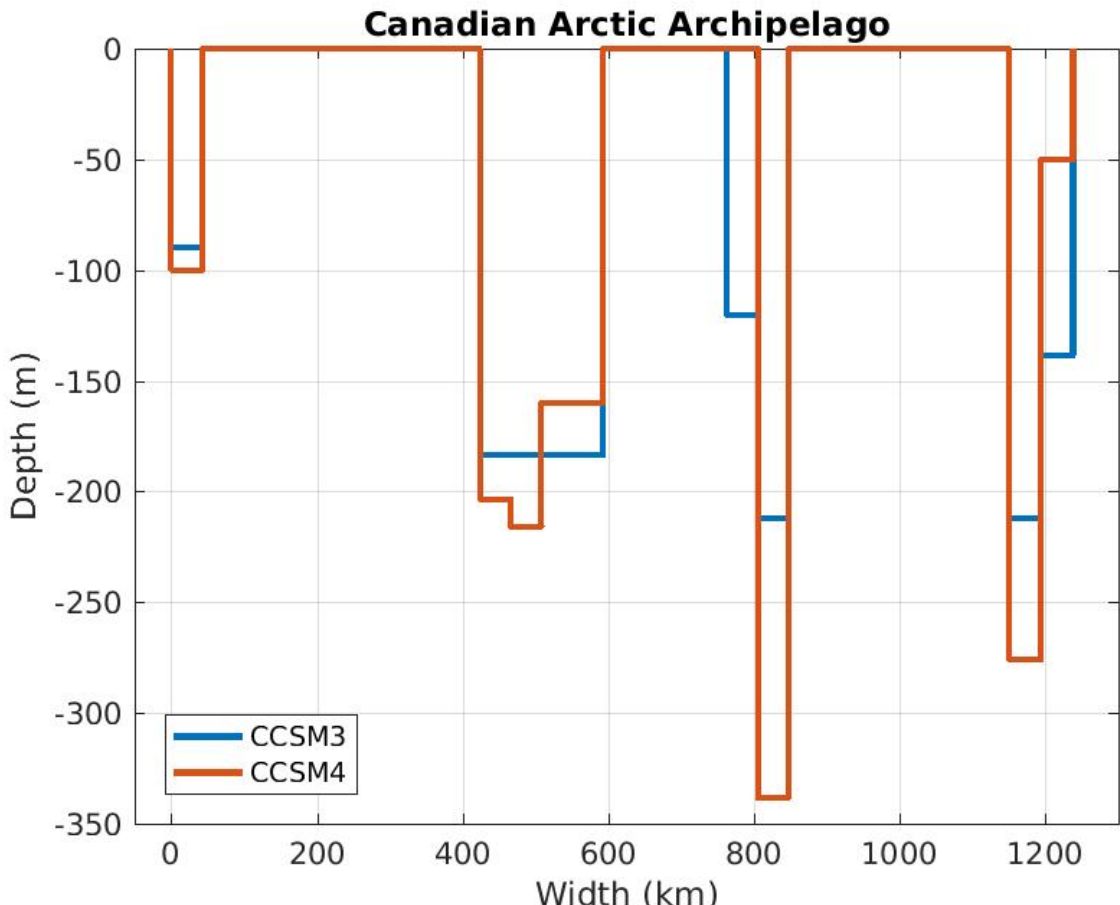


Figure 5.8: Bathymetry of the Canadian Arctic Archipelago along the cross-section defined in figure 3.1. It is completely located inside Canadian territory.

at a rate of  $-0.024\text{ TW}/y$  ending at  $7.7\text{ TW}$ .

The volume transport of the Canadian Arctic Archipelago is characterized by an outflow with an inconsequential inflow, see the left plots from the second to the fourth row of figure 5.9. The total volume of water through the Canadian Arctic Archipelago for the CCSM3 starts at  $-0.38\text{ Sv}$  in 1900 and increases in strength linearly up to  $-0.46\text{ Sv}$  by 2100. For the CCSM4, it starts at  $-1.8\text{ Sv}$  in 1900 and decreases in strength linearly down to  $-1.6\text{ Sv}$  by 2100. The reason for the higher outflow in the CCSM4 is because the Nares Strait is now connected to the Atlantic Ocean. It is a new feature of the ocean component of the CCSM4.

The mean temperature and the outflow temperature are almost identical due to the extremely weak inflow, see the right plots from the second to the fourth row of figure 5.9. The mean temperature of the inflow starts at  $-1.2^{\circ}\text{C}$  in 1900 and increases exponentially ending

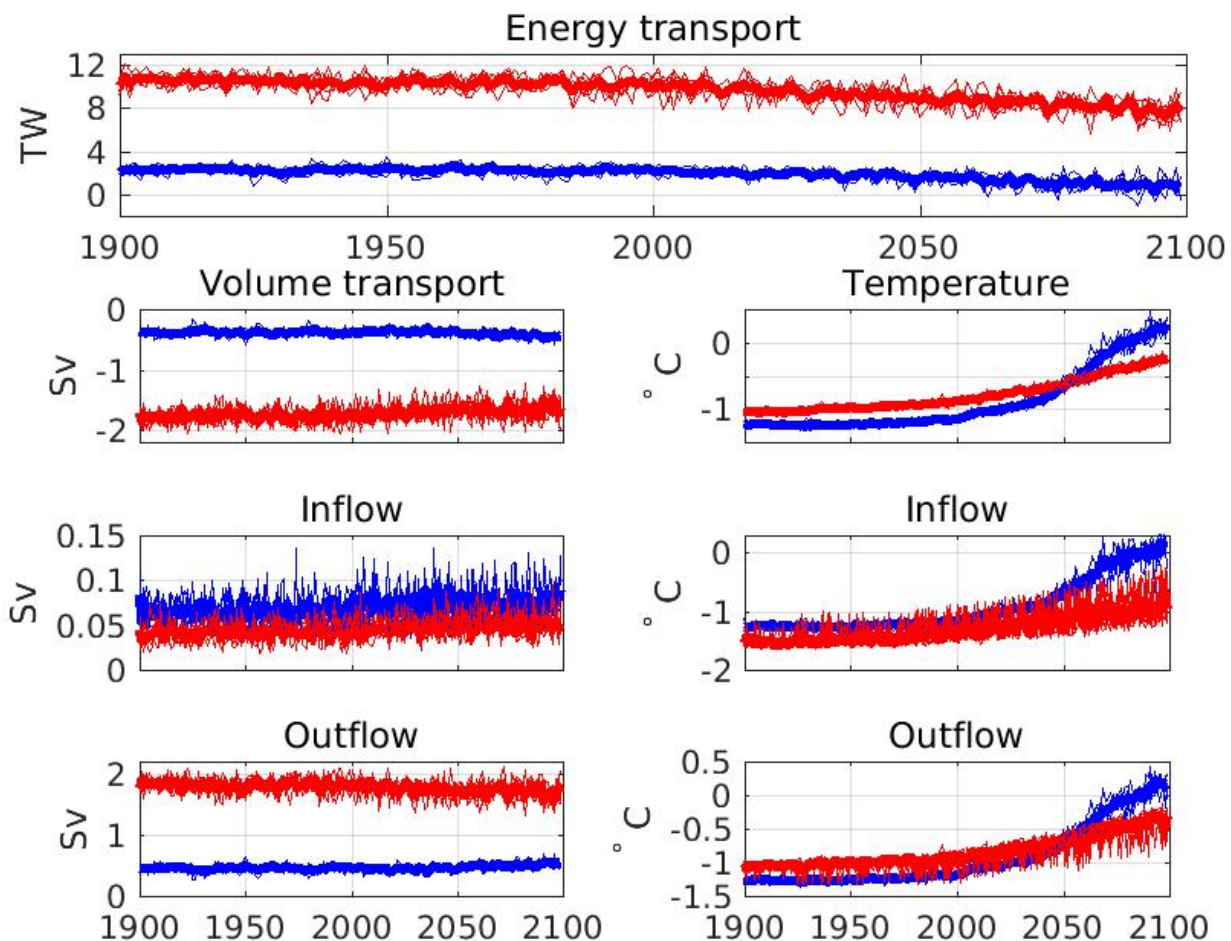


Figure 5.9: Canadian Arctic Archipelago energy transport, volume transport and temperature for the CCSM3 in blue and the CCSM4 in red. The volume transport and temperature are divided as: averaged over the full gateway (second row), averaged over the inflow (third row), averaged over the outflow (fourth row).

at  $0.2^{\circ}C$  in 2100 for the CCSM3. The CCSM4 Canadian Arctic Archipelago temperature starts at  $-1^{\circ}C$  in 1900 and increases exponentially ending at  $-0.25^{\circ}C$  in 2100.

The positive heat transport through the Canadian Arctic Archipelago comes from the product of a negative velocity (outflow) and a negative temperature. By the end of the 21<sup>st</sup> century, the CCSM3 temperature goes from subzero to positive resulting in several years with negative heat fluxes over the different simulations of the CCSM3. The outflow of the CCSM4 slightly decreases in strength. Its temperature increases getting closer to zero but staying negative. Both changes contribute to the CCSM4 decrease in heat transport magnitude through the Canadian Arctic Archipelago.

## 5.5 Bering Strait

The Bering Strait is the smallest gate to the Arctic Ocean. Its bathymetry is shown in figure 5.10. It links Russia to Alaska. The Bering Strait of the CCSM3 has an area of  $8\text{ km}^2$  which is twice the area of the CCSM4 with  $4\text{ km}^2$ . The CCSM3 is  $125\text{ km}$  wider and  $11\text{ m}$  deeper than the CCSM4. The CCSM3 and the CCSM4 have a wider than observed Bering Strait which is approximated at  $85\text{ km}$  wide ([Beszczynska-Moller et al., 2011](#)). The modelled Bering Straits are not deep enough. The Bering Strait is  $50\text{ m}$  deep. The CCSM3 is far too wide with an acceptable depth. The CCSM4 is closer to reality in terms of the width but is not deep enough with a depth of  $30\text{ m}$ . The Bering Strait spans over such a small number of model cells that most spatial variations are deemed identical. No spatial figure are presented for that reason.

The advective heat flux through the Bering Strait of the SRES A1B from the CCSM3 starts at  $-2.1\text{ TW}$  and increases at  $0.014\text{ TW}/y$  until 2000 where it accelerates at  $0.07\text{ TW}/y$  ending at  $5.1\text{ TW}$ , see the first row of figure 5.11. The CCSM4 follows the CCSM3 with higher values. It starts at  $-0.94\text{ TW}$  and increases at  $0.03\text{ TW}/y$  for 100 years. For the remaining 100 years, it increases at  $0.09\text{ TW}/y$  ending at  $10\text{ TW}$ . Both versions of the CCSM present an increase in heat flux over the whole region. [Woodgate et al. \(2010\)](#) measured a heat flux of  $10 - 20\text{ TW}$  between 1998 and 2007. The CCSM3 simulated  $-0.8\text{ TW}$  during the same period and the CCSM4  $2.4\text{ TW}$ . They are both too low to agree with observations.

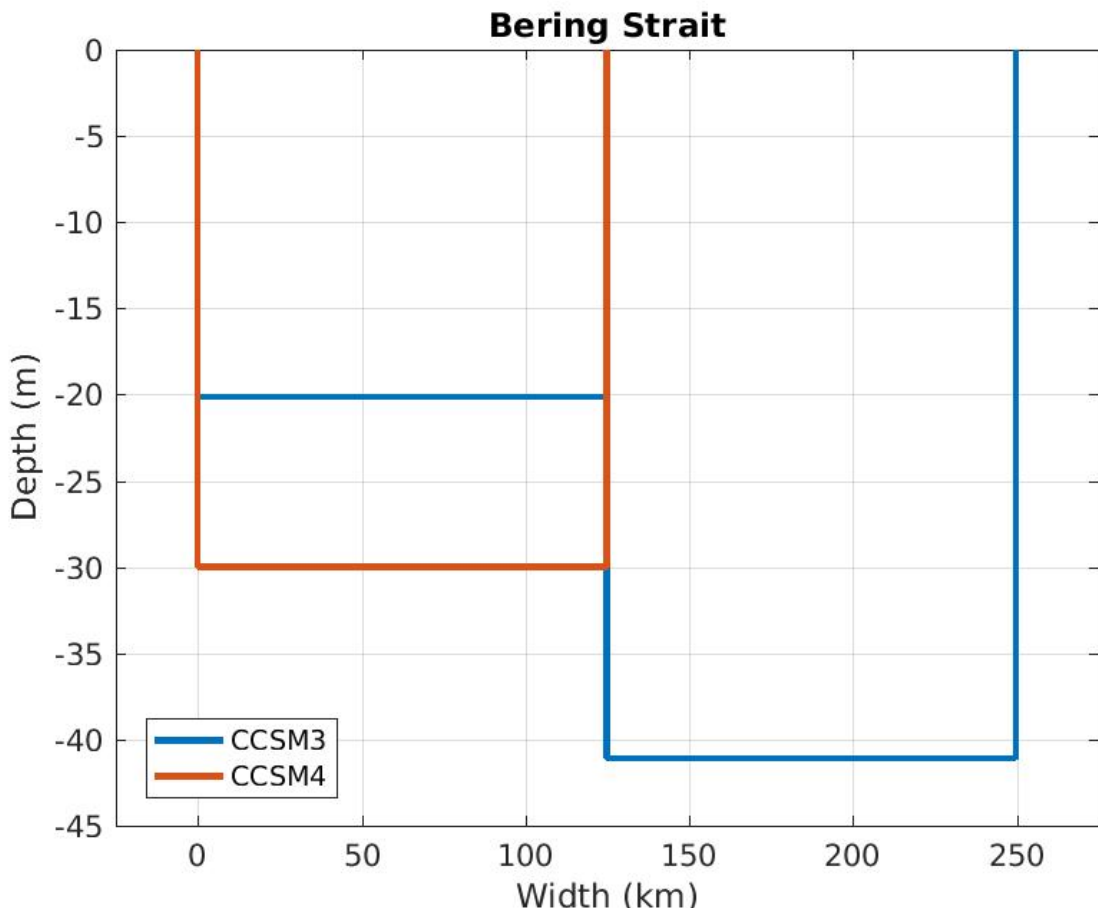


Figure 5.10: Bathymetry of the Bering Strait for the CCSM3 in blue and CCSM4 in red. On the right side (west) of the strait is Russia. On the left side (east) of the strait is Alaska, United States of America.

There is no outflow over the Bering Strait. The CCSM3 inflow is stable during the 20<sup>th</sup> century at 1  $Sv$ , see the second row of figure 5.11. It then decreases steadily over the 21<sup>st</sup> century ending at 0.7. The CCSM4 inflow through the Bering Strait is stable over the full simulation at 1  $Sv$ . [Woodgate et al. \(2010\)](#) observed an inflow of  $0.8 \pm 0.2 S v$  between 1998-2007. Both the CCSM3 and the CCSM4 agrees with the observed inflow for the Bering Strait.

The temperature of the CCSM3 over the Bering Strait is modestly increasing over the 20<sup>th</sup> century starting at  $-0.9^{\circ}C$  and ending at  $-0.75^{\circ}C$ , see the third row of figure 5.11. During the 21<sup>st</sup> century, it increases more rapidly ending at  $1^{\circ}C$  by 2100. The CCSM4 has the same two phases. The temperature of the Bering Strait for the CCSM4 starts at  $-0.3^{\circ}C$  in 1900, increases slowly up to  $0.4^{\circ}C$  in 2000 and then increases rapidly up to  $2.3^{\circ}C$  by 2100.

The CCSM3 and CCSM4 exhibits the same characteristics over the Bering Strait. The modelled shapes are not representative of the measurements. The increase in heat transport

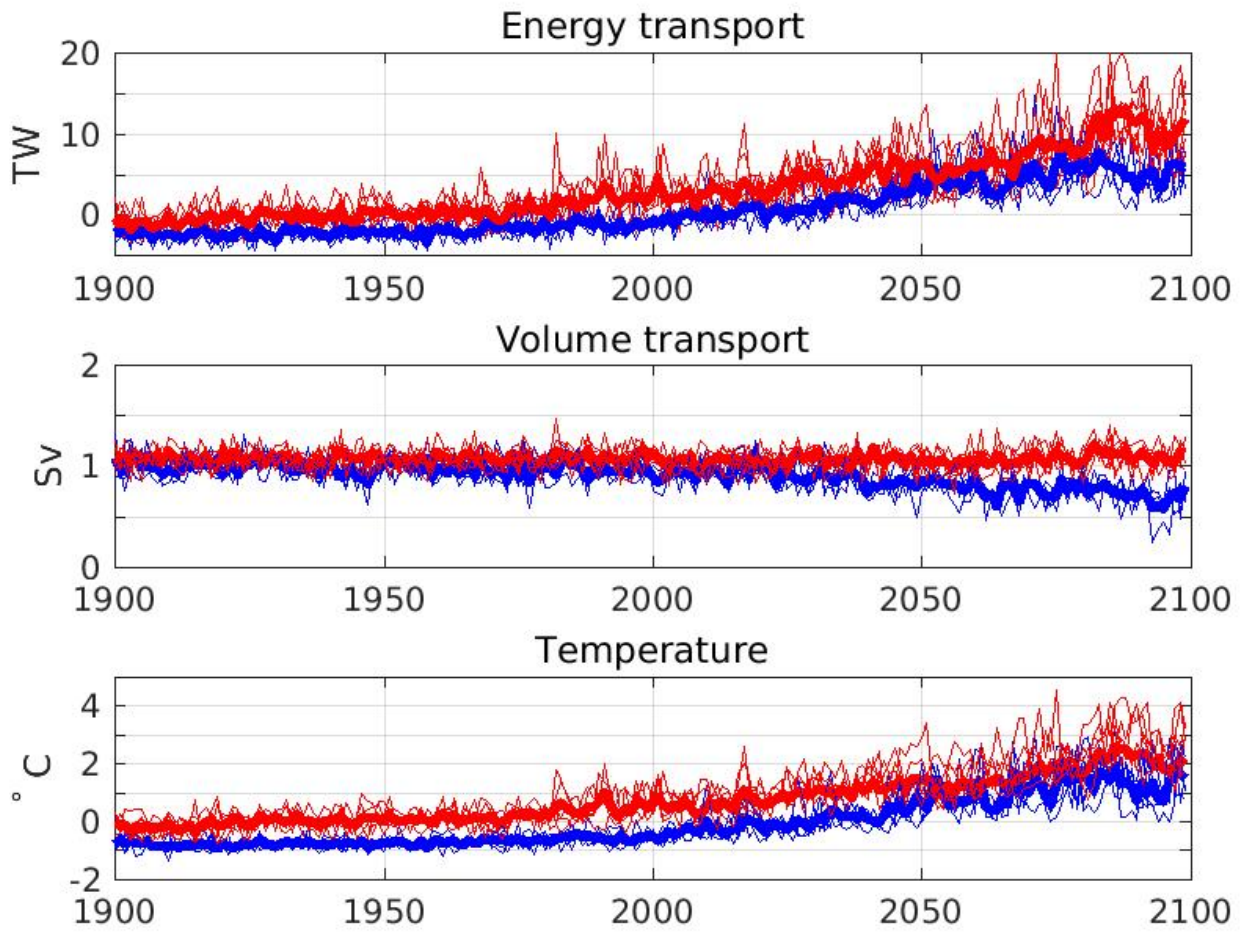


Figure 5.11: Bering Strait energy transport, volume transport and temperature. Blue) CCSM3. Red) CCSM4.

through the Bering Strait is explained by the increase in temperature. The loss of inflow is not enough to balance it. The heat fluxes disagree strongly with the observations being too weak but the volume transports agree.

## 5.6 Discussion

The heat transported through the Barents Sea Opening (BSO) is dominating all the other gateways of the Arctic Ocean for the CCSM3, figure 5.12. It coincides with the located melt observed in March 2099 in the Barents Sea in all the SRES A1B simulations of the CCSM3, figure 3.5. The heat transport through the Fram Strait has a small impact on the total budget. The contribution from the Bering Strait and the Canadian Arctic Archipelago are negligible. Even though the heat transport through the Bering Strait is inconsequential compared to the Barents Sea Opening, since it is located at the surface, its impact can be felt rapidly and strongly by the sea ice. It has left its mark on simulations a, b.ES01 and

e, figure 3.5. Woodgate et al. (2010) believes that the minimum sea extent recorded in 2007 was partly caused by an increase in heat transport through the Bering Strait weakening the sea ice in the vicinity.

In the case of the simulations under the RCP 6.0 scenario of the CCSM4, the total heat transported to the Arctic Ocean is divided into four commensurate sources. The Barents Sea opening is the one increasing the most just as the CCSM3. The only decreasing heat flux comes from the Canadian Arctic Archipelago decreasing mildly over the full simulation.

As stated in the introduction of this chapter, the warming of the Arctic takes several forms. The simulated heat transported to the Arctic Ocean by the CCSM3 SRES A1B is more aggressive than the CCSM4 RCP 6.0. In 1900, the total heat transported to the Arctic Ocean was of  $35\text{ TW}$  for the CCSM3 and  $19\text{ TW}$  for the CCSM4. By 2100, it rose up to  $130\text{ TW}$  for the CCSM3 and  $60\text{ TW}$  for the CCSM4.

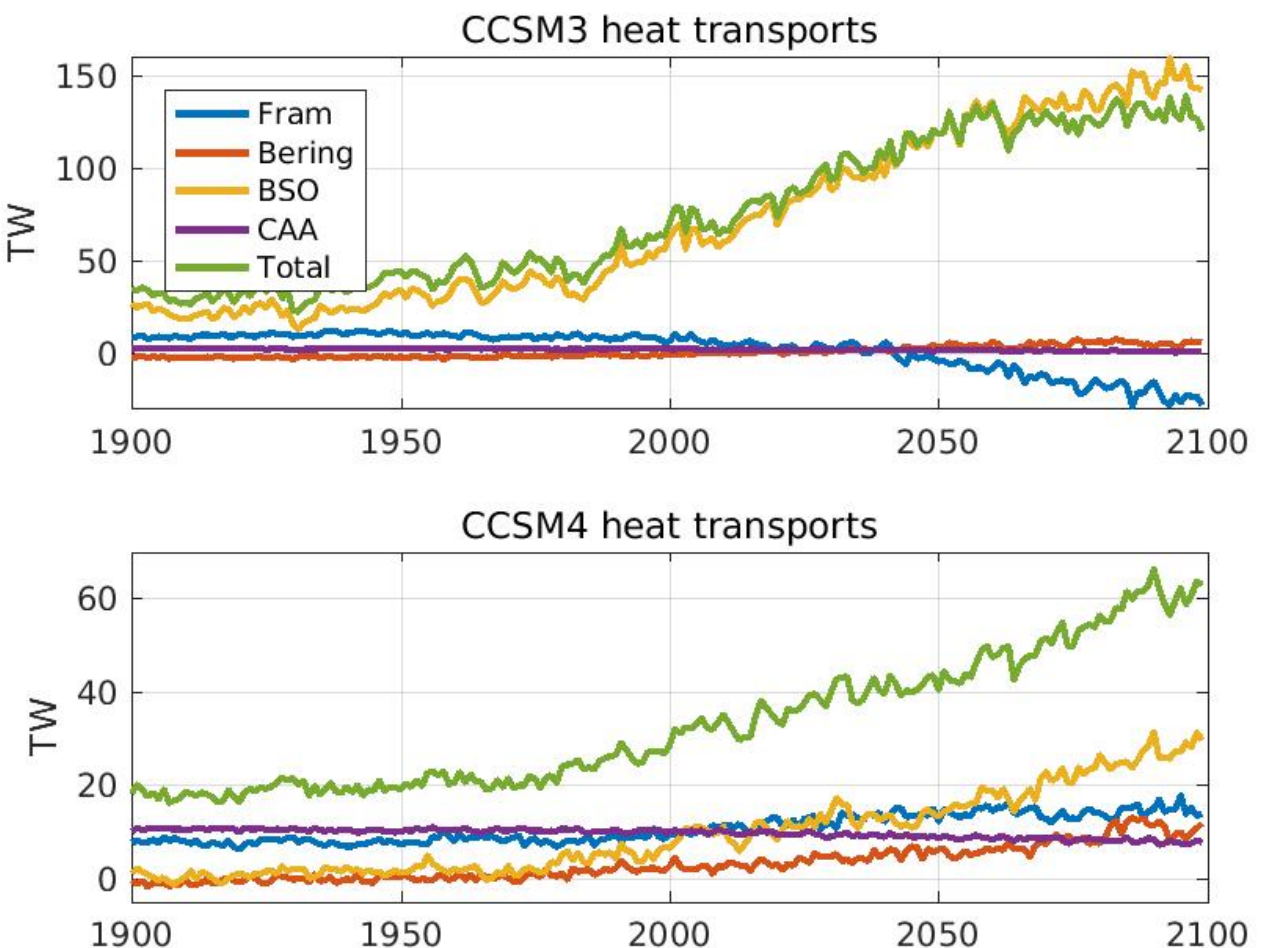


Figure 5.12: Heat transport through the gateways of the Arctic Ocean. Top) CCSM3. Bottom) CCSM4.

The volume transport budget closes satisfactorily in both CCSM3 and CCSM4. The CCSM ocean component treats the excess or loss of volume transport as sea level variation. The modest variations of the volume budget elevate or lower the mean sea level of the Arctic Ocean. The volume of water entering through the Barents Sea Opening in the CCSM3 is completely evacuated through the Fram Strait, figure 5.13. For the CCSM4, approximately one third of the water volume enters through the Bering Strait and two thirds through the Barents Sea Opening. Half of this water exits through the Fram Strait and the other half through the Canadian Arctic Archipelago.

The CCSM does not reproduce accurately the heat transport through the gateways of the Arctic Ocean, as presented in table 5.1. The volume transport simulated by the CCSM4 agrees better than the one by the CCSM3. While the CCSM4 volume transport agrees with observations for the Fram Strait, the Barents Sea Opening and the Bering Strait, the

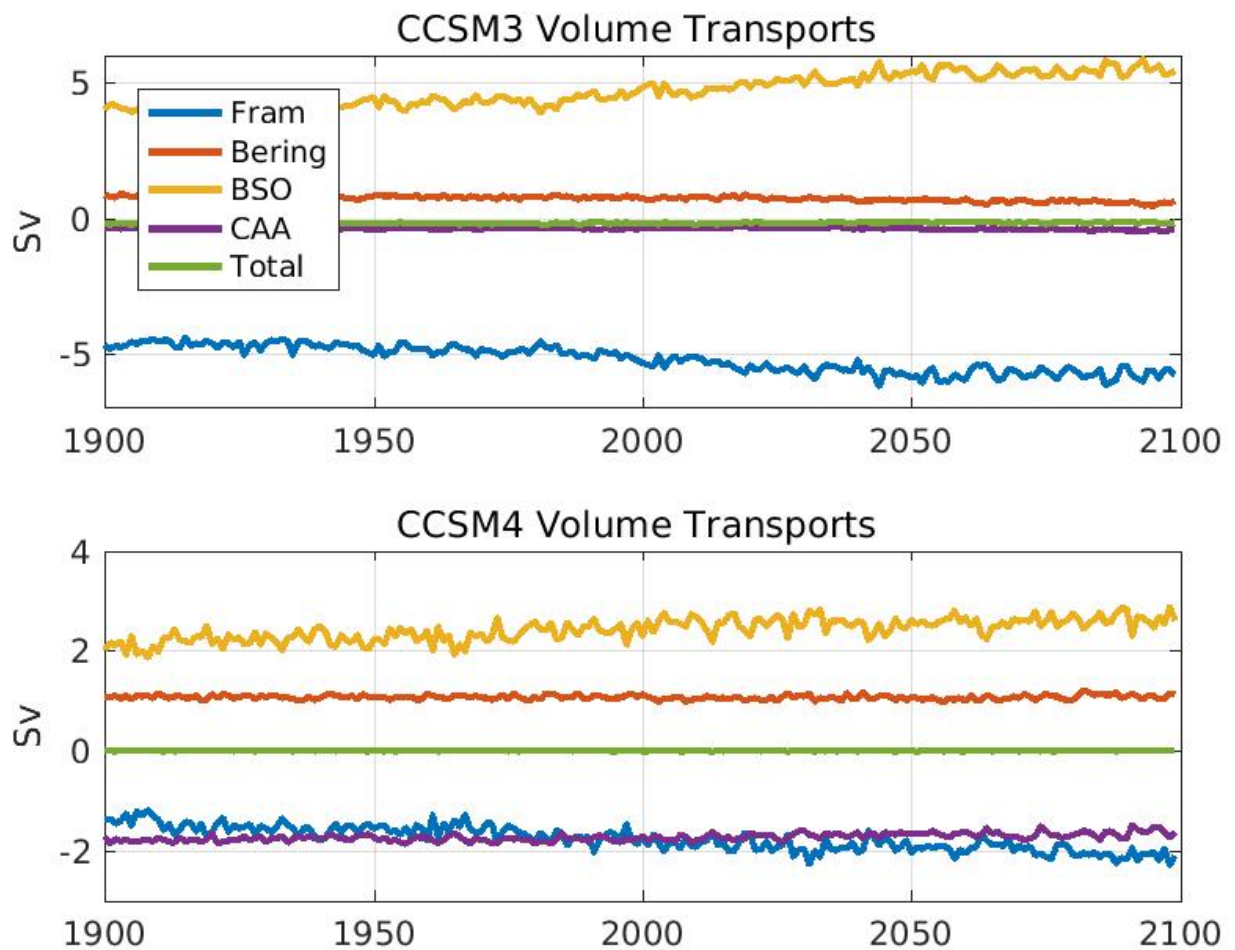


Figure 5.13: Volume transport through the gateways of the Arctic Ocean. Top) CCSM3. Bottom) CCSM4.

Heat transport				
	Years	Obs	CCSM3	CCSM4
Fram	1997-2009	$36 \pm 6 TW$	<b><math>8 TW</math></b>	<b><math>9 TW</math></b>
BSO	1997-2007	$50 - 70 TW$	$60 TW$	<b><math>8 TW</math></b>
CAA	-	-	-	-
Bering	1998-2007	$10 - 20 TW$	<b><math>-0.8 TW</math></b>	<b><math>2.4 TW</math></b>

Volume transport				
	Years	Obs	CCSM3	CCSM4
Fram	1997-2007	$-2.0 \pm 2.7 Sv$	<b><math>-5 Sv</math></b>	$-1.8 Sv$
BSO	1997-2007	$2 Sv$	<b><math>4.7 Sv</math></b>	$2.5 Sv$
CAA	-	-	-	-
Bering	1997-2007	$0.8 \pm -0.2 Sv$	$0.8 Sv$	$0.9 Sv$

Table 5.1: Heat and volume transport through the gateways of the Arctic Ocean from observations, simulated by the CCSM3 SRES A1B and simulated by the CCSM4 RCP 6.0 scenario. The gateways of the Arctic Ocean are: Fram Strait, Barents Sea Opening (BSO), Canadian Arctic Archipelago (CAA) and Bering Strait. The highlighted values do not agree with the observations.

CCSM3 volume transport agrees only for the Bering Strait. The heat transport worsens through. Since the heat transport is calculated from the product of the volume flux and the gateway temperature, and the volume transport from the CCSM4 agrees with observations, the temperature field must be inaccurate. It is known from [Jahn et al. \(2012\)](#) that the CCSM4 Arctic Ocean temperature profile is too high compared to observations below a depth of one kilometre. On a minor note, the bathymetry of the gateways could be more realistic.

## 6 Conclusion

This thesis studied the thermal interactions between the Arctic sea ice and the Arctic Ocean. In addition, the sources of ocean heat influencing the surface layer of the Arctic Ocean has been analyzed. Chapter 3 investigated the evolution of the sea ice volume for the six simulations of the CCSM3 under the SRES A1B described in [Holland et al. \(2006b\)](#). Sea ice volume starts decreasing in 1950 while the sea ice extent decrease starts in the 21<sup>st</sup> century; 40% of the sea ice volume has been lost between 1950 and 2000 compared to only 8% of the sea ice extent. The sea ice volume decreases exponentially in function of the extra forcing from the future emission scenario with a half life of  $1 W/m^2$ . Half of the remaining volume will be lost when the extra forcing increases of  $1 W/m^2$ . The transport of sea ice volume out of the Arctic Ocean happens almost entirely through the Fram Strait. In 1900,  $4 \cdot 1000 km^3/y$  exits the Arctic Ocean compared to  $1000 km^3/y$  in 2100. The most important and most growing thermodynamic process is basal melt. It is determined by the amount of heat from the ocean transferred to the sea ice. The amount of heat transferred is  $30 W/m^2$  by 1900 and ascend up to  $130 W/m^2$  by 2100. This utmost increase is caused by the exponential increase in surface temperature. The surface temperature starts at  $-1.5^\circ C$  in 1900 ending at  $0^\circ C$  in 2100. The rapid loss of September sea ice extent described in [Holland et al. \(2006b\)](#) cannot be explained solely by the bottom melt though. All the other processes are important and cannot be neglected.

Chapter 4 investigated all the heat sources influencing the Arctic Ocean surface temperature for the CCSM3. Unfortunately, the vertical heat diffusion is not output. It is possible to evaluate it as a residual of the temperature change and the other heat sources. To ascertain the inclusion of all the other heat sources, closing a column budget is necessary. The column budget has zero vertical diffusion at the ocean's surface and at the ocean's floor. This exercise leads to an error of  $\pm 2 W/m^2$  over the Global Ocean,  $\pm 3 W/m^2$  over the Arctic Ocean and  $\pm 150 W/m^2$  over the columns. The Arctic Ocean being well stratified, only weak diffusive fluxes, less than  $1 W/m^2$ , are expected ([Timmermans et al., 2008](#)). An error or  $\pm 150 W/m^2$  is unacceptable. The error can be lowered using instantaneous temperature snapshots for the temporal derivative instead of monthly averaged temperature fields. The CCSM3 does not

provide such fields but the CCSM4 does. The CCSM4 temperature-heat budget closes up to  $\pm 0.4 \text{ W/m}^2$  over the Global Ocean and the Arctic Ocean. Even if the Global and Arctic Oceans' budget error improved appreciably, the heat budget of the columns has an error of  $\pm 50 \text{ W/m}^2$ . This unacceptable error does not bring enough confidence in our calculation to trust the heat budget presented in this thesis. Verifying every term in the CCSM code would bring the most assertive confidence in the heat budget. Disappointingly, even if shedding some light on several heat sources, it did not point to any refinement of the temperature-heat budget calculation.

Instead of examining all the heat sources as a whole, chapter 5 scrutinize only one source: the advective heat fluxes through the gateways of the Arctic Ocean. The gateways include the Fram Strait, the Barents Sea opening, the Canadian Arctic Archipelago and the Bering Strait. There are considerable discrepancies between the CCSM3 and CCSM4 forecasts. Over the 20<sup>th</sup> century, the heat transports through the Fram Strait for the CCSM3 and CCSM4 are similar averaging at 9 TW yearly. They diverge over the 21<sup>st</sup> with the CCSM3 decreasing down to  $-25 \text{ TW}$  and the CCSM4 increasing up to 15 TW. Through the Barents Sea Opening, the heat transport increased from 25 TW up to 150 TW for the CCSM3 while it increased from 0 TW yearly up to 30 TW for the CCSM4. Over the Canadian Arctic Archipelago, the heat transport decreases modestly for both versions of the CCSM. The CCSM3 predicts a heat transport of 2 TW in 1900 and 1 TW in 2100 while the CCSM4 predicts 10 TW in 1900 and 8 TW in 2100. The results for the Bering Strait are similar over the versions 3 and 4 of the CCSM starting close to  $-1 \text{ TW}$  in 1900 and ending at 8 TW in 2100. Advective heat fluxes are elusive and different calculations could bring different results. Their impact on warming or cooling the Arctic Ocean can only be ascertained by doing a full budget over all the gates. In both versions of the CCSM, the total heat transport is positive, warming the Arctic Ocean. The CCSM3 total heat transport is dominated by the Barents Sea Opening. It starts at 35 TW and ends at 130 TW. The CCSM4 total heat transport receives notable contributions from all the gateways. It begins at 19 TW in 1900 and stops at 60 TW. The advective heat transport is twice more important in the CCSM3 than in the CCSM4. The CCSM heat transport forecasts do not agree well with observations.

The exchange of heat between the Arctic Ocean and its sea ice is a complex process. I am proposing five ideas to improve our knowledge of the Arctic, its sea ice and its ocean:

1. High resolution simulations focussing on the junction between fluid and solid. This type of simulation would enhance our understanding of how heat and kinetic energy is transferred between the Arctic Ocean and the Arctic sea ice.
2. A clear calculation reconstructing the CCSM temperature-heat equation. It seems the standard output does not offer the adequate variables to do so. The temperature is core in the many transformations the Arctic undergoes. It is mandatory to access the sources of the temperature increase if we want to understand the future of the Arctic.
3. Climate model simulations with controlled ocean circulation and heat transport. The impact of the heat transport through the gates of the Arctic Ocean on the sea ice is a challenging topic. Only the first few ocean layers have the possibility to melt sea ice. It would be important to understand which layers are impactful and how deep they can penetrate into the Arctic Ocean.
4. A simulated satellite measuring sea ice concentration in GCMs. In this era of Arctic sea ice melting, sea ice ponds are more and more present. This presence of water on sea ice is not detected by satellites who would register water instead of ice. A simulated satellite possessing the biases of real satellites would provide more comparable results to observations.
5. Climate simulations evolving through the future forcings instead of time. Several fields such as the sea ice volume behaves in a simpler way when plotted with the extra forcing instead of time. It could save computational time since one simulation through extra forcing forecasts all the future scenarios at once.

## A CCSM4 code verification

The CCSM4 code can be obtained following the instructions on the UCAR web site<sup>6</sup>. For those who could still be interested in the CCSM3, it can be obtained on the Earth System Grid web page: <https://www.earthsystemgrid.org/>. A search for ?CCSM3 code? should quickly bring the user to the download options for the code.

Only the west-east components are explicitly presented. The south-north component is calculated identically but over a different index.

### A.1 Temperature equation

The temperature equation is coded in the subroutine *tracer\_update* called at line 551 of *baroclinic.F90* and defined at line 1600:

```
1680   FT = c0
1691   call hdifft(k, WORKN, TMIX, UMIX, VMIX, this_block)
1694   FT = FT + WORKN
1761   call advt(k,WORKN,WTK,TMIX,TCUR,UCUR,VCUR,this_block)
1763   FT = FT - WORKN ! advt returns WORKN = +L(T)
1788   call vdiff(k, WORKN, TOLD, STF_IN, this_block)
1790   FT = FT + WORKN
1835   call set_pt_interior(k,this_block,WORKN(:,:,1))
1853   call add_kpp_sources(WORKN, k, this_block)
1856   call add_sw_absorb(WORKN, SHF_QSW(:,:,bid), k, this_block)
1859   FT = FT + WORKN
1971   TNEW(:,:,:k,n) = TOLD(:,:,:k,n) + c2dtt(k)*FT(:,:,:n)
```

The six involved subroutines are: (1) *hdifft* for the horizontal diffusion, (2) *advt* for the advection, (3) *vdiff* for the vertical diffusion, (4) *set\_pt\_interior*, *add\_kpp\_sources* and *add\_sw\_absorb*. Each routine computes its heat input in WORKN which is added to FT the temperature flux. We need to follow how WORKN is calculated in each routine. For each instance of WORKN, we want to know if it is output by the CCSM4.

### A.2 Horizontal diffusion

The horizontal diffusion is the first element of the temperature budget being called. The subroutine *hdifft* can be found in *horizontal\_mix.F90* at the line 413. The variable WORKN changes its name to HDTK. There are three diffusion schemes: laplacian (*hmix\_del2*), biharmonic (*hmix\_del4*) and Gent-McWilliams (*hmix\_gm*). The simulation *b40.20th.track1.1deg.012*

<sup>6</sup>[http://www.cesm.ucar.edu/models/ccsm4.0/ccsm\\_doc/x367.html](http://www.cesm.ucar.edu/models/ccsm4.0/ccsm_doc/x367.html), last visited May 9, 2018

used the Gent-McWilliams scheme. The routine computing the Gent-McWilliams mixing, *hdifft\_gm*, is located in the file *hmix\_gm.F90*. The variable HDTK in file *horizontal\_mix.F90* changes its name to GTK in file *hmix\_gm.F90*

### hmix\_gm.F90

```

1162 subroutine hdifft_gm (k, GTK, TMIX, UMIX, VMIX, this_block)
1344 TX(i,j,kk,n,bid) = KMASKE(i,j) &
1445 * (TMIX(i+1,j,kk,n) - TMIX(i,j,kk,n))
1440 TX(i,j,kk+1,n,bid) = KMASKE(i,j) &
1441 * (TMIX(i+1,j,kk+1,n) - TMIX(i,j,kk+1,n))
2023 WORK3(i,j) = KAPPA_ISOP(i, j,ktp,k,bid) &
2024 + HOR_DIFF (i, j,ktp,k,bid) &
2025 + KAPPA_ISOP(i, j,kbt,k,bid) &
2026 + HOR_DIFF (i, j,kbt,k,bid) &
2027 + KAPPA_ISOP(i+1,j,ktp,k,bid) &
2028 + HOR_DIFF (i+1,j,ktp,k,bid) &
2029 + KAPPA_ISOP(i+1,j,kbt,k,bid) &
2030 + HOR_DIFF (i+1,j,kbt,k,bid)
2076 FX(:,:,n) = dz(k) * CX * TX(:,:,k,n,bid) * WORK3
2077 FY(:,:,n) = dz(k) * CY * TY(:,:,k,n,bid) * WORK4
2340 GTK(i,j,n) = ( FX(i,j,n) - FX(i-1,j,n) &
2341 + FY(i,j,n) - FY(i,j-1,n) &
2342 + FZTOP(i,j,n,bid) - fz )*dzc(k)*TAREA_R(i,j,bid)

```

CX is related to the grid. TMIX is the tracer at the mixing time level. KMASKE is the ocean mask for the east side of grid cells. The CCSM grid places the tracers at the centre of the grid, figure 2.8.

To calculate the tracer diffusion, it is required to compute the tracer value at the sides of the cell times the diffusion component. TX and TY are the tracer values at the east side of the cell and at the north side of the cell respectively. WORK3 and WORK4 are the diffusion component on the east side and north side of the cell respectively. FX is the eastward diffusion of heat on the east side of the cell and FY is the northward diffusion of heat on the north side of the cell. Finally, GTK is the divergence of diffusion of a cell.

Once GTK is sent back in *horizontal\_mix.F90* as HDTK, it is integrated vertically and output as variable HDIFT.

### horizontal\_mix.F90

```

333 call define_tavg_field(tavg_HDIFT,'HDIFT',2, &
334 long_name='Vertically Integrated Horz Mix T tendency', &
335 coordinates='TLONG TLAT time', &
336 units='centimeter degC/s', grid_loc='2110')
413 subroutine hdifft(k, HDTK, TMIX, UMIX, VMIX, this_block)

```

```

485 where (k <= KMT(:,:,bid))
486 WORK = dz(k)*HDTK(:,:,1)
491 call accumulate_tavg_field(WORK,tavg_HDIFT,bid,k)

```

KMT gives the index of the deepest grid cell on T grid. The CCSM code defines output field using function *define\_tavg\_field* and then averages and stores date using function *accumulate\_tavg\_field*. Here, the variable tavg\_HDIFT is linked to the output variable HDIFT in line 333. The variable work is averaged as tavg\_HDIFT which will be output as HDIFT, line 491.

The MOAR outputs three extra variables for diffusion: HDIFE\_TEMP, HDIFN\_TEMP, HDIFB\_TEMP. There is nothing about those variables in the code. Based on their definition using the terminal command ncdump, it is reasonable to believe that HDIFE\_TEMP is FX in line 2076 and HDIFN\_TEMP is FY in line 2077. FX and FY units are  $cm^3 \circ C/s$  while HDIFE\_TEMP and HDIFN\_TEMP are  $\circ C/s$ . Therefore we believe, FX and FY have been divided by TAREA and dz to give HDIFE\_TEMP and HDIFN\_TEMP.

We can test our hypothesis by reconstructing HDIFT from the vertically integrated divergence of HDIFE\_TEMP and HDIFN\_TEMP. Following lines 2340 and 2341 in hmix\_gm.F90, the divergence is given by

$$HDIFE\_TEMP_{ij} \cdot TAREA_{ij} - HDIFE\_TEMP_{i-1j} \cdot TAREA_{i-1j} \quad (A.1)$$

$$+ HDIFN\_TEMP_{ij} \cdot TAREA_{ij} - HDIFN\_TEMP_{ij-1} \cdot TAREA_{ij-1}. \quad (A.2)$$

Using the output of the history file b40.20th.track1.1deg.012.pop.h.1998-12.nc, the error between HDIFT and its reconstruction peaks at  $0.03 W/m^2$ , figure A.1. We conclude that HDIFE\_TEMP and HDIFN\_TEMP are the eastward and northward diffusive heat flux respectively.

In conclusion, the vertically integrated divergence of the ocean diffusive heat flux is stored by the CCSM as HDIFT. For the MOAR of the CCSM4, extra variables are output: the eastward diffusive heat flux HDIFE\_TEMP and the northward diffusive heat flux HDIFN\_TEMP.

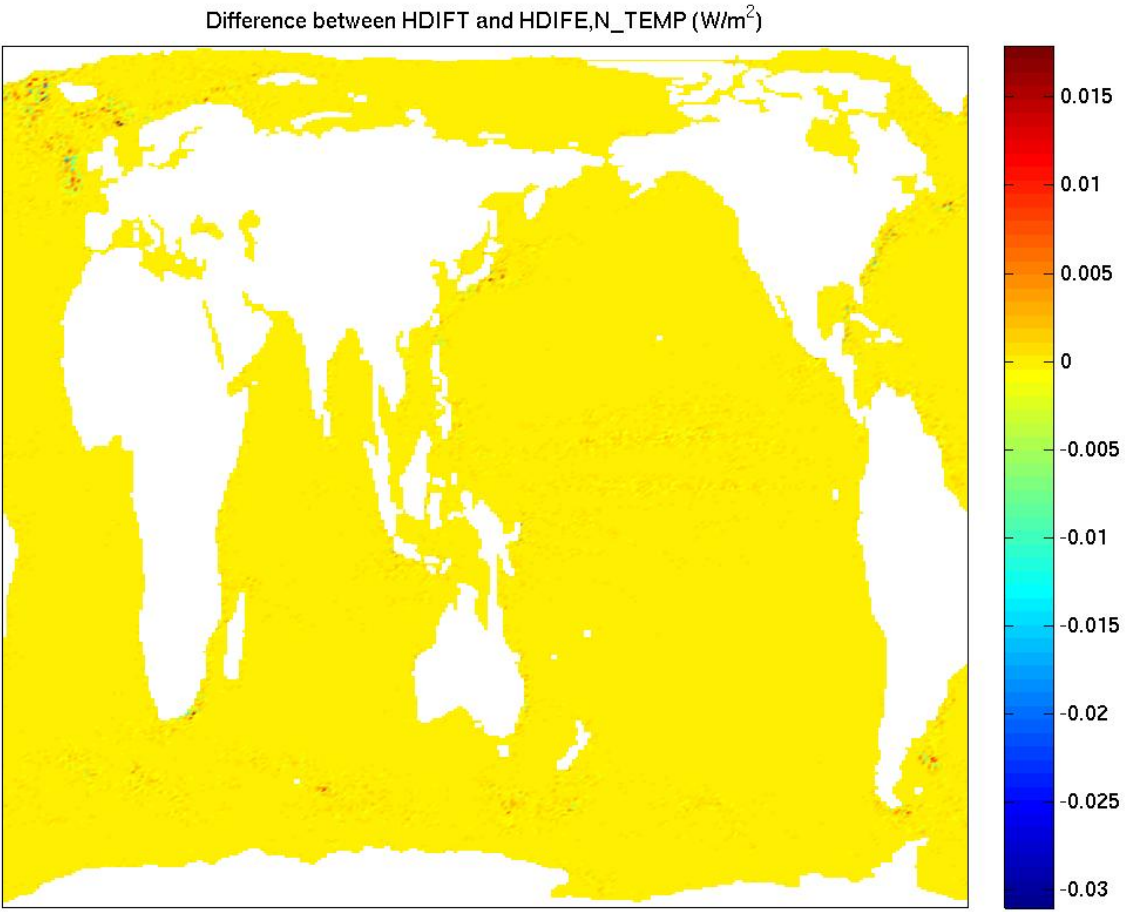


Figure A.1: Difference between HDIFT and its reconstruction from HDIFE\_TEMP and HDIFN\_TEMP in  $W/m^2$ .

### A.3 Advection

The second element of the temperature budget is the heat advection calculated in subroutine *advt* which can be found in the file *advection.F90*. The variable WORKN changes its name to LTK.

#### advection.F90

```

1602    subroutine advt(k,LTK,WTK,TMIX,TRCR,UUU,VVV,this_block)
2513    LTK(i,j,n) = p5*((VTN(i,j)-VTN(i,j-1)+UTE(i,j)-UTE(i-1,j)) &
2514    *TRCR(i,j,k,n) + &
2515    VTN(i,j)*TRCR(i,j+1,k,n) - &
2516    VTN(i,j-1)*TRCR(i,j-1,k,n) + &
2517    UTE(i,j)*TRCR(i+1,j,k,n) - &
2518    UTE(i-1,j)*TRCR(i-1,j,k,n))* &
2519    TAREA_R(i,j,bid)/ &
2548    LTK(:,:,n) = LTK(:,:,n) + dz2r(k)*WTK* &
2549    (TRCR(:,:,k-1,n) + TRCR(:,:,k,n))
2562    LTK(:,:,n) = LTK(:,:,n) - dz2r(k)*WTKB* &
2563    (TRCR(:,:,k,n) + TRCR(:,:,k+1,n))

```

VTN is the northward velocity located on the north side of the cell and UET is the eastward

velocity on the east side of the cell. LTK starts by computing the divergence of horizontal tracer transport. It then adds vertical tracer transport at the top of the cell and then at the bottom of the cell.

The variable LTK is then multiplied by minus the vertical length of the cell, summed vertically and stored as ADVT.

#### advection.F90

```

782 call define_tavg_field(tavg_ADV_TRACER(1),'ADVT',2, &
783 long_name='Vertically-Integrated T Advection Tendency',&
784 units='centimeter degC/s', grid_loc='2110', &
785 coordinates='TLONG TLAT time')
1602 subroutine advt(k,LTK,WTK,TMIX,TRCR,UUU,VVV,this_block)
1922 WORK(i,j) = -dz(k)*LTK(i,j,n)
1926 call accumulate_tavg_field(WORK,tavg_ADV_TRACER(n),bid,k)

```

In the temperature equation, -WORN is added to FT. The stored version of the vertically integrated heat advection already includes the minus sign as of line 1922. Therefore, the temperature budget made from the output of the CCSM will have the form  $\frac{dT}{dt} = ADVT + \dots$  instead of the usual  $\frac{dT}{dt} + ADV = \dots$ .

From the variable list, two other variables are giving advective heat transport: UET and VNT. They are calculated in file advection.F90. The following analysis depicts the investigative work required to understand how is calculated an output variable of the CCSM.

#### advection.F90

```

749 call define_tavg_field(tavg_UE_TRACER(1),'UET',3, &
754 call define_tavg_field(tavg_VN_TRACER(1),'VNT',3, &
1777 FVN = p5*VTN*TAREA_R(:,:,bid)
1778 FUE = p5*UTE*TAREA_R(:,:,bid)
1820 WORK = FUE*( TRCR(:,:,k,n) + &
1821 eoshift(TRCR(:,:,k,n),dim=1,shift=1))
1822 call accumulate_tavg_field(WORK,tavg_UE_TRACER(n),bid,k)
1835 WORK = FVN*( TRCR(:,:,k,n) + &
1836 eoshift(TRCR(:,:,k,n),dim=2,shift=1))
1837 call accumulate_tavg_field(WORK,tavg_VN_TRACER(n),bid,k)
2337 UTE(i,j) = p5*(UUU(i,j,k)*DYU(i,j,bid) + &
2338 UUU(i,j-1,k)*DYU(i,j-1,bid))
2342 VTN(i,j) = p5*(VVV(i,j,k)*DXU(i,j,bid) + &
2343 VVV(i-1,j,k)*DXU(i-1,j,bid))

```

The variable WORK is accumulated as *tavg\_UE\_TRACER*, line 1822, which is output as UET, line 749. WORK is calculated as west-east velocity on the east side of the cell times

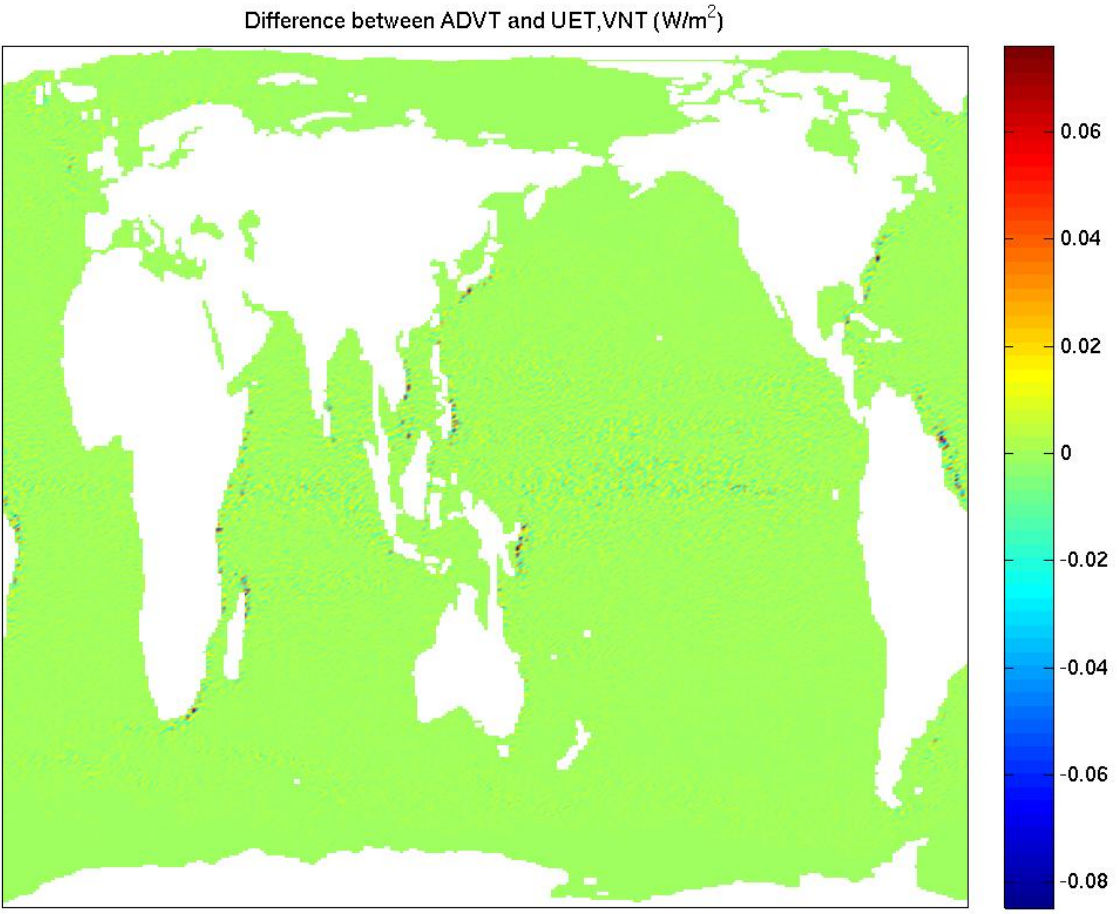


Figure A.2: Difference between ADVT and its reconstruction from UET and VNT in  $W/m^2$ .

the length of the east side divided by the surface area, FUE, multiplied by the tracer on the east side of the cell. It is the advective tracer transport per surface area unit per vertical length unit.

Putting together the pieces of code for ADVT, UET and VNT, it seems UET and VNT are the east and north part of ADVT divided by TAREA. The divergence must be calculated as shown in the diffusion section, equation A.1. The error between ADVT and its reconstruction is extremely high for 34 columns over 122,880 peaking at  $8000 W/m^2$ . Once those 34 points are neglected, the error drops at a maximum of  $0.1 W/m^2$ , figure A.2. We do not fully understand the source of the high error over such a small number of columns. We believe it could come from storing errors from the hardware.

In conclusion, the vertically integrated divergence of heat advection is stored in variable ADVT with an extra minus sign. Variables UET and VNT are the eastward and northward heat advection.

### A.3.1 Vertical diffusion

The third element of the temperature equation is the vertical diffusion. It is calculated in file *vertical\_mix.F90*. The variable WORKN changes its name to VDTK.

vertical\_mix.F90

```

645 subroutine vdifft(k, VDTK, TOLD, STF, this_block)
733 if (k == 1) then
734 VTF(:,:,n,bid) = merge(STF(:,:,n), c0, KMT(:,:,bid) >= 1)
735 endif
765 VTFB = merge(VDC(:,:,kvdc,mt2,bid)* &
766 (TOLD(:,:,k,n) - TOLD(:,:,kp1,n))*dzwr(k) &
767 ,c0, KMT(:,:,bid) > k)
771 VTFB = merge( -bottom_heat_flx, VTFB, &
772 k == KMT(:,:,bid) .and. &
773 zw(k) >= bottom_heat_flx_depth)
777 VDTK(:,:,n) = merge((VTF(:,:,n,bid) - VTFB)*dzc(k), &
778 c0, k <= KMT(:,:,bid))
788 VTF(:,:,n,bid) = VTFB

```

VDTK is calculated as the difference between VTF and VTFB. They are the vertical heat diffusion at the top and the bottom of the cell respectively. The model sets the vertical heat diffusion at the bottom of the ocean at zero. It then calculates the bottom heat diffusion of the next cell by multiplying the diffusivity, VDC, and the temperature at the bottom of the cell. The surface heat diffusion of the lower cell is defined by the bottom heat diffusion of the higher cell. For the first layer, the vertical heat diffusion is defined as STF. It is defined in the file forcing\_coupled.F90

forcing\_coupled.F90

```

715 STF(:,:,1,iblock) = (EVAP_F(:,:,iblock)*latent_heat_vapor &
716 + SENH_F(:,:,iblock) + LWUP_F(:,:,iblock) &
717 + LWDN_F(:,:,iblock) + MELTH_F(:,:,iblock) &
718 -(SNOW_F(:,:,iblock)+IOFF_F(:,:,iblock)) * latent_heat_fusion_mks)* &
719 RCALCT(:,:,iblock)*hflux_factor

```

STF includes several surface fluxes: evaporation, sensible heat, emitted and absorbed long wave, melt, snow and ice runoff. Note that the standard output files describe the latent heat of vapour units as KJ/Kg but it actually has units of J/Kg.

The subroutine collecting the standard output variables, accumulate\_tavg\_field, is not called in subroutine vidfft for the variable VDTK. Hence, the vertical diffusion is not part

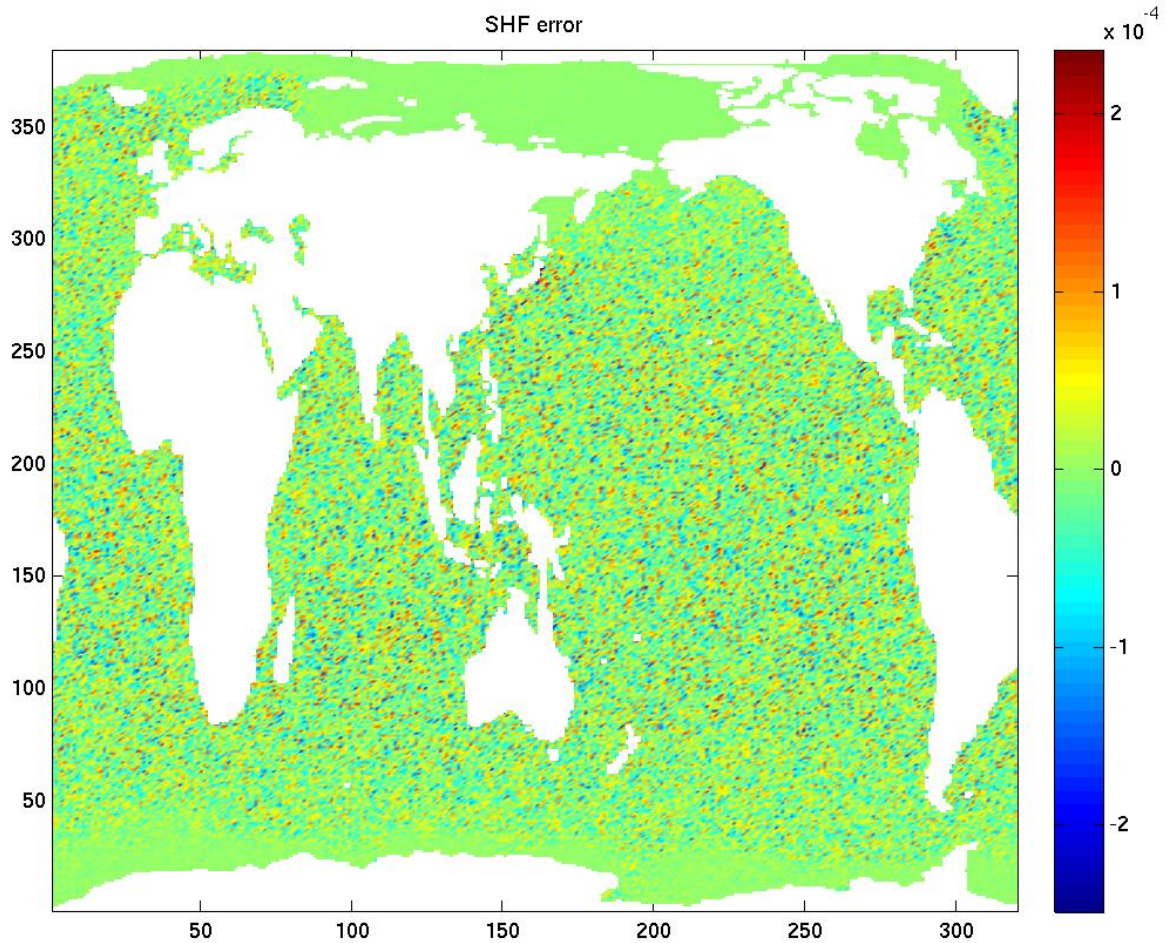


Figure A.3: Code definition of SHF verification with the output variables: SHF, EVAP\_F, SENH\_F, LWUP\_F, LWDN\_F, MELTH\_F, SNOW\_F, IOFF\_F, SHF\_QSW.

of the standard output. When integrated vertically, the diffusion at the top of a cell will be cancelled by the bottom of the following cell (line 788) leaving only the contribution from the bottom and top of the column. The bottom of the column is set at zero (line 778) and the top of the column holds surface fluxes (lines 670, 734-735). The variable STF plus the shortwave radiation absorbed by the ocean is output as variable SHF.

forcing.F90

```

445  WORK = (STF(:,:,1,iblock)+SHF_QSW(:,:,iblock))/ &
446  hflux_factor ! W/m2
451  call accumulate_tavg_field(WORK,tavg_SHF,iblock,1)

```

Every surface fluxes are output separately. When the definition of SHF is compared to the output files, the resulting error is machine accurate, figure A.3.

In conclusion, the vertical diffusion is not output by the CCSM. It is possible to work around it by calculating the vertically integrated budget. The only non-zero terms left after

the integration are: evaporation, sensible heat, emitted and absorbed longwave, melt, snow and ice runoff. They are output separately or as a bundle with the shortwave radiation in variable SHF.

#### A.4 Reset temperature

The fourth element of the temperature budget, set\_pt\_interior, is calculated in file forcing\_pt\_interior.F90. The variable WORN changes its name to PT\_SOURCE.

forcing\_pt\_interior.F90

```

677 subroutine set_pt_interior(k,this_block,PT_SOURCE)
756 DPT_INTERIOR = pt_interior_restore_rtau* &
757 (PT_INTERIOR_DATA(:,:,k,bid,now) - &
758 TRACER(:,:,k,1,curtime,bid))
766 PT_SOURCE = PT_SOURCE + DPT_INTERIOR

```

The constant pt\_interior\_restore\_rtau is defined as  $(24 * 60^2 * 10^{20})^{-1}$ . It is the reciprocal of the restoring timescale. The variable PT\_INTERIOR\_DATA is defined as the limit temperature the model allows. If the computed temperature exceeds the limit, the model restores the temperature at the limit. It is not part of the standard output. Though, the variable QFLUX, which is part of the standard output, seems to hold that role. It is defined in ice.F90.

ice.F90

```

451 POTICE = (TFRZ - TNEW(:,:,k,1))*DZT(:,:,k,bid)
506 QICE(:,:,bid) = QICE(:,:,bid) - POTICE
692 QFLUX(:,:,bid) = QICE(:,:,bid)/tlast_ice/hflux_factor

```

From the code, [Hunke and Lipscomb \(2010\)](#) and [Smith and Gent \(2004b\)](#),

$$QFLUX = \frac{\Theta_f - \Theta}{\Delta t_{ice}} dz \rho_w C_{pw}. \quad (\text{A.3})$$

It restores any temperature below the freezing temperature and transform this energy in frazil ice formation.

In conclusion, the restoring temperature flux is not part of the standard output. We believe the variable QFLUX holds that role but we did not find any direct link with PT\_SOURCE.

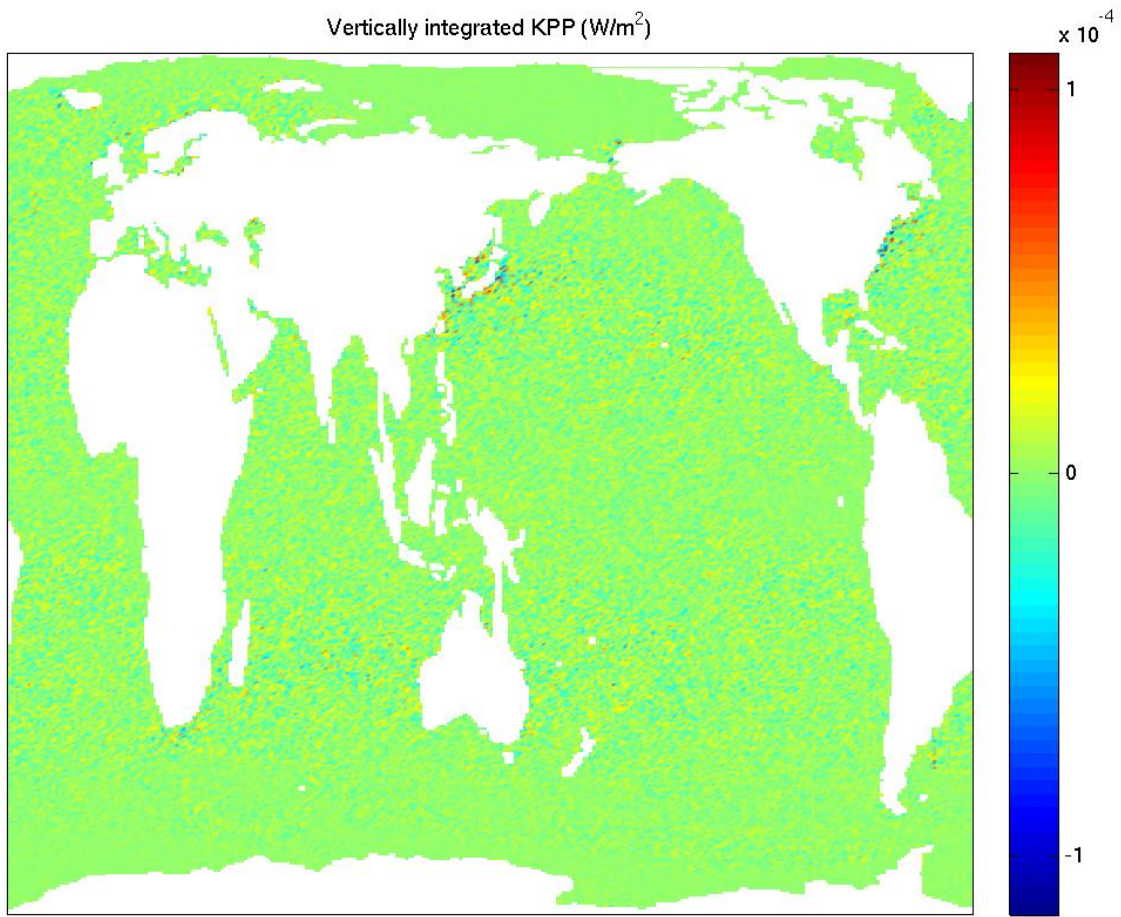


Figure A.4: Yearly vertically integrated KPP mixing term in  $W/m^2$ .

## A.5 KPP

The fifth element of the temperature equation, add\_kpp\_sources, is calculated in vix\_kpp.F90. It is the nonlocal K-profile parameterization for vertical mixing, or KPP, defined in [Large et al. \(1994\)](#). The variable WORKN changes its name to KPP\_SRC.

vmix\_kpp.F90

```

896   KPP_SRC(:, :, k, n, bid) = STF(:, :, n)/DZT(:, :, k, bid) &
897     *( VDC(:, :, k-1, mt2)*GHAT(:, :, k-1) &
898       -VDC(:, :, k, mt2)*GHAT(:, :, k) )

```

VDC is the diffusivity and GHAT is the non-local mixing coefficient. The temperature nonlocal vertical mixing is output as variable KPP\_SRC\_TEMP. Note that KPP\_SRC\_TEMP sums up to zero when integrated vertically, figure [A.4](#).

## A.6 Absorbed short wave

The sixth, and last, element of the temperature budget is add\_sw\_absorb and is calculated in file sw\_absorption.F90. The variable WORKN changes its name to WORK.

sw\_absorption.F90

```
868     WORK = max(SHF_QSW,c0) !*** insure no neg QSW - store in work
```

The variable SHF\_QSW is the short wave absorbed from the ocean. It is given to the ocean component of the CCSM from the coupler that acquired the data from the atmosphere and sea ice components. It is output individually and as a bundle with all the other surface fluxes as SHF. SHF has already been discussed in section [A.3.1](#).

## A.7 Conclusion

Accounting for the six subroutines included in the temperature equation, the required variables for the vertically integrated budget are: HDIFT for the horizontal diffusion, ADVT for the horizontal advection, SHF for the surface forcing included in the vertical diffusion and the short wave absorption, QFLUX for the restoring temperature. The column budget equation becomes:

$$\sum_z \frac{\partial T}{\partial t} = HDIFT + ADVT + SHF + QFLUX. \quad (\text{A.4})$$

## Table of Abbreviations

CCSM	Community Climate System Model
GCM	Global Climate Model
GFDL	Geophysical Fluid Dynamics Laboratory
IMB	Ice-Mass-Balance
NSIDC	National Sea & Ice Data Center
RCP	Representative Concentration Pathway
SHEBA	Surface HEat Budget of the Arctic
SIA	Sea Ice Area
SIE	Sea Ice Extent
SIV	Sea Ice Volume
SRES	Special Report on Emission Scenario
	A1B the reasonable scenario from the SRES
	B1 the optimistic scenario from the SRES
	A2 the pessimistic scenario from the SRES

## References

- Aagaard, K., Coachman, L. K., and Carmack, E. (1981). On the halocline of the arctic ocean. *Deep Sea Research Part A. Oceanographic Research Papers.*
- ACIA (2005). Arctic Climate Impacts Assessment scientific report. *Cambridge University Press.*
- Ahrens, C. D. (2009). Meteorology today an introductin to weather, climate, and the environment 9<sup>th</sup> edition. *Brooks/Cole cengage learning.*
- AMAP (2013). Amap assessment 2013: Arctic ocean acidification. *Arctic Monitoring and Assessment Programme (AMAP).*
- Arfeuille, G., Mysak, L. A., and Tremblay, L.-B. (2000). Simulation of the interannual variability of the wind-driven arctic sea-ice cover during 1958-1998. *Climate Dynamics.*
- Beszczynska-Moller, A., Woodgate, R. A., Lee, C. M., Melling, H., and Karcher, M. (2011). A synthesis of exchanges through the main oceanic gateways to the arctic ocean. *Oceanography.*
- Bonan, G. B., Oleson, K. W., Vertenstein, M., Levis, S., Zeng, X., Dai, Y., Dickinson, R. E., and Yang, Z.-L. (2002). The land surface climatology of the community land model coupled to the ncar community climate model\*. *Journal of Climate.*
- Briegleb, B. P., Bitz, C. M., Hunke, E. C., Lipscomb, W. H., Holland, M. M., Schramm, J. L., and Moritz, R. E. (2004). Scientific description of the sea ice component in the community climate system model, version three. *NCAR Tech. Note.*
- Briegleb, B. P., Danabasoglu, G., and Large, W. G. (2010). An overflow parameterization for the ocean component of the community climate system model. *NCAR technical note.*
- Briegleb, B. P. and Light, B. (2007). A delta-eddington multiple scattering parameterization for solar radiation in the sea ice component of the community climate system model. *NCAR Technical Note.*

- Cavalieri, D. J., Crawford, J. P., Drinkwater, M. R., Eppler, D. T., Farmer, L. D., Jentz, R. R., and Wackerman, C. C. (1991). Aircraft active and passive microwave validation of sea ice concentration from the defense meteorological satellite program special sensor microwave imager. *Journal of Geophysical Research: Oceans*.
- Collins, W. D., Bitz, C. M., Blackmon, M. L., Bonan, G. B., Bretherton, C. S., Carton, J. A., Chang, P., Doney, S. C., Hack, J. J., Henderson, T. B., Kiehl, J. T., and Large, W. G. (2006a). The community climate system model version 3 (ccsm3). *Journal of Climate*.
- Collins, W. D., Rasch, P. J., Boville, B. A., Hack, J. J., Mccaa, J. R., Williamson, D. L., Kiehl, J. T., Briegleb, B., Bitz, C., jiann Lin, S., and Zhang, M. (2006b). The formulation and atmospheric simulation of the community atmosphere model version 3 (cam3). *Journal of Climate*.
- Collins, W. D., Rasch, P. J., Boville, B. A., Hack, J. J., Mccaa, J. R., Williamson, D. L., Kiehl, J. T., Briegleb, B., Bitz, C., jiann Lin, S., Zhang, M., and Dai, Y. (2004). Description of the ncar community atmosphere model (cam3). *Technical Report NCAR*.
- Curry, B., Lee, C. M., and Petrie, B. (2005). Davis strait volume, freshwater and heat fluxes. *Deep Sea Research Part I: Oceanographic Research Papers*.
- Danabasoglu, G., Bates, S., Briegleb, B. P., Jayne, S., Jochum, M., Large, W. G., Peacock, S., and Yeager, S. (2012). The ccsm4 ocean component. *Journal of Climate*.
- Dickinson, R. E., Oleson, K. W., Bonan, G., Hoffman, F., Thornton, P., Vertenstein, M., Yang, Z.-L., and Zeng, X. (2006). The Community Land Model and its climate statistics as a component of the Community Climate System Model. *Journal Of Climate*.
- Dmitrenko, I. A., Kirillov, S. A., Tremblay, L. B., Bauch, D., Holemann, J. A., Krumpen, T., Kassens, H., Wegner, C., Heinemann, G., and Schroder, D. (2010). Impact of the arctic ocean atlantic water layer on siberian shelf hydrography. *Journal of Geophysical Research: Oceans*.
- Dmitrenko, I. A., Polyakov, I. V., Kirillov, S. A., Timokhov, L. A., Frolov, I. E., Sokolov, V. T., Simmons, H. L., Ivanov, V. V., and Walsh, D. (2008). Toward a warmer arctic ocean:

- Spreading of the early 21st century atlantic water warm anomaly along the eurasian basin margins. *Journal of Geophysical Research: Oceans*.
- Feltham, D., Untersteiner, N., Wettlaufer, J., and Worster, M. G. (2006). Sea ice is a mushy layer. *Geophys. Res. Lett.*
- Ferrari, R., McWilliams, J. C., Canuto, V. M., and Dubovikov, M. (2008). Parameterization of eddy fluxes near oceanic boundaries. *Journal of Climate*.
- Ferreira, D. and Marshall, J. (2006). Formulation and implementation of a residual-mean ocean circulation model. *Ocean Modelling*.
- Fetterer, F. K., Knowles, W., Meier, W., Savoie, M., and Windnagel, A. K. (2017). 2017, updated daily. sea ice index, version 3. *NSIDC: National Snow and Ice Data Center*.
- Fissel, D. B., Marko, J. R., and Melling, H. (2004). Upward looking ice profiler sonar instruments for ice thickness and topography measurements. *MTS/IEEE techn-ocean '04*.
- Ford, J. D. (2009). Vulnerability of inuit food systems to food insecurity as a consequence of climate change: a case study from igloolik, nunavut. *Regional Environmental Change*.
- Ford, J. D., Smit, B., and Wandel, J. (2006). Vulnerability to climate change in the arctic: A case study from arctic bay, canada. *Global Environmental Change*.
- Fox-Kemper, B., Danabasoglu, G., Ferrari, R., Griffies, S. M., Hallberg, R. W., Holland, M. M., Maltrud, M. E., Peacock, S., and Samuels, B. L. (2011). Parameterization of mixed layer eddies. iii: Implementation and impact in global ocean climate simulations. *Ocean Modelling*.
- Fox-Kemper, B. and Ferrari, R. (2008). Parameterization of mixed layer eddies. part ii: Prognosis and impact. *Journal of Physical Oceanography*.
- Fox-Kemper, B., Ferrari, R., and Hallberg, R. (2008). Parameterization of mixed layer eddies. part i: Theory and diagnosis. *Journal of Physical Oceanography*.

Gent, P. R., Danabasoglu, G., Donner, L. J., Holland, M. M., Hunke, E. C., Jayne, S. R., Lawrence, D. M., Neale, R. B., Rasch, P. J., Vertenstein, M., Worley, P. H., Yang, Z.-L., and Zhang, M. (2011). The community climate system model version 4. *Journal of Climate*.

Gent, P. R. and Mcwilliams, J. C. (1990). Isopycnal mixing in ocean circulation models. *Journal of Physical Oceanography*.

Golden, K. M., Ackley, S. F., and Lytle, V. I. (1998). The percolation phase transition in sea ice. *Science*.

Gorodetskaya, I. V., Tremblay, L.-B., Liepert, B., Cane, M. A., and Cullather, R. I. (2008). The influence of cloud and surface properties on the arctic ocean shortwave radiation budget in coupled models\*. *Journal of Climate*.

Haas, C., Lobach, J., Hendricks, S., Rabenstein, L., and Pfaffling, A. (2009). Helicopter-borne measurements of sea ice thickness, using a small and lightweight, digital EM system. *Journal Of Applied Geophysics*.

Holland, M. M., Bailey, D. A., Briegleb, B. P., Light, B., and Hunke, E. (2011). Improved sea ice shortwave radiation physics in CCSM4: The impact of melt ponds and aerosols on arctic sea ice\*. *Journal of Climate*.

Holland, M. M. and Bitz, C. M. (2003). Polar amplification of climate change in coupled models. *Climate Dynamics*.

Holland, M. M., Bitz, C. M., and Tremblay, B. (2006a). Future abrupt reductions in the summer Arctic sea ice. *Geophysical Research Letters*.

Holland, M. M., Bitz, C. M., and Tremblay, L.-B. (2006b). Future abrupt reductions in the summer Arctic sea ice. *Geophysical research letters*.

Holland, M. M., Finnis, J., and Serreze, M. C. (2006c). Simulated arctic ocean freshwater budgets in the twentieth and twenty-first centuries. *Journal of Climate*.

Holland, M. M., Serreze, M. C., and Stroeve, J. (2010). The sea ice mass budget of the Arctic and its future change as simulated by coupled climate models. *Climate Dynamics*.

Holliday, N. P., Hughes, S. L., Bacon, S., Beszczynska-Moller, A., Hansen, B., Lavin, A., Loeng, H., Mork, K. A., Osterhus, S., Sherwin, T., and Walczowski, W. (2008). Reversal of the 1960s to 1990s freshening trend in the northeast north atlantic and nordic seas. *Geophysical Research Letters*.

Hunke, E. C. and Dukowicz, J. K. (1997). An elastic-viscous-plastic model for sea ice dynamics. *Journal of Physical Oceanography*.

Hunke, E. C. and Lipscomb, W. H. (2010). Cice: The los alamos sea ice model. documentation and software user's manual. version 4.1. *T-3 Fluid Dynamics Group*.

IPCC (2007). Fourth assessment report of the intergovernmental panel on climate change. *Cambridge University Press*.

IPCC (2013). Fifth assessment report of the intergovernmental panel on climate change. *Cambridge University Press*.

Jahn, A., Sterling, K., Holland, M. M., Kay, J. E., Maslanik, J. A., Bitz, C. M., Bailey, D. A., Stroeve, J., Hunke, E. C., Lipscomb, W. H., and Pollak, D. A. (2012). Late-twentieth-century simulation of arctic sea ice and ocean properties in the CCSM4. *Journal of Climate*.

Jakobsson, M., Mayer, L., Coakley, B., Dowdeswell, J. A., Forbes, S., Fridman, B., Hodnesdal, H., Noormets, R., Pedersen, R., Rebesco, M., Schenke, H. W., Zarayskaya, Y., Accettella, D., Armstrong, A., Anderson, R. M., Bienhoff, P., Camerlenghi, A., Church, I., Edwards, M., Gardner, J. V., Hall, J. K., Hell, B., Hestvik, O., Kristoffersen, Y., Marcussen, C., Mohammad, R., Mosher, D., Nghiem, S. V., Pedrosa, M. T., Travaglini, P. G., and Weatherall, P. (2012). The international bathymetric chart of the arctic ocean (ibcao) version 3.0. *Geophysical Research Letters*.

Jayne, S. R. (2009). The impact of abyssal mixing parameterizations in an ocean general circulation model. *Journal of Physical Oceanography*.

- Johannessen, O., Miles, M., Drange, H., Evensen, G., and Lisoeter, K. (2000). Arctic sea ice reduction - implications for the northern sea route. *Northern Sea Route User Conference*.
- Johannessen, O. M., Shalina, E. V., and Miles, M. W. (1999). Satellite evidence for an Arctic sea ice cover in transformation. *Science*.
- Kalnay, E., Kanamitsu, M., Kistler, R., Collins, W., Deaven, D., Gandin, L., Iredell, M., Saha, S., White, G., Woollen, J., Zhu, Y., Leetmaa, A., Reynolds, R., Chelliah, M., Ebisuzaki, W., Higgins, W., Janowiak, J., Mo, K. C., Ropelewski, C., Wang, J., Jenne, R., and Joseph, D. (1996). The ncep/ncar 40-year reanalysis project. *Bulletin of the American Meteorological Society*.
- Kwok, R., Cunningham, G. F., Wensnahan, M., Rigor, I., Zwally, H. J., and Yi, D. (2008). Thinning and volume loss of the arctic ocean sea ice cover. *Journal of Geophysical Research: Oceans*.
- Laidre, K., Heide-Jorgensen, M., Nyeland, J., Mosbech, A., and Boertmann, D. (2008). Latitudinal gradients in sea ice and primary production determine arctic seabird colony size in greenland. *Proceedings of the Royal Society B: Biological Sciences*.
- Large, W. G., McWilliams, J. C., and Doney, S. C. (1994). Oceanic vertical mixing: A review and a model with a nonlocal boundary layer parameterization. *Reviews of Geophysics*.
- Lawrence, D. M., Oleson, K. W., Flanner, M. G., Thornton, P. E., Swenson, S. C., Lawrence, P. J., Zeng, X. B., Yang, Z. L., Levis, S., Sakaguchi, K., Bonan, G., and Slater, A. G. (2011). Parameterization improvements and functional and structural advances in version 4 of the community land model. *Journal of advances in modeling earth systems*.
- Lawrence, D. M., Slater, A. G., Tomas, R. A., Holland, M. M., and Deser, C. (2008). Accelerated arctic land warming and permafrost degradation during rapid sea ice loss. *Geophysical Research Letters*.
- Laxon, S. W., Giles, K. A., Ridout, A. L., Wingham, D. J., Willatt, R., Cullen, R., Kwok, R., Schweiger, A., Zhang, J., Haas, C., Hendricks, S., Krishfield, R., Kurtz, N., Farrell,

- S., and Davidson, M. (2013). CryoSat-2 estimates of Arctic sea ice thickness and volume. *Geophysical Research Letters*.
- Lehner, F., Raible, C. C., Hofer, D., and Stocker, T. F. (2012). The freshwater balance of polar regions in transient simulations from 1500 to 2100 ad using a comprehensive coupled climate model. *Climate Dynamics*.
- Lindsay, R. and Schweiger, A. (2015). Arctic sea ice thickness loss determined using subsurface, aircraft, and satellite observations. *Cryosphere*.
- Lipscomb, W. H., Hunke, E. C., Maslowski, W., and Jakacki, J. (2007). Ridging, strength, and stability in high-resolution sea ice models. *Journal of Geophysical Research: Oceans*.
- Lique, C., Guthrie, J., Steele, M., and Krishfiled, R. (2013). Diffusive vertical heat flux in the canada basin of the arctic ovean infeered from moored intruments. *Journal of Geophysical research*.
- Markus, T., Cavalieri, D. J., and Comiso, J. (2012). Algorithm theoretical basis document sea ice products. *NASA Goddard Space Flight Center*.
- Maslowski, W., Clement Kinney, J., Higgins, M., and Roberts, A. (2012). The future of arctic sea ice. *Annual Review of Earth and Planetary Sciences*.
- Maslowski, W., Marble, D., Walczowski, W., Schauer, U., Clement, J. L., and Semtner, A. J. (2004). On climatological mass, heat, and salt transports through the Barents Sea and Fram Strait from a pan-Arctic coupled ice-ocean model simulation. *Journal of Geophysical Research - Oceans*.
- Maykut and Perovich (1987). The role of shortwave radiation in the summer decay of a sea ice cover. *Journal of Geophysical Research - Oceans*.
- Maykut, G. and Untersteiner, N. (1971). Some results from a time-dependent thermodynamic model of sea ice. *Geophysical research letters*.
- Maykut, G. A. and McPhee, M. G. (1995). Solar heating of the Arctic mixed layer. *Journal of Geophysical Research*, 1002.

- McLaughlin, F. A., Carmack, E. C., Williams, W. J., Zimmermann, S., Shimada, K., and Itoh, M. (2009). Joint effects of boundary currents and thermohaline intrusions on the warming of atlantic water in the canada basin, 1993?2007. *Journal of Geophysical Research: Oceans*.
- McPhee, M. and Untersteiner, N. (1982). Using sea ice to measure vertical heat-flux in the ocean. *Journal of geophysical research-oceans and atmospheres*.
- McPhee, M. G., Kikuchi, T., Morison, J. H., and Stanton, T. P. (2003). Ocean-to-ice heat flux at the north pole environmental observatory. *Geophysical Research Letters*.
- McPhee, M. G., Kwok, R., Robins, R., and Coon, M. (2005). Upwelling of arctic pycnocline associated with shear motion of sea ice. *Geophys. Res. Lett.*
- Melia, N., Haines, K., and Hawkins, E. (2016). Sea ice decline and 21st century trans-arctic shipping routes. *Geophysical Research Letters*.
- Neale, R., Richter, J., Conley, A., Park, S., Lauritzen, P., Gettelman, A., Williamson, D., Rasch, P., Vavrus, S., Taylor, M., Collins, W. D., Zhang, M., and Lin, S. (2010). Description of the ncar community atmosphere model (cam 4.0). *NCAR Technical Note*.
- Noerdlinger, P. D. and Brower, K. R. (2007). The melting of floating ice raises the ocean level. *Geophysical Journal International*.
- Norris, S., Rosentrater, L., and Eid, P. M. (2002). Polar Bears at Risk a WWF Status Report. *WWF International Arctic Programme*.
- Notz, D. (2005). Thermodynamic and fluid-dynamical processes in sea ice. *Ph.D. thesis, Univ. of Cambridge, Cambridge, U. K.*
- Notz, D. and Grae Worster, M. (2006). A one-dimensional enthalpy model of sea ice. *Annals of Glaciology*.
- Notz, D. and Worster, M. G. (2009). Desalination processes of sea ice revisited. *Journal of Geophysical Research: Oceans*.

NSIDC (2013). All about sea ice. thermodynamics: Albedo.  
<http://nsidc.org/cryosphere/seaice/processes/albedo.html>.

Oleson, K. W., Dai, Y., Bonan, G., Bosilovich, M., Dickinson, R., Dirmeyer, P., Hoffman, F., Houser, P., Levis, S., Niu, G.-Y., Thornton, P., Vertenstein, M., Yang, Z.-L., and Zeng, X. (2004). Technical description of the community land model (clm). *Technical Report NCAR*.

Oleson, K. W., Niu, G. Y., Yang, Z. L., Lawrence, D. M., Thornton, P. E., Lawrence, P. J., Stoeckli, R., Dickinson, R. E., Bonan, G. B., Levis, S., Dai, A., and Qian, T. (2008). Improvements to the Community Land Model and their impact on the hydrological cycle. *Journal Of Geophysical Research-BioGeoSciences*.

Overland, J. E. and Wang, M. (2013). When will the summer Arctic be nearly sea ice free? *Geophysical Research Letters*.

Parkinson, C. L. and Comiso, J. C. (2013). On the 2012 record low arctic sea ice cover: Combined impact of preconditioning and an august storm. *Geophysical Research Letters*.

Perovich, D., Tucker, W., and R., K. (1989). Oceanic heat-flux in the Fram strait measured by a drifting buoy. *Geophysical research letters*.

Perovich, D. K. and Elder, B. (2002). Estimates of ocean heat flux at sheba. *Geophysical Research Letters*.

Petrich, C. and Eicken, H. (2010). Growth, structure and properties of sea ice. *Sea Ice*.

Pfirman, S. and Tremblay, B. (2009). Polar bears' last stand. *New scientist*.

Polyakov, I. V., Beszczynska, A., Carmack, E. C., Dmitrenko, I. A., Fahrbach, E., Frolov, I. E., Gerdes, R., Hansen, E., Holfort, J., Ivanov, V. V., Johnson, M. A., Karcher, M., Kauker, F., Morison, J., Orvik, K. A., Schauer, U., Simmons, H. L., Skagseth, O., Sokolov, V. T., Steele, M., Timokhov, L. A., Walsh, D., and Walsh, J. E. (2005). One more step toward a warmer arctic. *Geophysical Research Letters*.

Pressley, A. (2010). Elementary differential geometry. *Springer-Verlag London*.

- Rainville, L. and Winsor, P. (2008). Mixing across the arctic ocean: Microstructure observations during the beringia 2005 expedition. *Geophysical Research Letters*.
- Rigor, I. G., Wallace, J. M., and Colony, R. L. (2002). Response of sea ice to the arctic oscillation. *Journal of Climate*.
- Rudels, B., Marnela, M., and Eriksson, P. (2008). Constraints on estimating mass, heat and freshwater transports in the Arctic Ocean: An Example. *Arctic?Subarctic Ocean Fluxes*.
- Schaefer, K., Lantuit, H., Romanovsky, V., and Schuur, E. A. G. (2012). *Policy Implications of Warming Permafrost*. United Nations Environment Programme Special Report.
- Schauer, U. and Beszczynska-Moeller, A. (2009). Problems with estimation and interpretation of oceanic heat transport - conceptual remarks for the case of Fram Strait in the Arctic Ocean. *Ocean Science*.
- Schauer, U., Beszczynska-Moller, A., Walczowski, W., Fahrbach, E., Piechura, J., and Hansen, E. (2008). Variation of Measured Heat Flow Through the Fram Strait Between 1997 and 2006. *Arctic?Subarctic Ocean Fluxes*.
- Schweiger, A., Lindsay, R., Zhang, J., Steele, M., Stern, H., and Kwok, R. (2011). Uncertainty in modeled Arctic sea ice volume. *Journal of Geophysical Research - Oceans*.
- Serreze, M. C., Barrett, A. P., Slater, A. G., Steele, M., Zhang, J., and Trenberth, K. E. (2007). The large-scale energy budget of the arctic. *Journal of Geophysical Research: Atmospheres*.
- Serreze, M. C., Barrett, A. P., Slater, A. G., Woodgate, R. A., Aagaard, K., Lammers, R. B., Steele, M., Moritz, R., Meredith, M., and Lee, C. M. (2006). The large-scale freshwater cycle of the arctic. *Journal of Geophysical Research: Oceans*.
- Serreze, M. C., Maslanik, J. A., Scambos, T. A., Fetterer, F., Stroeve, J., Knowles, K., Fowler, C., Drobot, S., Barry, R. G., and Haran, T. M. (2003). A record minimum arctic sea ice extent and area in 2002. *Geophysical Research Letters*.

- Shirtcliffe, T. G. L., Huppert, H. E., and Worster, M. G. (1991). Measurement of the solid fraction in the crystallization of a binary melt. *Journal of Crystal Growth*.
- Shupe, M. D. and Intrieri, J. M. (2004). Cloud radiative forcing of the arctic surface: The influence of cloud properties, surface albedo, and solar zenith angle. *Journal of Climate*.
- Skagseth, A., Furevik, T., Ingvaldsen, R., Loeng, H., Mork, K., Orvik, K., and Ozhigin, V. (2008). Volume and heat transports to the arctic ocean via the norwegian and barents seas. *Arctic-Subarctic Ocean Fluxes*.
- Smedsrud, L., Ingvaldsen, R., Nilsen, J. E., and Skagseth, A. (2010). Heat in the barents sea: Transport, storage, and surface fluxes. *Ocean Science*.
- Smedsrud, L. H., Halvorsen, M. H., Stroeve, J. C., Zhang, R., and Kloster, K. (2017). Fram strait sea ice export variability and september arctic sea ice extent over the last 80 years. *The Cryosphere*.
- Smith, R., Jones, P., Briegleb, B., Bryan, F., Danabasoglu, G., Dennis, J., Dukowicz, J., Eden, C., Fox-Kemper, B., Gent, P., Hecht, M., Jayne, S., Jochum, M., Large, W. G., Lindsay, K., Maltrud, M., Norton, N., Peacock, S., Vertenstein, M., and Yeager, S. (2010). The parallel ocean program (pop) reference manual. *Los Alamos National Laboratory technical note*.
- Smith, R. D. and Gent, P. R. (2004a). Anisotropic gent–mcwilliams parameterization for ocean models. *Journal of Physical Oceanography*.
- Smith, R. D. and Gent, P. R. (2004b). Reference manual for the parallel ocean program (pop) ocean component of the community climate system model (ccsm2.0 and 3.0). *LAUR-02-2484, Los Alamos Natl. Lab., Los Alamos, N. M.*
- Smithson, P., Addison, K., and Atkinson, K. (2002). Fundamentals of the physical environment. *Psychology Press*.
- Steele, M. (1992). Sea ice melting and floe geometry in a simple ice-ocean model. *Journal of Geophysical Research - Oceans*.

- Steele, M. and Boyd, T. (1998). Retreat of the cold halocline layer in the arctic ocean. *Journal of Geophysical Research: Oceans (1978–2012)*.
- Stirling, I. and Derocher, A. E. (2012). Effects of climate warming on polar bears: a review of the evidence. *Global change biology*.
- Stoeckli, R., Lawrence, D. M., Niu, G. Y., Oleson, K. W., Thornton, P. E., Yang, Z. L., Bonan, G. B., Denning, A. S., and Running, S. W. (2008). Use of FLUXNET in the community land model development. *Journal Of Geophysical Research-BioGeoSciences*.
- Stroeve, J., Holland, M. M., Meier, W., Scambos, T., and Serreze, M. (2007). Arctic sea ice decline: Faster than forecast. *Geophysical Research Letters*.
- Stroeve, J., Serreze, M., Drobot, S., Gearheard, S., Holland, M., Maslanik, J., Meier, W., and Scambos, T. (2008). Arctic sea ice extent plummets in 2007. *Eos, Transactions American Geophysical Union*.
- Stroeve, J. C., Kattsov, V., Barrett, A., Serreze, M., Pavlova, T., Holland, M., and Meier, W. N. (2012). Trends in arctic sea ice extent from cmip5, cmip3 and observations. *Geophysical Research Letters*.
- TheCircle (2012). Ice whales - where are they going? *The Circle, WWF magazine*.
- Thorndike, A. S., Rothrock, D. A., Maykut, G. A., and Colony, R. (1975). The thickness distribution of sea ice. *Journal of Geophysical Research*.
- Timmermans, M.-L., Toole, J., Krishfield, R., and Winsor, P. (2008). Ice-tethered profiler observations of the doublediffusive ice-tethered profiler observations of the double-diffusive staircase in the canada basin thermocline. *J. Geophys. Res.*
- Vallis, G. (2006). Atmospheric and oceanic fluid dynamics fundamentals and large-scale circulations. *Cambridge University Press*.
- Vaughan, D. G., Comiso, J., Allison, I., Carrasco, J., Kaser, G., Kwok, R., Holland, D., and al. (2013). Climate change 2013: The physical science basis. contribution of working

group i to the fifth assessment report of the intergovernmental panel on climate change, observations: Cryosphere. *Cambridge University Press*.

Wang, M. and Overland, J. E. (2012). A sea ice free summer Arctic within 30 years: An update from CMIP5 models. *Geophysical research letters*.

Wassmann, P., Duarte, C. M., Agusti, S., and Sejr, M. K. (2011). Footprints of climate change in the arctic marine ecosystem. *Global Change Biology*.

Wijffels, S. E. (2001). Chapter 6.2 ocean transport of fresh water. *Ocean Circulation and Climate*.

Williams, G. P. (1972). Friction term formulation and convective instability in a shallow atmosphere. *Journal of the Atmospheric Sciences*.

Winton, M. (2011). Do climate models underestimate the sensitivity of northern hemisphere sea ice cover? *Journal of Climate*.

Woodgate, R. A., Weingartner, T., and Lindsay, R. (2010). The 2007 bering strait oceanic heat flux and anomalous arctic sea ice retreat. *Geophysical Research Letters*.

Zhang, J. and Rothrock, D. A. (2003). Modeling global sea ice with a thickness and enthalpy distribution model in generalized curvilinear coordinates. *Monthly Weather Review*.

Zwally, . J., Schutz, B., Abdalati, W., Abshire, J., Bentley, C., Brenner, A., Bufton, J., Dezio, J., Hancock, D., Harding, D., Herring, T., Minster, B., Quinn, K., Palm, S., Spinhirne, J., and Thomas, R. (2002). ICESat's laser measurements of polar ice, atmosphere, ocean, and land. *Journal Of Geodynamics*.